Czech Technical University in Prague
Faculty of Mechanical Engineering

Complex Flow Field Structure in A Mid-section of a Last Stage Blade Equipped with a Part Span Connector

Doctoral Thesis

Doctoral study programme: Mechanical engineering
Doctoral field: Fluid Dynamics and Thermodynamics

Supervisor: prof. Ing. Pavel Šafařík, CSc.
Specialist supervisor: doc. Ing. Martin Luxa, Ph.D.
Specialist supervisor: Ing. David Šimurda, Ph.D.

Prague 2023

Ing. Tomáš Radnic

Declaration

I declare that I accomplished my doctoral thesis by myself, and I named all the sources I used in accordance with the guideline about ethical rules during preparation of university final theses. Experimental research described in this thesis was an effort of a team of scientists of Institute of Thermomechanics of the Czech Academy of Sciences, which I was a part of.

In Prague . . . . . Tomas Radnic . . . . . .

Acknowledgment

The author would like to extend most sincere gratitude towards a team of amazing people that he was blessed to work with. It is their patience and willingness to advise and to criticize where necessary which created an environment suitable for immersing oneself into research and personally grow in the meantime.

The author is also aware, that this path has brought many hardships for his family and friends and, that continuous support, both emotional and material, was provided. Not many are lucky enough to have such an excellent loved ones.

There is a hard learned lesson that is worth sharing with any future authors. Experience is something you get after you needed it. Do not despair or delve into feelings of inadequacy.

Title: Complex flow field structure in a mid-section of a last stage blade equipped with a part span connector

Author: Ing. Tomas Radnic

Abstract: This thesis is concerned with the complex problematic of the transonic flow field in the interblade channel with a part span connector called tie-boss. The investigated cascade is comprised of mid-section of a 1220 mm long last stage blade of a large output steam turbine. Two versions of the part span connector were investigated, one with oval cross section and round trailing edge and other with part of the trailing edge being a flat face with sharp edges. Only nominal operating conditions were considered.

The thesis contains results of experimental investigation and numerical simulations. Insight into the flow field phenomena provided by mentioned means is based on detailed theoretical background. The investigation of the flow field was concerned with three main topics, which were vortices, shock waves and flow field parameters. The flow field parameters were evaluated using the method of data reduction and showed the influence of the presence of the tie-boss on loss of kinetic energy and on flow turning. Shock wave configuration was evaluated, and influence of the tie-boss was assessed, namely the deformation of inner branch of the exit shock wave and introduction of new shock waves into the flow field. Vortical structures and their interactions with shock waves were investigated, and their effect on loss of kinetic energy and possibly flow turning discussed.

Influence of the tie-boss geometry on origination of the investigated phenomena was examined and conclusions were drawn regarding future possible optimization of part span connector shape and position. Overall emphasis was placed on the possibility of aerodynamic optimization of device designed to fulfil a critical structural role.

Keywords: Part span connector, transonic flow, shock wave, vortex interaction, CFD, experimental investigation

Název: Transsonické proudové pole na oběžné lopatce posledního stupně parní turbíny s vazební opěrkou

Autor: Ing. Tomáš Radnic

Abstrakt: Ústředním tématem této práce je komplexní vyšetřování proudového pole v lopatkové mříži, která se skládá z profilů středního řezu 1220 mm dlouhé oběžné lopatky posledního stupně parní turbíny velkého výkonu, která je vybavena vazební opěrkou. Při zkoumání byly použity modely dvou typů opěrky, kdy jeden typ byl opatřen zakulacenou odtokovou hranou a část odtokové hrany druhého typu byla tvořena plochým čelem s ostrými hranami. Byl uvažován pouze návrhový režim lopatkové mříže.

Práce obsahuje výsledky experimentálního výzkumu provedeného v aerodynamickém tunelu v laboratořích v Novém Kníně a numerické simulace proudění za pomoci komerčního softwaru. V práci je také uveden teoretický podklad pro vyšetřování jevů proudového pole, zejména pro vznik a chování rázových vln, pro vznik a interakce vírů a pro vyhodnocování integrálních parametrů proudového pole. Integrální parametry proudového pole jsou vyhodnocovány za pomoci metody redukce dat, je vyhodnocena zejména ztráta kinetické energie a výstupní úhel mříže. Dále byl vyhodnocen vliv přítomnosti opěrky na podobu rázových vln v proudovém poli. Bylo zjištěno, že tvar rázových vln je deformován a v proudovém poli vznikly vinou opěrek zcela nové rázové vlny. Dále bylo zjištěno, že jsou v proudovém poli přítomny významné vírové struktury a tyto interagují s úplavy, mezními vrstvami a rázovými vlnami. Dále je diskutován vliv vírů na parametry proudového pole.

Výsledkem práce je vyšetření vlivu geometrie opěrek na proudové pole. Byly představeny možné oblasti optimalizace tvaru opěrek pro snížení jejich vlivu na proudění v mezilopatkovém kanále.

Klíčová slova: vazební opěrka, transsonické proudění, rázová vlna, víry, numerické simulace, experimentální vyšetřování

Table of contents

List of figures

List of tables

1. Foreword

The steam turbine is, and arguably will be, a major contributor to the generation of electric energy. Yesterday's world looked quite bleak for the steam turbine, as the whole world stopped building nuclear or coal power plants in favour of gas turbines and renewable sources of energy. Today's world is different, when the word superpowers learned that short term supplies of crucial fuels can stop or can go through a sharp price increase. As of writing these lines, Japan has pledged to restart its idled nuclear reactors. Despite not building any new nuclear blocks, this brings hope to once again rebuild the reputation of safety and reliability of the nuclear powerplant as carbon neutral power source. Reputation which has been damaged by three major accidents, the latest of which was not caused by mismanagement of the plants but by force of nature.

It is author's firm belief that nuclear powerplant is the only way forward in today's economical, geopolitical and ecological landscape. The energy and heat generation produce about 31% of man-made carbon dioxide emissions [1]. Transportation is attributed for another 15%. While it is true that renewable sources are both cheaper and cleaner than a large nuclear power plant, they lack the stability and as of now volume to support ever greater need for electric energy. The need only grows stronger as in recent years the global warming slowly protrudes into our lives and air conditioning units have become a must have for many southern cities and electric vehicles, which need to be charged often by stations of very high power, steadily increase their market share. Therefore, in author's opinion, building of new nuclear blocks will continue and the steam turbine of large power output will preserve its significance. Building of new steam turbines will continue and the design process of continual improvement will resume.

2. Introduction and state of the art

This thesis is concerned with detailed description of flow field and all associated phenomena present in the interblade channel of a cascade formed with the profiles of the mid-section of the last stage blade of the steam turbine of large power output. This cascade was equipped with the part span connector called tie-boss. Reason for mounting this device on the blade is purely structural. Its aerodynamic influence needs to be described in detail to provide basis for improved design in the future.

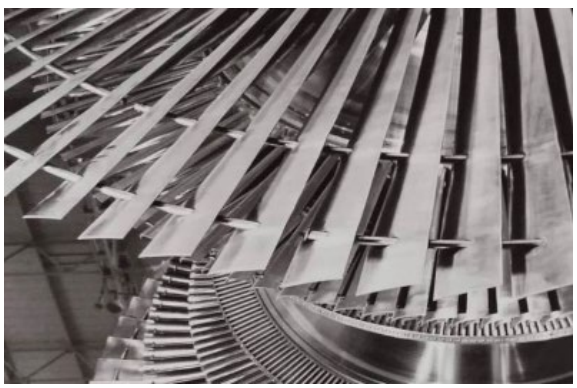

Figure 1 – Blade wheel with stabilization wire.

It is widely understood that natural frequencies do have a profound impact on aeroelastic effects inside the blade wheel. Their presence influences whether there will be aero damping conditions or

flutter conditions [2]. As the race for ever longer last stage blade, and therefore ever larger exit anulus, has led to very long and very thin blades, their natural frequencies shifted to lower numbers. Therefore, blades needed to be stabilized and connectors were designed. In the Figure 1 early design of the connectors is shown. A wire was used as a stabilization device. These were replaced by connector that are mounted on the blades themselves and only come into contact with adjacent blades once the turbine has been started and the non-prismatic blades untwist. The investigated part span connector, called tie-boss, is mounted on a blade equipped with two stabilization devices, see Figure 2.

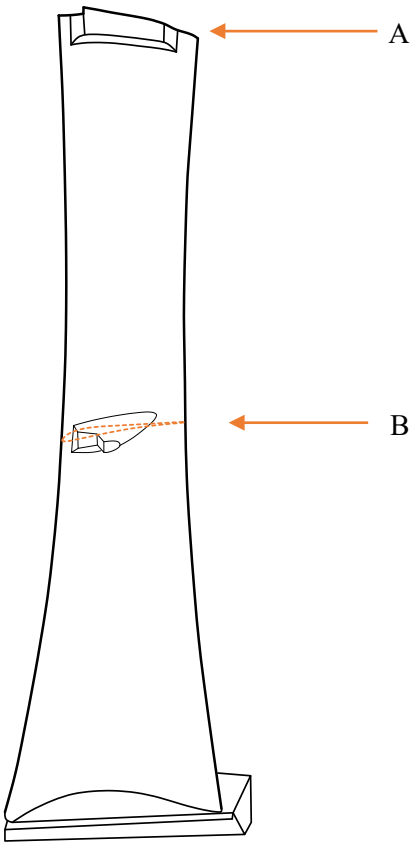

Figure 2 – 1575 mm long rotor blade with integral lock (A) and tie-boss (B) with marked section of the blade used for construction of the cascade.

The stability of the blades has been investigated by the team of Míšek and Kubín, see [3]. The numerical simulation and experimental investigation of the blade wheel with blades interconnected by the tip shrouds and tie-bosses has proved mechanically stable. Natural frequencies were outside the operating range of the 3000-rpm turbine even for over-rotated conditions. However, this particular work was not concerned with assessment of the aerodynamic influence of the part span connector on the interblade flow field. At the same time, authors state that the prolonged last stage blade will lead to improved efficiency of the whole turbine.

Figure 3 – Tie-boss mounted in a blade rotor.

The tie-boss is located in the middle of the blade; hence it is called part span connector by some authors. Tie-boss consists of two opposing metal pieces, see Figure 3. One piece is an integral part of the pressure side of a blade while the other is on suction side of adjacent blade. As mentioned before, the tie-boss abutment surfaces only come into contact after the turbine has been spun up. In stationary state, the turbine blades are able to freely wiggle. Because of the shape of the tie-boss, a formation of strong secondary flows is expected as the shear layers will encounter strong deflecting with the obstructing tie-boss [4].

Aerodynamic investigations of part span connectors (PSC) were carried out by multiple research teams around the globe. Team of Hiteshkumar Mistry [5] did a complete stage computer fluid dynamics (CFD) analysis of very long last stage blade with PSC. The model used by the team is General Electric last stage blade equipped with tip-shroud and part span connector. The working medium was linear gamma approximation model of steam, and the computational domain was of tetrahedral type with surface prismatic layers. The analysis consisted of evaluation of several possible positions of PSC and two models that had the same basic shape, but one had a fillet. Fillet is a rounded transition between the surface of the blade and the body of the PSC. The evaluation showed that the fillet is responsible for large part of the efficiency loss of the PSC and thus its careful design is in order. The evaluation of different PSC positions showed that while PSC itself may even increase the work extracted by the particular part of the blade, the work extraction decreases in adjacent locations. Roughly 30% of blade's span around the PSC is affected by its presence. Additional effect of the presence of the PSC is cross flow from the pressure side of the blade to the suction side of the blade. The cross flow was found to be enabled by the fillet and vortical structures.

This analysis clearly points to the profound effect that vortical structures can have on the flow field and the whole blade efficiency. While scope of this work does not allow for investigation of different PSC placement as well as confirmation that the differently placed connectors would still fulfil their structural role.

Another numerical investigation of PSC was performed by the team of C. Bruggemann [6]. The investigation dealt with numerous variants of a PSC mounted on a linear blade cascade rather than on a full stage. The variants differed in axial position, size, shape, and yaw incidence angle. Working medium for the simulation was air, as ideal gas. The simulations did not include any fillet or mechanical reinforcement for the PSC. Outlet Mach numbers for the simulations were in region of M = 0.57 and M = 0.74. The simulation confirmed that there are major vortical structures causing cross flow between the pressure and suction side of the blade. The study also found that the lower vortical structures were much more massive than the upper one. This research was conducted on fully subsonic blade and the fillet that was not present on investigated blade is crucial for reduction of mechanical stress in the blade. While it gives great insight into the topic, accurate transonic investigation needs to be performed.

Bin Li et al. [7] have led a detailed numerical investigation of last stage blade with PSC. For this investigation, three last stages have been modelled. There were two different variants of PSC, one mounted at 60% of span, another mounted at 63% of span. Mesh modelling has been done by Ansys ICEM and structured mesh has been generated for the whole domain with y^+ in between 30-50. Simulation medium was equilibrium steam model based on IAPWS-IF97. The evaluation revealed that the PSC mounted at 60% of span causes lower losses, but any PSC will affect performance of roughly 40% of span around the PSC. Cross flow has been identified as well as the vortical structures enabling it. Additional losses were assigned to the vortices.

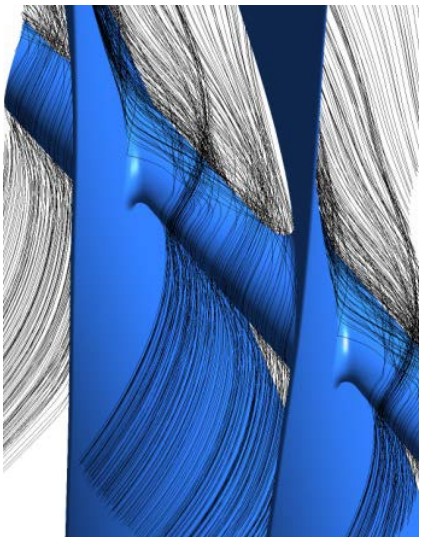

Figure 4 – Cross flow vortex caused by the PSC [7].

Very comprehensive numerical and experimental investigation of PSC was conducted by Häfele et al. [8] and [9]. The research has been done on an industrial steam turbine and has found that the presence of the PSC has effect on all the flow field parameters. Blockage of the flow channel leads to increase of the backpressure of the previous stage, changing performance of the whole machine. The position of part span connectors also played a role. Attention was also paid to shape of the PSC, where circular PSC showed higher losses than elliptical ones, but on the contrary, cylindrical support structures showed lower losses than elliptical ones. It has been also found that the stage efficiency is

reduced significantly as well as changes in the steam wetness. Significant vortical structures and crossflows have also been identified and examined by CFD methods. Authors suggest that additional aerodynamic research might alleviate the effects of the PSC.

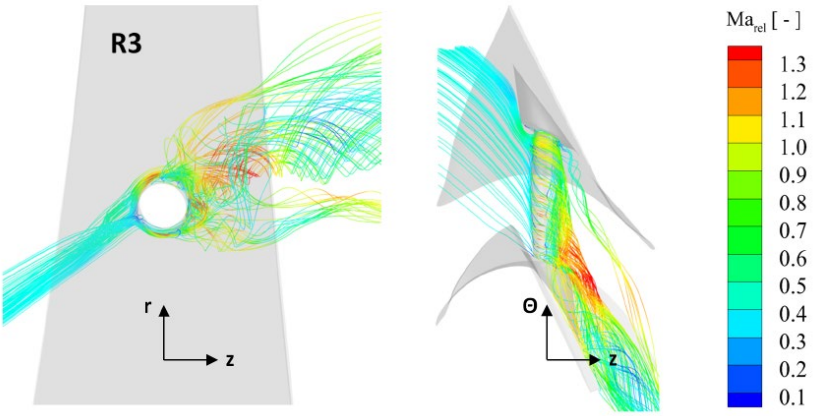

Figure 5 – Identified secondary flows by Häfele et al. [8].

Experimental research by Liu et al. [10] on a scaled model of a turbine, which was aimed at investigating flow though the turbine at off-design conditions, clearly show influence of part span connector on the flow parameters. The presented distributions of exit flow angle and total pressure show clear distortion at approximately 47% of span. Although the connector was not a primary topic of interest for Liu et al., the presented results show that its influence is significant and present in all the investigated flow regimes.

The state of the research published by the authors around the world suggests that the part span connectors induce multiple flow field phenomena and influence overall parameters of the blades. The existing research was focused on part span connectors that had cylindric or oval shape. A detailed study focused on part span connectors with complicated, non-uniform shapes such as tie-boss was not yet presented. The proposed research also heavily focuses on transonic flow, while many of the presented papers are concerned with high subsonic speeds often on different types of blades. The presented research suggests that vortices are important factor in the overall influence of the part span connectors. Therefore, detailed analysis of vorticial structures in transonic blade cascade with PSC ought to be done. Presented research should provide background for the design and development of part span connectors to be placed in last stages of large power output steam turbines.

3. Aims of the work

This thesis is concerned with detailed description and understanding of flow through a blade cascade equipped with part span connectors. Existing research showed that vortical structures are of great importance regarding the flow field phenomena present in the cascade. Great deal of attention is also to be paid to the shock waves in the interblade channel as presence of the connectors is expected to interfere with shock waves greatly. The task ahead can be categorized as follows in order to attain understanding of the flow field.

I. To design and develop techniques that will allow investigation and assessment of complex supersonic three-dimensional flow field containing nonplanar shock waves, vortices, and wakes.

   a. Design of experimental model and assessment of capabilities of experimental setup for the task at hand.

   b. Examination and assessment of phenomena that are expected to be met with the goal of building a set of recognizable patterns in the measured data.

II. Development and validation of numerical simulations able to assess problem with very complicated geometry coupled with complex flow field.

III. Re-examination of the results of experiments to provide more clarity into the flow field phenomena in the context of numerical simulations and newly published research is crucial.

IV. Meticulous examination of the numerical results must be done.

   a. Identification of the flow field phenomena, especially shock waves, vortices and their possible interactions with themselves, wakes and boundary layers should be provided.

   b. Determining the influence of these phenomena on the quality of the flow field and implications on blade cascade performance.

   c. Identification of origins and causes of the various flow field phenomena. Based on this knowledge, a set of recommendations for future investigation and aerodynamic design of the part span connectors should be drawn.

4. Investigated model

4.1. Blade cascade geometry

Due to the properties of the utilized wind tunnel, the investigated model was a linear cascade. The profiles used in the cascade represent section of 1220 mm long last stage rotor blade. This section is located 610 mm above the root of the blade where the tie-boss is located. Profile of the blade is shown in Figure 6.

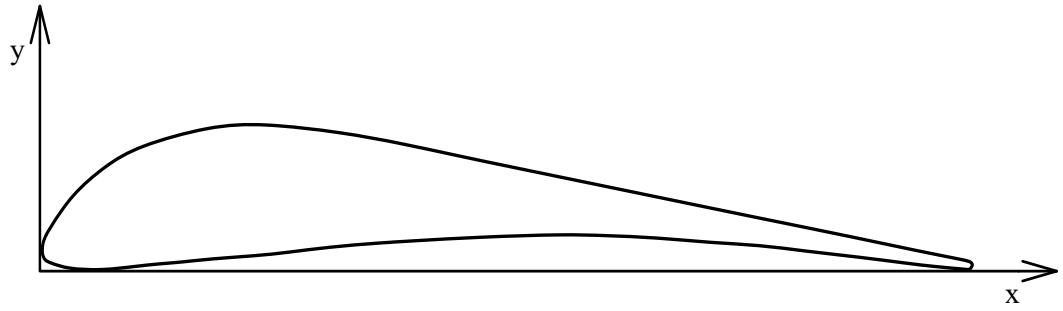

Figure 6 – Section of the 1220 mm long rotor blade located 610 mm above the root section.

The model blade cascade consisted of 8 prismatic blades. Parameters of the cascade are depicted in Figure *7*. Profile chord is c = 80 mm and pitch t = 58.34 mm. Blades were set at stagger angle $\gamma = 55.52°$. The stagger angle is historically defined in the laboratory as angle between the chord line of the profile and normal of the plane of the leading edges (i.e., axis of the machine). Geometry of the blade cascade is very similar to the mid-section cascade which was investigated previously in the laboratory in Nový Knín that was not equipped with the tie-boss [11]. The current blade cascade is slightly more curved, but the maximal deviation of surface curve is below 0.4 mm at the point of maximum profile thickness. The previously investigated cascade was a section of the same blade, but the section was 600 mm above the root of the blade. The nominal inlet angle $\alpha_1 = 30.9°$ and the incidence angle $\iota = 0°$. Then, the expected flow angle $\beta_1 = 30.9°$.

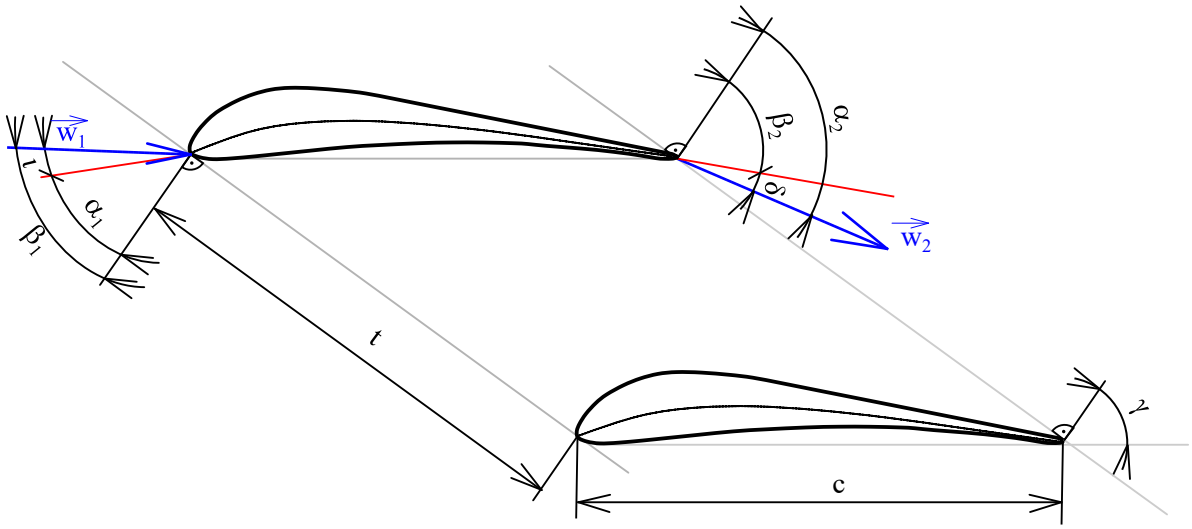

Figure 7 – Description of the geometry of the blade cascade.

4.2. Tie-boss geometry

The tie-boss has, as opposed to stabilizing wire, two parts. One is integral part of the suction side of the blade, while the other is integral part of the pressure side of the adjacent blade. Both parts come into contact as the blade untwists while being loaded, but because of the manufacturing tolerances, there is a notch at the joint.

Two variants of the tie-boss were investigated. Different shapes of the tie-bosses are given by the manufacturer of the blade. The type I tie-boss has an oval cross section along the whole interblade channel, see Figure 8. The notch is placed so that both the parts have similar weight and do not cause any more bending in the blade.

Type II tie-boss has a tailored trailing edge with a cut out. The cut was a measure of weight reduction. However, sharp edges and flat trailing plate were formed. The joint is also shorter as only the cross section (marked A) is significantly smaller than in the case of type I. A scheme with cross section is shown in Figure 9.

Both variants were given trivial designations to simplify the process of identification further in the text. Experimental research on this cascade was party covered by Radnic et al. [R1].

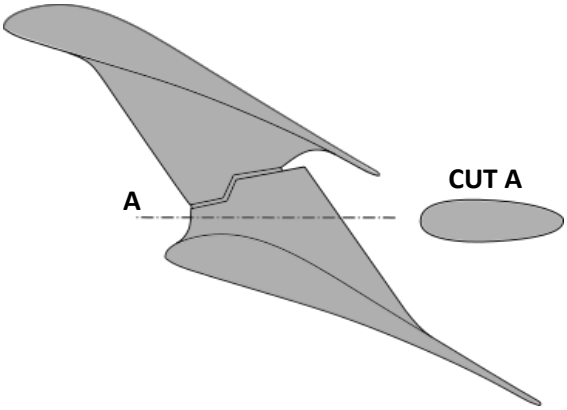

Figure 8 – Tie-boss type I, called oval.

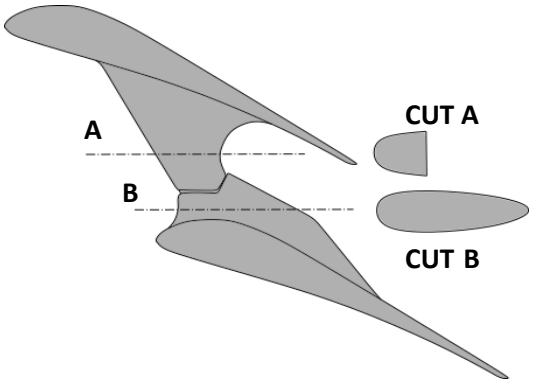

Figure 9 – Tie-boss type II, called tailored.

The design of the tie-boss mounting on the blade was modified to fit modelling of the flow in the wind tunnel. The midplane of the tie-boss body is perpendicular to the plane of the leading edges, while the production tie-boss is slightly rotated to accommodate for the conical flow in a real turbine. The influence of the simplification of the conical flow to cylindrical flow is presumably marginal. The model of tie-boss mounted in the blades 3-6 is shown in Figure 10 and Figure 11.

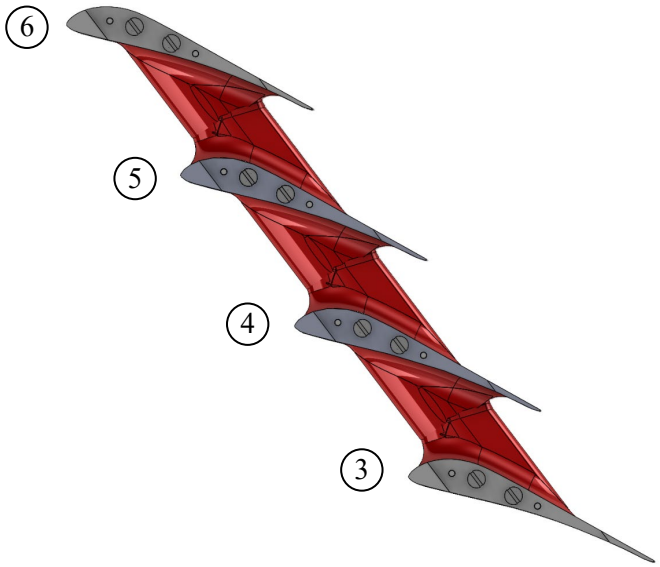

Figure 10 – Type I, oval, tie-boss in the four mid blades of the linear cascade.

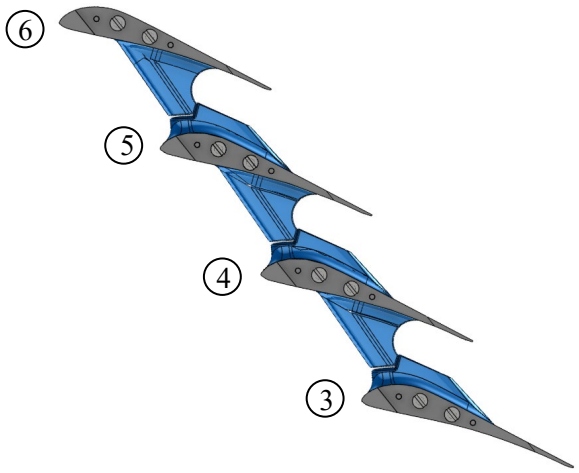

Figure 11 – Type II, tailored, tie-boss in the four mid blades of the linear cascade.

4.3. Scaling of the model

Presence of the tie-boss in the interblade channel limits its flow-through area. There was a relevant concern about a possible shifting of the throat of the cascade due to the obstruction. Shifting of the position of the iso-plane $M = 1$ would mean that the modelled flow would no longer be coherent with real flow in the turbine rotor. Therefore, small enough scaling needed to be chosen. However, preserving flow field parameters is also critical for modelling of the flow. Mach number, as the most important one, would be preserved, but that means, that the Reynolds number, which is dependent on the dimensions of the model, would be not. Ultimately, the chord c = 80 mm was chosen. The chord is shorter than the chord of previously investigated mid-section cascade, which had c = 100 mm [11]. The size itself is a compromise of smallest possible blade, hence lowest probability of chocking while the ability to install static pressure tappings in the blades was maintained. Static pressure tappings requires groves to be milled or in the surface of the blade drilled through its core and in turn weaken the blade. If the chosen scale would be too small, the grooves could not be machined, and measurements would have not been possible at all. The Reynolds number was calculated using equation 4.3.1 [12].

$$\mathrm{Re} = 47130 \cdot \frac{p_{01} M_{2is} c\left[T_0 + 117\left(1 + 0.2M_{2is}^2\right)\right]}{T_0^2\left(1 + 0.2M_{2is}^2\right)^{2.5}} \qquad 4.3.1$$

The Reynolds number was approximately $\mathrm{Re} = 1.2 \cdot 10^6$. Although there is always a compromise in measurements using air as its working medium while modelling steam, which is working medium of the real turbine, the Reynolds number in the measured cascade is in the region of very high, aeromodelling, values. The Reynolds number in the reference mid-section cascade was approximately $\mathrm{Re} = 1.6 \cdot 10^6$, which means that the data can be compared without any significant error. This enabled usage of the formerly measured data as a reference cascade. The scale has been also verified in [R1] by numerical simulations on cascade of infinite width.

4.4. Manufacturing

The tie-boss is manufactured as single 3D printed body. It is mounted through the middle blades of the cascade, which have milled orifices to accommodate it, and mounted on the blades 3 and 6, which had milled groove and holes for fastening. Unlike the research by Mistry et. al. [5], tie-boss without fillet was not considered. The fillet fulfils a structural role, decreasing notch factor and a fillet-less tie-boss could not be incorporated in the real turbine. The fillets were manufactured as standalone parts, mainly because the 3D printing process could not achieve the shape and the mounting orifices in the blades would need to be rather large.

5. Measurement setup

Experimental testing of the cascades was performed in the high-speed wind tunnel of the Aerodynamic laboratory of the Institute of Thermomechanics of the Czech Academy of Sciences in Nový Knín, see [R1]. The layout of the tunnel is in Figure 12.

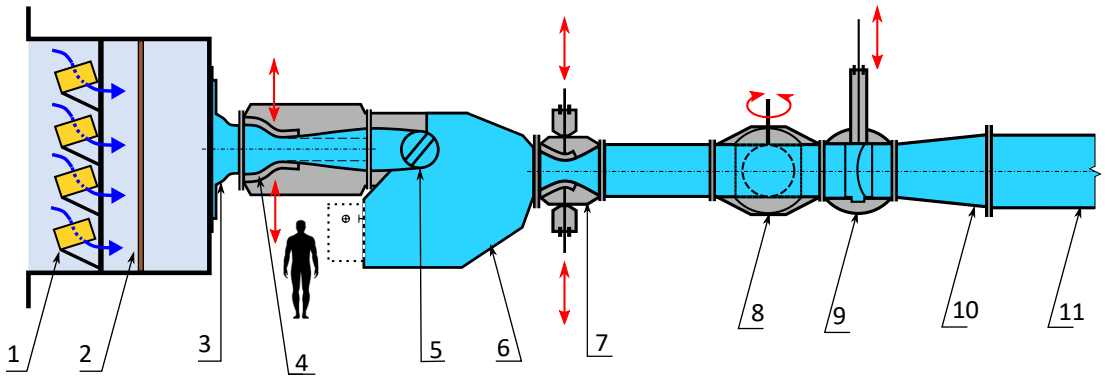

Figure 12 – Layout of the wind tunnel: 1 – silica-gel dryer; 2 – particle filters; 3 – entrance nozzle; 4 – deformable inlet nozzle; 5 – rotatable test section; 6 – settling chamber; 7 – control nozzle; 8 - quick acting valve; 9 – main sluice valve; 10 – diffuser; 11 – vacuum chamber.

The wind tunnel is indraft intermittent type supersonic tunnel with a former gold mine repurposed as the vacuum chamber. The volume of the vacuum chamber is circa 6500 cubic meters, which allows measurement times of dozens of seconds in the test section which is 160 mm wide. The tunnel is powered by three 55 kW vacuum pumps. The inlet flow conditions are set by deformable inlet nozzle and the backpressure is set by the opening of the control nozzle. The settling chamber ensures enough room for the cascade turned flow without causing undesired flow phenomena. The quick acting valve enables limiting of runup and rundown times and limiting the vacuum usage. The turbulence of the inlet flow is below 1.7 % [13].

The inlet flow parameters were measured by a Prandtl probe and static pressure taps on the side walls in front of the cascade. Therefore, the inlet Mach number M_1 was evaluated from the total pressure measured by Prandtl probe located further from the cascade and average static pressure

readings from 5 taps located on the sidewall in front of the cascade. The static pressure readings from tapping placed on the wind tunnel wall are presumed to be corresponding to the static pressure in the free flow based on the Prandtl theorem. The theorem states that the static pressure across the boundary layer remain constant by a dimensional analysis of the boundary layer theory equation. The precise positioning of the tapping is shown in the Figure 13. Static pressure was measured by NetScanner Pressure Systems 9116 multichannel differential pressure sensor with appropriate ranges. The reference barometric pressure p_b was measured by a mercury station barometer. Total temperature T_0 of the inlet flow was measured by a thermistor thermometer. Approximate value of isentropic exit Mach number M_{2is}^{SC} was calculated using total pressure from the Prandtl probe and static pressure measured in the settling chamber. The M_{2is}^{SC} is used for setting the backpressure for attaining the desired flow field parameters that resemble the nominal operational regime of the blade section. The nominal outlet Mach number was M_{2is}^{SC}=1.44 and the incidence angle $\iota = 0°$.

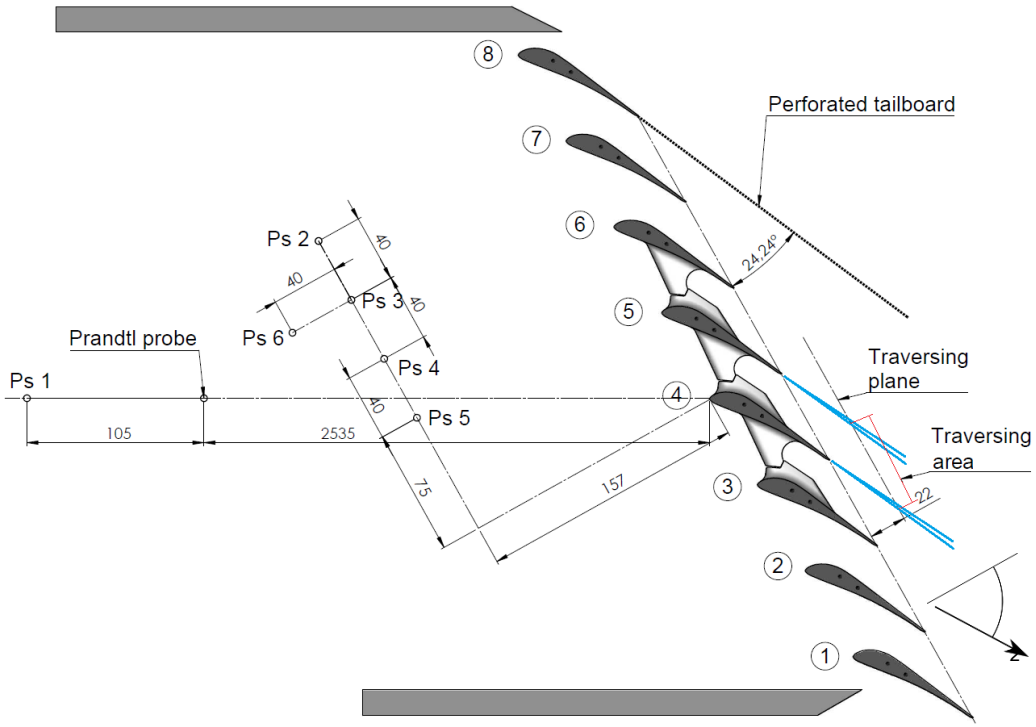

Figure 13 – Scheme of the measurement set-up.

A perforated tailboard was mounted behind the trailing edge of blade No. 8. The tailboard prevents formation of major free stream shear layer behind the topmost blade, which can interact with shock waves and have otherwise negative influence on flow field periodicity, see [14]. Absence of the reflected shock waves improves the periodicity of the flow field as the reflected shock waves do not interact with the shock waves from adjacent blades. The angle of the perforated tailboard was determined by the optical measurements on the reference cascade and was set to $\alpha_{pt} = 24°24'$.

5.1. Pneumatic measurements

Pneumatic measurements on the cascade were conducted by traversing five-hole conical probe trough trajectories on traversing plane at various distances from the side wall of the tunnel. The traversing plane is parallel to the plane of trailing edges of the cascade and offset by 22 millimetres streamwise. The probe was traversed by an inhouse designed device with continuous adjustment of the probe angle by balancing mechanism with a PID controller. The traversing device also enables the probe to be automatically moved in the pitch-wise direction and in span-wise direction and manually moved in the stream-wise direction. The position of the probe is measured by linear resistance sensor TLH300 and TLH225 with indicated precision greater than 0.001 mm. The sensors were recalibrated by a high precision calliper.

The pressures were measured by sensors mounted directly on the device. This design allows for decreased length of the pressure tubing and thus improving the response times. The linear pressure to voltage transducers HUBA Control were used, with indicated precision greater than 0.5% of full scale. The voltage was then measured by National Instruments measuring card and the data acquisition was performed by a LabView code.

During the pneumatic measurements, the probe is traversed trough 25 pitch-wise, one pitch long, trajectories. Image of the trajectories in the traversing plane is shown in section 7.5. Spatial setting of the probe position was done by a precision calliper.

Real values of pressures were calculated from the measured ones using the calibration of the five-hole conical probe. The calibration also includes a correction for a possible shock wave in front of the probe [15]. The pressure transducers were calibrated using the Schildtknecht high precision mercury manometer. The angle of the actively balanced probe was measured by a high precision calibrated resistive sensor GL200 with indicated deviation lower than 0.1°.

5.2. Measurements with five-hole conical probe

For the purposes of evaluation of the of the flow field parameters, a probe capable of measuring total pressure, static pressure and angle of the flow was required. Such a probe must have pressure taps positioned along a surface with variating angle to the flow.

The three-dimensional evaluation of the flow field requires a multidirectional probe. Right circular conical probe was used for the measurements, its apex angle is 60°. The diameter of the probe is 3 mm, and it is equipped with 5 pressure taps, one is at the apex and four are equally spaced on the surface of the cone. The designation of the pressure taps in Figure 14 was chosen with accordance to Bryer and Pankhurst [16].

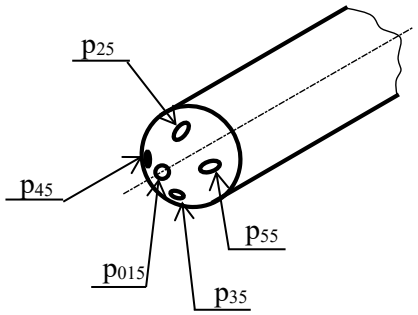

Figure 14 – Five-hole conical probe layout.

Obtaining of the flow filed parameters is much more complicated. The probe was manufactured by Aeroprobe Corporation in the USA and calibrated for transonic and supersonic operations in the laboratory of Institute of Thermomechanics [15]. The aim of the calibration is finding the relation between measured pressures and pitch angle, yaw angle, total pressure, and static pressure of the fluid. The coefficients for calculation of these properties are defined as follows.

$$C_\alpha = \frac{\Delta p_{45-55}}{p_{015} - p_{avg23}} \quad 5.2.1$$

$$C_\beta = \frac{p_{35} - p_{25}}{p_{015} - p_{avg23}} \quad 5.2.2$$

$$C_0 = \frac{p_{015} - p_{01kor}}{p_{015} - p_{avg23}} \quad 5.2.3$$

$$C_s = \frac{p_{01kor} - p_{sI}}{p_{015} - p_{avg23}} \quad 5.2.4$$

he definition of the coefficients differs to the definitions used in [16] because of the way traversing device and pressure transducers are arranged and because the probe was calibrated to work in supersonic conditions. There is no direct reading of p_{45} or p_{55}, there is differential transducer. The pressure p_{01kor} is corrected for the frontal shock wave that will form in higher speeds. The correction was done through coefficient distribution, which was derived from measured p_{015}, and total pressure measured on reference Prandtl probe. The p_{avg23} is the average od the p_{25} and p_{35}. A standalone script for flow field parameters distribution was produced.

5.3. Surface flow visualisation

Visualisation of the surface flow is performed using viscous oil with diluted pigment or kerosene with magnesium powder. The mixtures used in the investigation differ in colour. The white mixture is kerosene and magnesium powder, the orange is the pigment in oil. The mixture is applied to the blade and tie-boss in form of small droplets. Then, when the tunnel is turned on, the aerodynamic forces move the mixture into patterns resembling shear stress in the fluid near the surface of the blade.

6. Expected flow field attributes

The following chapter deals with the flow field phenomena expected to be in the flow field, based on the work by Radnic et al. [R1] and [R2]. The former mentioned clearly showed that there are curved, three-dimensional shock waves in the flow field, while the latter proved that there are massive vorticial structures. Both of the studies lacked the accuracy to capture and explain the phenomena to the fullest.

6.1. Expansion on a turbine stage

For better understanding of used quantities following graph shows a h-s diagram of media expansion on a steam turbine stage with air (ideal gas) as substitute medium. Firstly, the dimensionless velocity M* need to be defined, see 6.1. The difference between the March number and the dimensionless velocity is different norm. While Mach number uses local speed of sound, dimensionless velocity uses critical speed of sound a*.

$$M^* = \frac{w}{a^*}, \tag{6.1}$$

where a* is defined as follows.

$$a^* = \sqrt{\kappa r T^*} \tag{6.2}$$

For the purposes of this thesis, more convenient form of dimensionless velocity expression can be derived, as seen in 6.3 [17].

$$M^* = \sqrt{\frac{\kappa + 1}{\kappa - 1}\left(1 - \frac{T}{T_0}\right)} \tag{6.3}$$

The state of the fluid before the expansion is marked 1, and the fluid expands from pressure p_1 to pressure p_2. The state of fluid after the expansion is marked 2. These pressures are characterized by isobaric curves, which satisfy equation 6.4.

$$h = h_0 e^{\frac{s - s_0}{c_p}} \tag{6.4}$$

This expansion is accompanied by increase of entropy from s_1 to s_2. For determining the efficiency of the expansion, an imaginary state 2′ is created, where the expansion shares same pressure change as the original one, but is reversible, therefore isentropic. The state 2′ has thermodynamic properties marked as isentropic. And while the $p_{2'} = p_{2is} = p_2$, all the other quantities are different. Namely $T_{2is} < T_2$, $M^*_{2is} > M^*_2$.

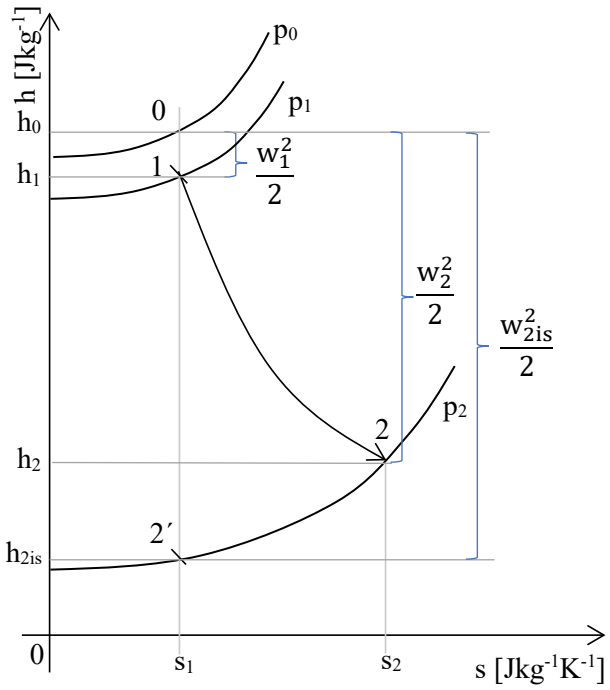

Figure 15 – Graph of expansion in h-s diagram.

Assumption is then made, that isentropic expansion represents ideal flow, the real expansion can be characterised by comparison of states 2 and 2′. The losses in the real expansion can be calculated by kinetic energy loss coefficient ζ, which is defined by equation 6.5.

$$\zeta = 1 - \frac{M^{*2}_2}{M^{*2}_{2is}} \qquad 6.5$$

6.2. Shock wave mechanics

Flow of compressible fluid in the interblade channel which exceeds the speed of sound will induce shock waves to the flow field. Shock wave is a very thin, usually several mean free paths wide, flow discontinuity at which flow parameters change suddenly [18]. There are two main types of shock wave, normal and oblique shock. Main difference between the normal and oblique shock is that normal shock will have subsonic speeds after it occurred, while oblique shock will, most often, have supersonic speed after they occur.

Based on preceding numerical simulation, no normal shock is expected in the flow field. Therefore, focus of upcoming chapter will be in the oblique shock. Oblique shocks form in supersonic flow field when there is a deflection in the flow which turns the flow into itself. Deflection can be caused by changing geometry of the past flown surfaces, or by an interaction with the boundary layer. Basic proposal of oblique shock is that when a distortion is present in the flow, the flow must be parallel to the new direction of the wall, such as in Figure 16 (a).

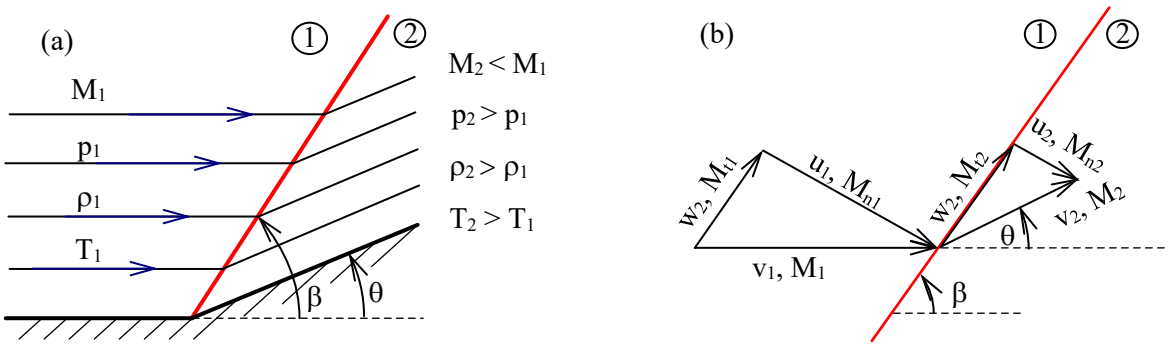

Figure 16 – Oblique shock wave (a), Velocity components of flow on oblique shock wave (b).

As seen in Figure 16 (b) the tangential component velocity is identical for flow upstream and downstream of the shock wave. Then, following equation, called θ – β – M relation [19], can be obtained:

$$\tan\theta = 2\cot\beta\frac{M_1^2\sin^2\beta - 1}{M_1^2(\kappa + \cos 2\beta) + 2}. \qquad 7.1.1$$

This equation states the relation between angle of deflection and upstream Mach number M_1. It also shows that there is maximal deflection angle θ_{max} for specific upstream M_1 above which there is no solution to the equation and no straight oblique shock can exist. In such cases curved shock will occur, which will be detached from the deflective geometry. It is also apparent that for each upstream M_1 and $\theta < \theta_{max}$, there are two solutions for β. The lower solution is called weak and the higher is called strong.

In the internal aerodynamics, there will often be another surface, such as other side of the interblade channel, in the way of propagation on the shock wave. When the shock wave impinges the adjacent surface, another flow turning will be forced. This secondary turning will force a creation of a new shock wave which will be called reflected shock wave.

There is a pending debate whether shock wave and surface interaction can be called reflection. Apparently, the term reflection comes from Ernst Mach. When the first interaction was observed, it strongly resembled the reflection of a light beam from the surface and hence the term shock wave reflection originated. However, from physical point of view the interaction is not a reflection of this kind nor does it respect qualities of light ray reflection like incidence angles. However, from the fluid mechanics point of view it could be argued that the turned fluid flow bounces of the surface which with it interacts and is deflected. The term reflection will be used further in this work because it is well established, but it should be noted that it might not be the correct term for the flow phenomenon.

The reflected shock wave, as shown in Figure 17 (a) will be weaker than the original shock wave, because although the angle of deflection θ stays the same, the M_2 is lower than M_1. Properties of region 3 can be obtained by relation 7.1.1 using conditions of region 2 as upstream conditions. It is also possible, that M_2 would be too low for solution of attached oblique shock. In this case, Mach reflection is formed, see Figure 17 (b). Precise shape of shock waves in this scenario must be determined by utilizing numerical methods. There will also be a slip line in the flow field.

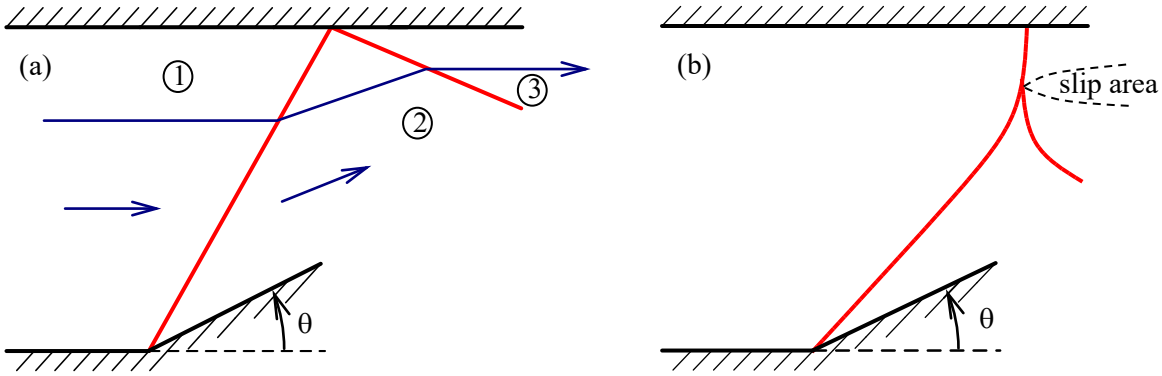

Figure 17 – Diagram of shock regular wave reflection (a) and Mach reflection (b).

In the interblade channel, a situation when two shock waves meet can arise. Such cases are sketched in Figure 18 and Figure 19. In the first case there are two points of deflection, with two different angles of deflection θ_1 and θ_2. From those bases, two shock waves emerge that have different angles of β_1 and β_2 and two zones of different parameters are created, the zones 2 and 3. Yet, after the meeting of the shocks, another flow turning is forced and zone 4 is created. In this process two refracted shock waves emerge. Zone 4 will be separated into two zones, 4 and 4', which will have same direction of flow and pressure, but different other parameters. The separation is called slip line. At slip line, there will be a difference in velocity magnitude and slip will be forced and there will be different entropy.

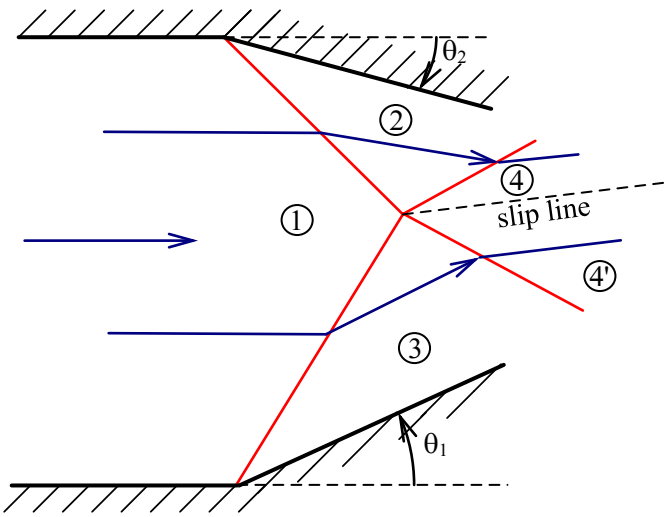

Figure 18 – Interaction of opposite shock waves.

Another type of interaction that can be expected in an interblade channel are two deflections in a configuration where one is downstream of another. Such case is sketched in Figure 19. Here, the flow is deflected by angle θ_1, which leads to creation of shock wave (a). Upstream conditions in zone 1 then change into conditions 2, where $M_1 > M_2 > 1$. Then, another deflection occurs downstream, and shock wave (b) is formed. The deflection angle would be $\theta_2 - \theta_1$ and upstream Mach number is lower than for shock wave (a), hence the shock is weaker in comparison. The shock waves (a) and (b) meet at one point and merge into shock (c). There would be a slip line behind the point of meeting and possibly a reflected shock, because pressure and velocity direction in region 3 and 3' must be identical.

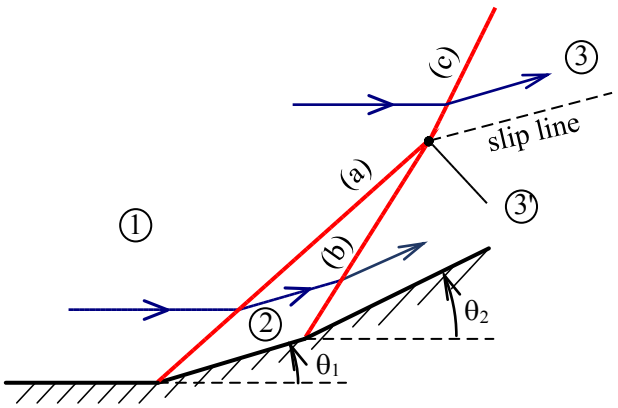

Figure 19 – Interaction of alike oriented shock waves.

In practical supersonic internal flows, a situation can occur where the shock wave will pass through an expansion fan, which is formed by a deflection of flow away from itself. Precise solution of strength and angle of such waves can be obtained numerically or analytically by the method of characteristics, as shown by Safarik in [20]. In such case, the state 2 changes into state 2', where $M_{2'} > M_2 > 1$ because of the expansion. The shape of the shock wave will then deform to accommodate the new conditions.

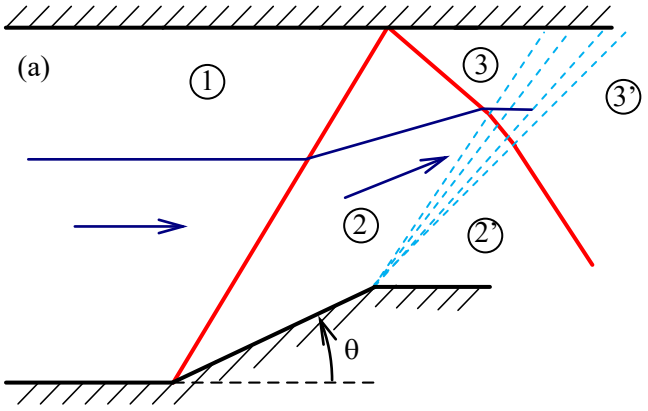

Figure 20 – Interaction of shock wave with expansion fan.

Regarding the topic of shock waves in interblade channel, mechanisms of practical creation are also worth mentioning. Namely exit shock waves, which originate at the trailing edge of the past flown blades. There are two categories of trailing edges, thick and thin, which have different flow conditions, as shown by Luxa [21]. The trailing edge presents a surface that turns away from the flow, as shown in Figure 21. This divergent curvature forces the flow into expansion fan A. Thicker trailing edge will lead to flow separation at points 1 and 2, thus leading to formation of recirculation area called near wake. At the intersection with the near wake, the flow is deflected by angle θ_1. This deflection causes oblique shock wave (a). At the end of the near wake area, there is normalization of flow direction which again bring deflection by angle θ_2. This creates secondary shock wave (b). Those two shock waves interact with one another and merge into a stronger shock wave (c) that is clearly visible on macroscopic level.

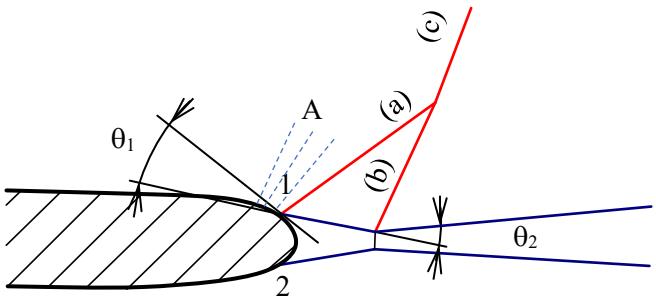

Figure 21 – Shock wave generation at thick trailing edge.

Another possibility of shock wave formation of the trailing edge of the blade is interaction without the near wake area. In the case of thin trailing edge, the near wake area can be very small or not present at all. In this case, there will be only one significant flow deflection θ and θ_1 at each side of the trailing edge. Flow past the trailing edge can be asymmetric, so deflection angles and corresponding shock waves can differ. There will be identical pressures past the exit shock waves, however a slip line can be formed in the wake. It is worth noting that thin leading or trailing edges are impractical for blade profile design.

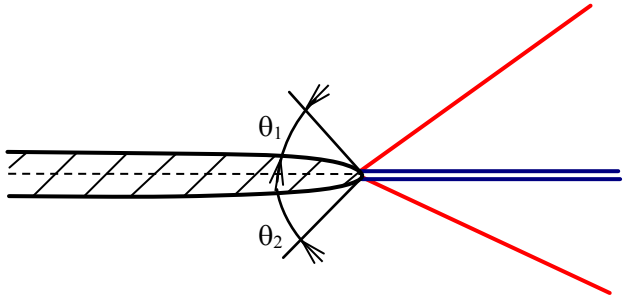

Figure 22 – Shock wave creation at thin trailing edge.

6.3. Vortical mechanics

Next major flow field phenomenon present in the investigated cascade is a vortex. A vortex can be defined as flow which revolves around an axis. In flow of inviscid fluid, vortices can be generally characterized by Helmholtz's theorems.

The first theorem states that the vortex circulation is constant along its filament. The first theorem can be viewed as momentum conservation in the fluid.

$$\Gamma = \text{const} \tag{7.2.1}$$

Second theorem states that fluid circulation remains constant in time. Fluid which had no circulation will remain that way. This also implies that there is no exchange of the fluid between the vortex and outer fluid.

$$\frac{d}{dt}\Gamma = 0 \tag{7.2.2}$$

Third theorem states that vortical filament cannot begin or end in a fluid. It must either be closed loop or lead to a boundary of the fluid.

$$\nabla \cdot (\nabla \times \vec{v}) = 0 \tag{7.2.3}$$

Vortical axis can be straight or curved. The motion of the fluid can be characterized by curl of velocity vector, see 7.2.4, however other metrics will often be utilized.

$$\nabla \times \vec{v} = \hat{i}\left(\frac{\partial v_z}{\partial y} - \frac{\partial v_y}{\partial z}\right) + \hat{j}\left(\frac{\partial v_x}{\partial z} - \frac{\partial v_z}{\partial x}\right) + \hat{k}\left(\frac{\partial v_y}{\partial x} - \frac{\partial v_x}{\partial y}\right) \quad 7.2.4$$

Formation of the complex secondary flow as vortices usually relates to the presence of shear layers in the flow [4] or possibly helical vane, such as in case of [22]. Shear layer presence is, however, directly contradicted by the assumption of Helmholtz's theorems which require inviscid flow. Validity of the theorems for the flow of viscous compressible fluid is expected to be limited. For instance, vortices in viscous flow are known do dissipate in time, even without interaction with any boundary.

According to Bradshaw [4] formation of vortex is usually preceded by distortion of a shear layer present in the flow. There is a debate whether a helical flow caused by swirl vanes would be considered a vortex. Research on shock/vortex interaction by [22] was conducted in a setup with swirl vanes in front of the convergent divergent nozzle. This debate is however purely theoretical in the light of presented work as there are no vanes or other geometry that would cause helical flow. The distortion can be caused by many geometrical features of the flown past object or flow channels.

6.4. Vortex quantification

Qualitative description of vortices is important, but quantitative description is crucial for understanding the influence of vortices on the flow field and for description of interactions of vortices with other flow phenomena. First quantity described is vortex strength or maximal swirl ratio τ. It is the maximal value of tangential speed divided by axial speed in the vortex core, see 7.3.1.

$$\tau = \left(\frac{v_\theta}{v_x}\right)_{max} \quad 7.3.1$$

Problem of the vortex strength as the quantifier is that it is not invariant to chosen plane of examination. If the plane's normal on which the tangential speed was calculated diverted from the vortex axis, the tangential speed would have an axial component, which would make the vortex strength value disproportionately high. Despite its shortcomings, vortex strength can be evaluated in sections further from the geometry on which vortices originate, where flow deflection could be reasonably attributed, and the plane was perpendicular enough to the axis of the vortex. Main reason for utilizing the vortex strength is comparability of obtained data to other authors.

Another possible metric for the vortex is value of velocity curl. Definition term is written in 7.3.2. Right side of the equation is expanded in equation 7.2.4. The $\vec{\omega}$ is called vorticity. Intuitive description of vorticity is twice the angular speed between the flow in the near vicinity of the investigated volume and the investigated volume itself.

$$\vec{\omega} = \nabla \times \vec{v} \quad 7.3.2$$

Vorticity will be equal to zero if the mean angular velocity of surrounding flow is zero. That also means that even if the path lines of the flow are perfectly straight but there is a parallel velocity gradient, such as in a boundary layer, vorticity will be non-zero. Which effectively means that there will always be false positivity of vortex detection. As shown by the research on vortex identification by Jinhee and Hussain [23], the vorticity vector values, which have to be arbitrarily chosen, often do not capture the core of the vortex and rather show wider area around the vortex, or if the value is set so that the vortex core is captured, often secondary rib vortices or weaker cores will be not. It was also found out, that the value of vorticity which captures vortex core well, will also be present in the regions of flow that are not affected by vortices. Those regions are for example boundaries of the wake, the regions of interaction between the shock waves and the regions of interaction of shock waves and the wake. On top of the high vorticity value in the boundary layer, this makes vorticity as criterion for quantification of vortex undesirable.

In the search of better metric, Q criterion was considered. The Q criterion is defined as the second invariant of the velocity gradient tensor. For the intuitive understanding of the criterion, different approach was chosen, see 7.3.3. In the presented term, the S and Ω are the symmetric and antisymmetric part of the velocity gradient tensor respectively.

$$Q = \frac{1}{2}(\|S\|^2 - \|\Omega\|^2) \tag{7.3.3}$$

Q criterion is Galilean invariant, which means that the criterion will stay the same in any chosen evaluation frame even with relative motion between the frames. From the above equation its apparent that Q criterion will be positive when rotational forces will be greater than strain rate or viscous stress.

Another metrics utilized to identify vortex cores is λ_2 criterion. It is the second eigenvalue of $S^2 + \Omega^2$ velocity gradient tensor, see 7.3.4.

$$S^2 + \Omega^2 = -\frac{1}{2}(\lambda_1 + \lambda_2 + \lambda_3) \tag{7.3.4}$$

The λ_2 criterion will show a connected region of Q with two negative eigenvalues, which will indicate existence of local pressure minimum induced by the vortical motion of the fluid. Because Q is symmetric, it will only have real eigenvalues, thus if λ_2 is negative, λ_3 is also sure to be negative. Very comprehensive evaluation of the quality of λ_2 criterion is presented by Jeong and Hussein [23]. The evaluation shows that λ_2 will capture the shape of the vortex core in variety of flows where other criteria may fail. Although λ_2 is based on Q and the detected vortex cores will be similar, it was found that results of λ_2 will resemble reality more closely.

6.5. Vortex – shock interactions

In the transonic flow field with geometry which will induce vortices, a vortex is sure to encounter a shock wave. One of the known phenomena associated with passage of a vortex trough a shock wave is called vortex breakdown. It can be characterized by formation of an enlarged subsonic turbulent conical area and by forming a blunt nosed conical shock upstream to the undisturbed part of the passed shock wave. The broken-down core of a vortex will act as disturbance in the flow. Research presented by Kalkhoran and Smart [24] shows that there is a relation between the τ and freestream Mach number that indicates possible vortex breakdown.

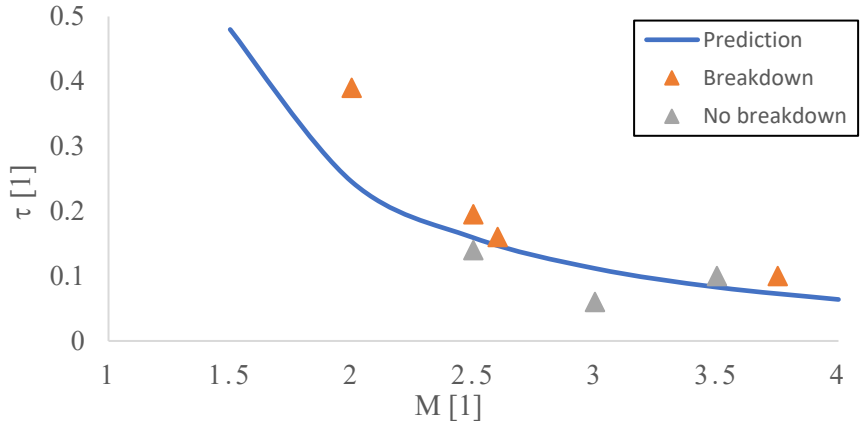

Figure 23 – Relation between the τ and vortex breakdown occurrence [24].

This relation shows that vortices are more likely to break down with higher upstream Mach number. Occurrence of a vortex breakdown in the interblade channel would have wide implications regarding losses of kinetic energy. For the investigated cases, the vortices with the risk of breakdown would have to have τ in the region 0.4.

6.6. Method of data reduction

The traversing device was used to measure flow field parameters in the traversing plane, see Figure 13. The probe was traversed along pitch-wise trajectories that were unevenly distributed in the span-wise direction. Reason for the uneven distribution is reduction of the probe passes in the regions of smaller spanwise changes of the flow and presumably unaffected by the presence of the tie-boss in the cascade.

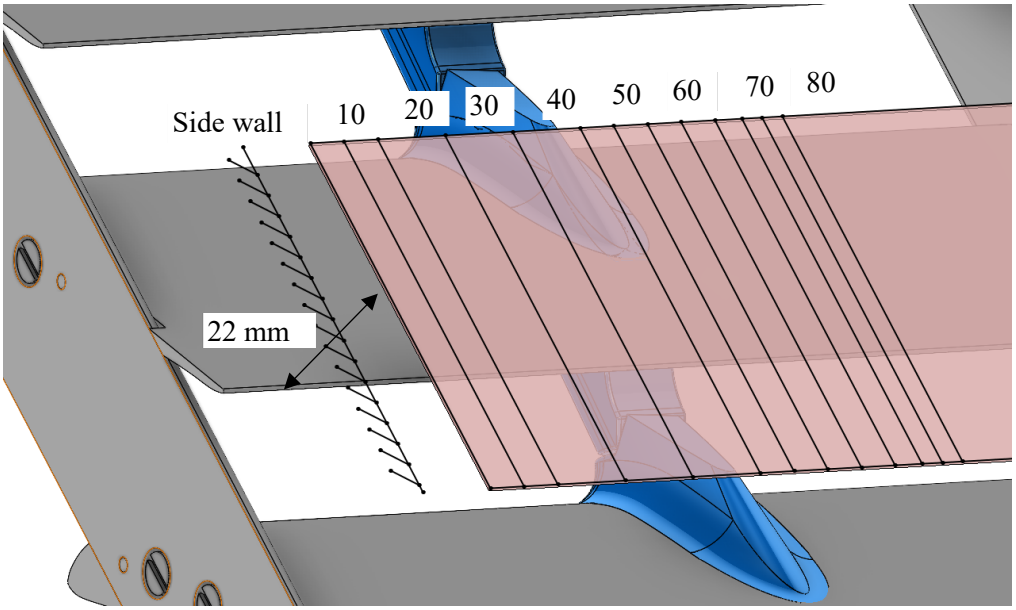

Figure 24 – Schematic of the distribution of half of the traversing trajectories with selected distances from the sidewalls of the test section. The pink plane is visualization of the traversing plane parallel to the plane of trailing edges. Lines on the traversing plane mark the passes of the probe.

In the Figure 24 there is one half of the centrally symmetrical traversing trajectories distribution. The traversing device allows measurement as close as 10 mm from the sidewall of the test section. In order to obtain a pressure distribution in the traversing plane, the coverage of the trajectories had to be dense enough to provide relevant data, however, distance between trajectories further away from the sidewalls or the tie-boss was increased to optimize run time of the wind tunnel.

The pneumatic measurements result in gathering exceptional amount of local data. For evaluation purposes, however, parameters representative of the whole cascade or certain cut along the blade height are needed. Therefore, the method of data reduction has been used. It allows obtaining of integral parameters of the flow field based on strict balance of the mass, energy and momentum fluxes in the flow.

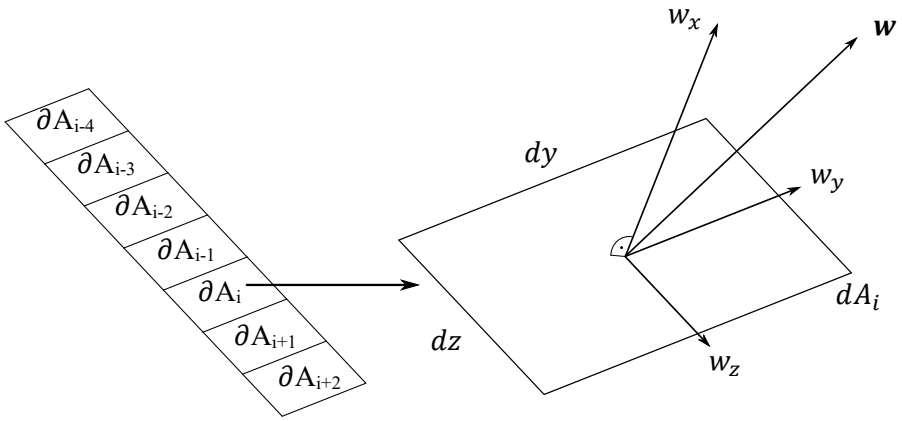

Figure 25 – Scheme of data reduction algorithm.

The method of data reduction, although same in principle, has two variants. The first one, simpler, is used to evaluate parameters of the numerical experiments. The second one is listed in Appendix 1. The simplicity of the method is given mainly by availability of the density ρ at any given point. Therefore, the mean value equations can be written as follows.

Mass flux mean value equation:

$$I_m = \frac{1}{A}\iint_A \left[\rho_{yz}(w_x)_{yz}\right]dy\,dz \qquad 7.5.1$$

Momentum flux mean value equation in the direction x:

$$I_X = \frac{1}{A}\iint_A \left[\rho_{yz}(w_x)_{yz}{}^2 + p_{yz}\right]dy\,dz \qquad 7.5.2$$

Momentum flux mean value equation in the direction y:

$$I_Y = \frac{1}{A}\iint_A \left[\rho_{yz}(w_x)_{yz}(w_y)_{yz}\right]dy\,dz \qquad 7.5.3$$

Momentum flux mean value equation in the direction z:

$$I_Z = \frac{1}{A}\iint_A \left[\rho_{yz}(w_x)_{yz}(w_z)_{yz}\right]dy\,dz \qquad 7.5.4$$

The integrals I_M, I_X, I_Y, I_z can be obtained directly from the data extracted from the CFD. The balance equations containing the reduced parameters can then be written as follows:

$$\rho w_x = I_m, \tag{7.5.5}$$

$$\rho w_x^2 + p = I_X, \tag{7.5.6}$$

$$\rho w_x w_y = I_Y, \tag{7.5.7}$$

$$\rho w_x w_z = I_Z, \tag{7.5.8}$$

where the velocity components w_x, w_y, w_z represent the reference value of velocity component for the investigated area. These equations have been complemented by the energy equation and by the state equation.

$$w_x^2 + w_y^2 + w_z^2 = 2c_p(T_0 - T) \tag{7.5.9}$$

$$p = \rho r T \tag{7.5.10}$$

Solution to this system of equations provides the desired reduced parameters of the flow. Solution of the system was obtained by substituting velocity components:

$$w_x = \frac{I_M}{\rho}, \tag{7.5.11}$$

$$w_y = \frac{I_Y}{\rho w_x} = \frac{I_Y}{I_M}, \tag{7.5.12}$$

$$w_z = \frac{I_Z}{\rho w_x} = \frac{I_Z}{I_M}, \tag{7.5.13}$$

$$T = \frac{p}{r\rho}. \tag{7.5.14}$$

Thus, the final substitution into the equation 7.5.9.

$$\frac{I_M^2}{\rho^2} + \frac{I_Y^2}{I_M^2} + \frac{I_Z^2}{I_M^2} = 2c_p\left(T_0 - \frac{p}{\rho r}\right) \tag{7.5.15}$$

Then a substitution was chosen:

$$K = I_X - p = \frac{I_M^2}{\rho}. \tag{7.5.16}$$

So, the equation 7.5.15 can be written as follows.

$$\frac{K^2}{I_M^2} + \frac{I_Y^2}{I_M^2} + \frac{I_Z^2}{I_M^2} = 2c_p\left[T_0 - \frac{(I_X - K)K}{I_M^2 r}\right] \tag{7.5.17}$$

The equation 7.5.17 can be multiplied by $r^2 I_M^2$ and divided by $2c_p$, obtaining the following:

$$K^2\left(1 - \frac{r}{2c_p}\right) - KI_X - \frac{r}{2c_p}\left(I_Y^2 + I_Z^2\right) + rT_0 I_M^2 = 0\,. \tag{7.5.18}$$

The equation 7.5.18 can be solved using discriminant.

$$K_{1,2} = \frac{I_X \pm \sqrt{D}}{2\left(1 - \frac{r}{2c_p}\right)}, \tag{7.5.19}$$

where D in the equation 7.5.19 can be stated as follows:

$$D = I_X^2 - 4r\left(1 - \frac{r}{2c_p}\right)\left(T_0 I_M^2 - \frac{I_Y^2 + I_Z^2}{2c_p}\right). \tag{7.5.20}$$

Using the parameter K, the integral parameters of the flow field can be obtained using following equations, see Table 1. There is a duality of solution to the problem. The correct solution was decided by inspection of static pressure, where one of the solutions would lead to subsonic results while the flow is known to be supersonic. Amecke and Safarik [25] provide in depth analysis of the duality of the solution.

Table 1 – Integral parameters equations.

$p_{1,2} = I_X - K_{1,2}$	$w_{x_{1,2}} = \frac{I_M}{\rho_{1,2}}$	$w_{1,2} = \sqrt{2c_p(T_0 - T_{1,2})}$
$\rho_{1,2} = \frac{I_M}{K_{1,2}}$	$w_{y_{1,2}} = \frac{I_Y}{I_M}$	$p_{0_{1,2}} = p_{1,2}\left[1 + \frac{\kappa - 1}{2} M_{1,2}^2\right]^{\frac{\kappa}{\kappa-1}}$
$T_{1,2} = \frac{p_{1,2}}{r \cdot \rho_{1,2}}$	$w_{z_{1,2}} = \frac{I_Z}{I_M}$	$M_{is_{1,2}} = \sqrt{\frac{2}{\kappa - 1}\left[\left(\frac{p_{1,2}}{p_0}\right)^{\frac{1-\kappa}{\kappa}} - 1\right]}$
$T_{is_{1,2}} = T_0\left(\frac{p_{1,2}}{p_0}\right)^{\frac{\kappa-1}{\kappa}}$	$\zeta_{1,2} = 1 - \frac{T_0 - T_{1,2}}{T_0 - T_{is_{1,2}}}$	$\Delta s_{1,2} = r \ln \frac{p_0}{p_{0_{1,2}}}$

Using the equations from Table 1, the integral parameters can be obtained. The calculation itself is based on Matlab code that extracts the integrands and calculates values of the desired quantities. The evaluation is carried out, similarly as the evaluation of measured data, by pitch-wise sections of the (virtual) traversing plane. For each column of computational mesh cells there will be value of chosen parameter. This allows obtaining of spanwise distribution of any listed quantity or derived quantity.

Data reduction has been performed in the pitch-wise direction and reduced quantities were evaluated giving span-wise distributions of these quantities. It is also worth mentioning, that presented implementation of data reduction method requires velocity vector components, pressure and density as inputs. Measurements with five-hole probe do provide total pressure, static pressure and pitch and yaw angles. Therefore, a different implementation of the method needed to be used. Description and derivation of these equations are in the Appendix 1.

6.7. Data reduction uncertainty

The method of data reduction in itself is mathematically exact. However, inputs into the method are burdened by uncertainty. Correct question to be asked is what exact influence the input uncertainties have on the reduced flow field parameters obtained by the method.

Multiple approaches to this problem are possible. It is possible to solve the differential equations that lead to exact output uncertainty by input uncertainties. This approach was implemented in [26].

Another approach is direct data variation. This approach requires creation of testing data sets in which there will be different quantities variated to the maximal extent of the measurement devices and output quantities will be monitored. Upside of this approach is its simplicity as well as immunity to mathematical error, as opposed to the exact method mentioned above, which by definition has to have multitude of differential terms. Downside of this approach is the necessity for multiple variated data sets, as it is impossible to determine which quantities will have positive or negative impact on the output values.

For this purpose, a homogenous data field has been created. The field contains 25 entries that correspond to a rectangular 5-to-5-point grid. The parameters have been chosen so that the kinetic energy loss coefficient was equal to $\zeta = 0.04447$. Then, 5000 repetitions of the data reduction were performed, where the physical quantities inputs were varied by random number from -1 % to 1 % of total value of the quantity for each step. The coordinates of individual data point were not varied. Results of the variation are shown in Table 2.

Table 2 – Results of variation of input quantities.

Investigated row	1	2	3	4	5
Mean ζ value	0.04428	0.04456	0.04443	0.04457	0.04470
Standard deviation of ζ	0.0043585	0.0043265	0.00448548	0.00453901	0.00444834

The data shows that maximal deviation of mean output values was lower than 0.7% of overall ζ value. Although the standard deviation is disconcerting, regarding the fact that it reached almost 10%. Higher overall standard deviation is a non-issue for the presented case because the input data are taken from numerically accurate CFD data. Search for maximal possible data deviation, where all the inputs were lowered by 1%, showed that maximal deviation of dimensionless velocity M* in this case was over 7% which would lead to deviation of ζ over 50%. In experimental case, however, the issue would not be so pressing, because calculation of velocities and density is performed from measured pressures, therefore limiting the amount of possibly uncertain values. Regardless, in the experimental measurements, different approach was chosen, as seen in [26].

7. Experimental results

7.1. Reference case

The goal of the conducted research was to assess the influence of the tie-boss on the flow field in the blade cascade. It must be mentioned that the experimental research preceded the numerical research. Therefore, it had not been designed to specifically find the complex flow field phenomena later shown by the numerical simulation. As a comparison a reference cascade without the tie-boss was investigated first. The cascade had identical profile dimensions but was not equipped with the tie-boss. This research was published by Radnic et al. [R1], albeit with slightly different conclusions because of the more limited knowledge of the topic at the time.

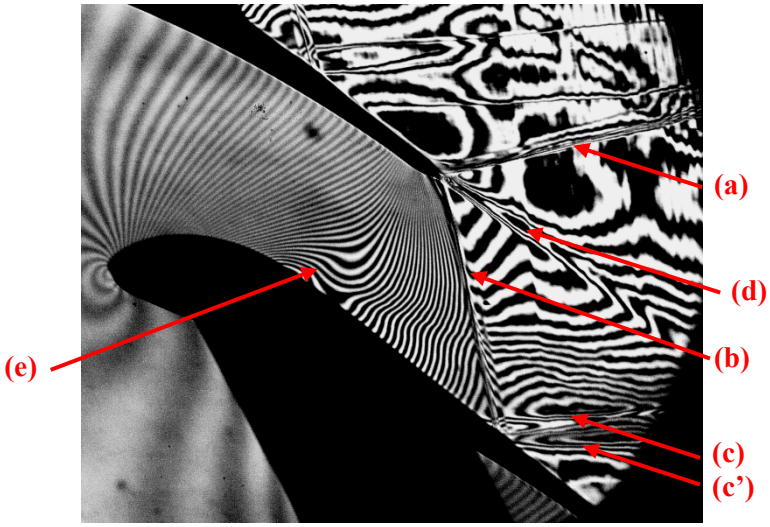

Figure 26 – Interferogram showing 2D flow field in the blade cascade without tie-boss in nominal regime.

These optical measurements were taken from [27] because the profile blade is identical, albeit with different chord, to the investigated blade.

Figure 26 shows that the flow in the interblade channel is transonic with subsonic inlet and supersonic outlet. There are two branches of the exit shock wave, called outer (a) and inner (b). The inner branch is directed into the interblade channel and interacts with suction side of the adjacent blade while the outer branch is directed outwards. Beginning of both branches of the exit shock wave at the trailing edge of the upper blade has characteristic shape similar to letter λ which corresponds to the mechanism of shock wave generation on thick trailing edge. The inner branch of the exit shock wave then impinges on the suction side of adjacent blade where the adverse pressure gradient induced to the flow by

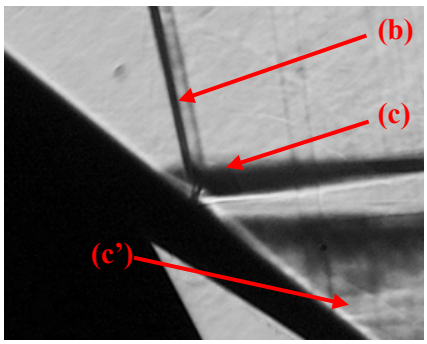

Figure 27 – Schlieren photography of shock wave boundary interaction.

compression on the shock wave causes local separation bubble in the boundary layer. The interaction of the shock wave bares some quantities of interaction with laminar boundary layer, see Figure 27. The reflected shock (c) originates in front of the impingements and there is secondary shock wave (c') downstream of the interaction. The secondary shock is, however, weaker than expected for fully laminar interaction. Wake of the blade (d) is also perfectly visible. Because of the change of the curvature of the blade on the suction side, the transonic recompression (e) can be observed.

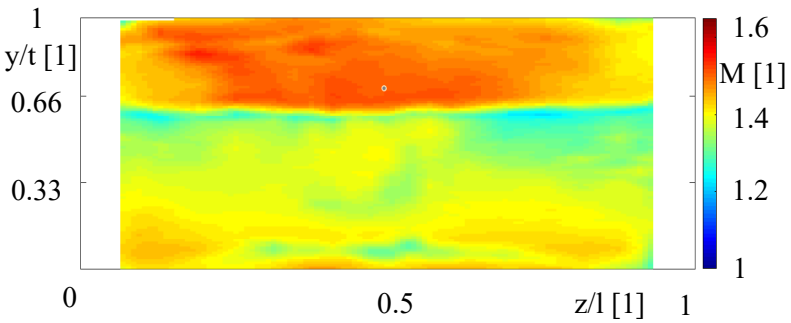

Figure 28 – Distribution of Mach number in the traversing plane.

In Figure 28 there is the distribution of Mach number in the traversing plane and in Figure 29 there is the distribution of kinetic energy loss coefficient. There is a clear trace of outer branch of the exit shock wave, which separates area of high Mach number upstream and lower downstream of it. There is also a slight drop in the Mach number in the wake of the blade, which is in the bottom part of the distribution. The wake is visible much more clearly in the distribution of ζ. There is very clear area of higher loss in the wake which corresponds to the slight drop in Mach number. There is also a trace of the outer branch of exit shock wave, which is much weaker. The trace itself is probably an artefact created when the probe passed through the wave.

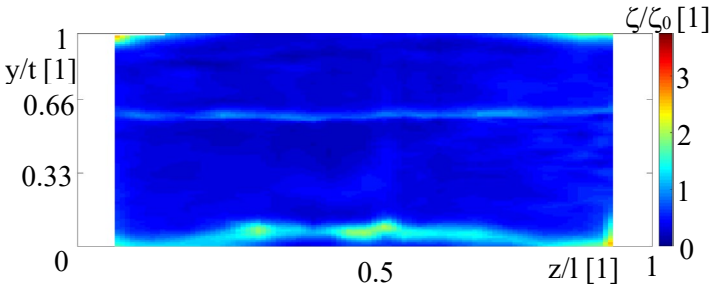

Figure 29 – Distribution of ζ/ζ_0 in the traversing plane.

7.2. Influence of tie-boss on aerodynamic characteristics of blade cascade

Figure 30 and Figure 31 show the same distribution as Figure 28, only this time, there is a tie-boss mounted in the cascade. There are significant flow phenomena traces that are atributed to the tie-boss. In both tie-boss

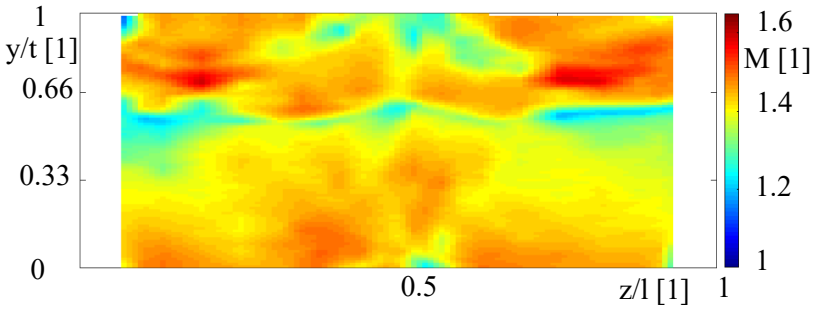

Figure 30 – Distribution of Mach number in the traversing plane of the oval tie-boss.

cases the trace of the outer branch of the exit shock wave is deformed, albeit it is much more deformed in the case of the oval tie-boss in Figure 31.

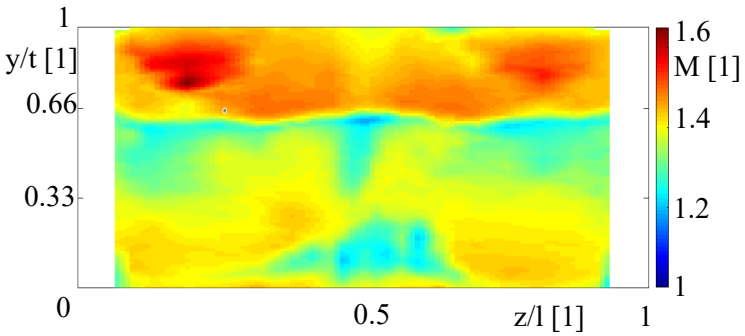

Figure 31 – Distribution of Mach number in the traversing plane of the tailored tie-boss.

Moreover, in case of the oval tie-boss it is apparent that the wake of the blade has partially shifted periodically upwards. This would suggest higher flow turning. In the case of tailored tie-boss, the wake is much larger, thus implying higher losses.

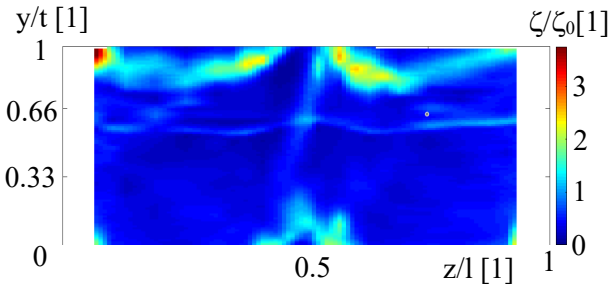

Figure 32 – Distribution of ζ/ζ_0 in the interblade channel with oval tie-boss.

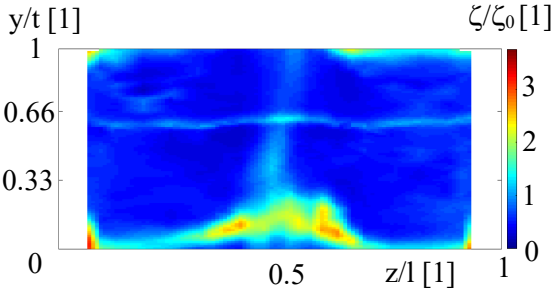

Figure 33 – Distribution of ζ/ζ_0 in the interblade channel with tailored tie-boss.

Distribution of kinetic energy loss coefficient paints similar picture. In Figure 32 and Figure 33 there are distributions of relative loss coefficient. As in the reference case without any tie-boss mounted, the trace of the outer branch of exit shock wave is much smaller than the trace of wake. The areas of significant loss of kinetic energy are concetrated in the wake of the blade near the tie-boss, and wake of the tie-boss itself is clearly visible. The wake of tailored tie-boss seems to have caused higer losses and also the area of high loss in the wake is wider and more pronaunced.

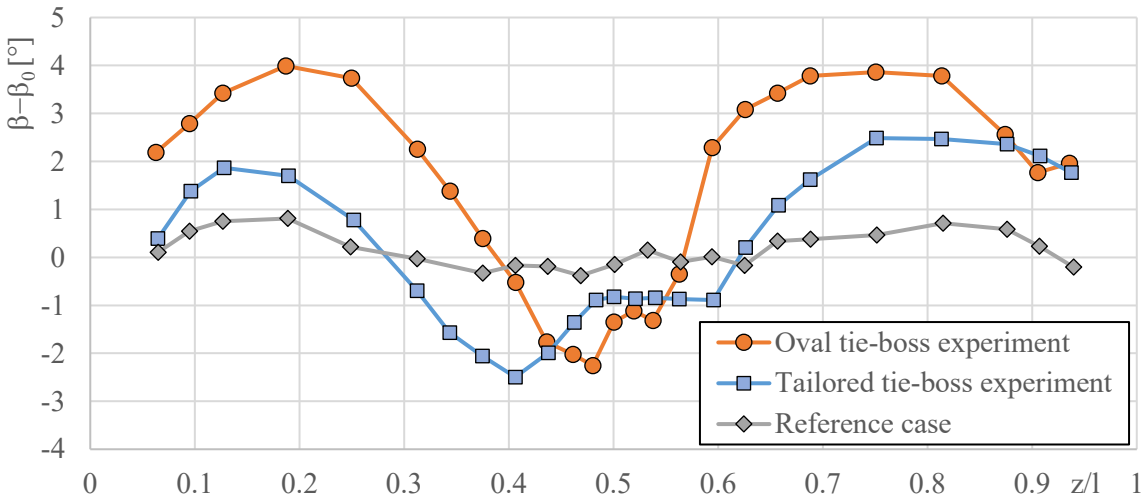

Figure 34 – Distribution of relative exit flow angle $\beta-\beta_0$.

The effects seen in the planar distributions of flow field parameters can be exactly evaluated using span-wise distribution of reduced parameters. The relative exit flow angle of the cascade is shown in Figure 34. The decrease in β in the area right behind the tie-boss is present in both variants of the tie-boss. Peak of the decrease, approx. -2.4° compared to the nominal exit flow angle is present in the tailored tie-boss interblade channel and it is located just outside the wake of the tie-boss. This eccentricity suggest that a vortex might be responsible. It must be remembered that the physical models used for testing lack the notch in the leading edge and side of the tie-boss. This means that the vortex configuration might be different to the simulated case. However, major geometric features, like the tailored trailing edge were modelled and thus, any vortex originating there is expected to develop. The freestream area of this channel is, however, quite close to the reference case. In the case of the oval tie-boss, the turning of the flow is more confined to the area of the wake but the freestream flow turning is quite high, in some places as much as 4° higher than the reference case. The effect of tie-boss is quite dramatic in this regard.

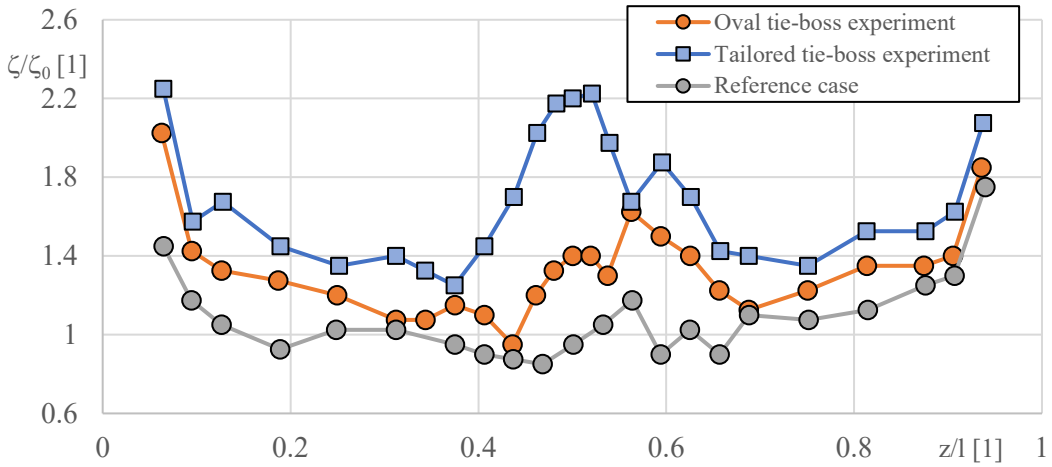

Figure 35 – Distribution of relative kinetic energy loss coefficient.

As shown in the planar distributions, tie-boss also has a profound effect on the loss of kinetic energy. The distribution of reduced relative loss coefficient is shown in Figure 34. The severity of influence on the flow field is reversed. While the oval tie-boss had stronger effect on flow turning, the tailored tie-boss shows much higher losses in wider area. Loss of kinetic energy is spatially more limited in the case of oval tie-boss, although peak of the loss occurs outside the wake of the tie-boss itself. Losses in the interblade channel with tailored tie-boss are much higher and the peak is very wide. Unsurprisingly, massive flow separation at the trailing edge and also near the root of the tie-boss leads to loss of kinetic energy locally more than twice as strong as in the reference case. Reduction of the loss of kinetic energy and negative flow turning is a logical path towards minimizing the adverse effects of tie-boss presence in the interblade channel. However precise understanding of the origin of the changes is required to do so.

7.3. Results of surface flow visualizations

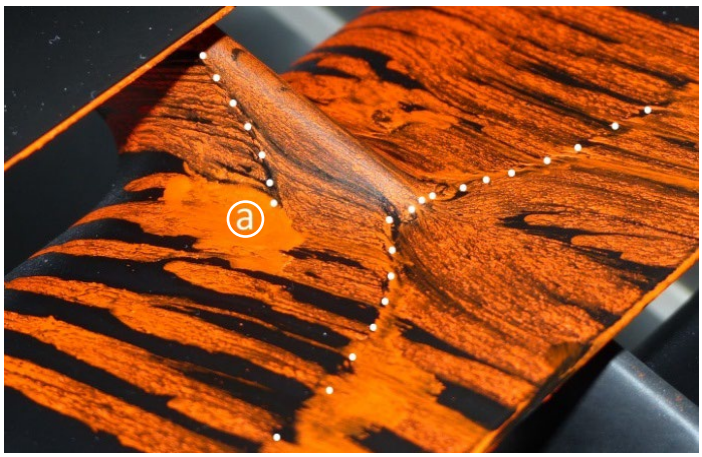

Figure 36 – Surface flow visualisation on the suction side of the blade in oval tie-boss interblade channel.

Figure 37 – Surface flow visualisation on pressure side of the oval tie-boss interblade channel.

Surface flow visualisation of interblade channel with oval tie-boss is shown in Figure 36 and Figure 37. In the first mentioned image, there is a distinct trace of what appears to be the impingement curve of the inner branch of exit shock wave of the adjacent blade. This trace is curved, supposedly as the result of lower Mach number upstream the shock wave in the wake of the tie-boss, leading to lower angle of the shock in the cascade plane. Also, the shock trace is very close to the base of the tie-boss itself, which induces flow turning to the flow which in turn forces creation of a shock wave in the flow. This would mean, however, that the shock would be connected to the exit blade shock by pure coincidence, which is highly improbable, because this behaviour is seen in both types of the tie-boss. There is also trace of what appears to be a vortex filament contact with the surface ending in a separation bubble a. Examination of the video shows that a similar separation bubble forms on the other side of the tie-boss too and that its size is much smaller during the measurement, but the mixture cumulates in this point after the tunnel is shut off. This means that while the separation looks massive, in reality it was rather small. It is clear that under normal circumstances there would be a critical part of the flow where the shear stress would decrease. But the presence of the oil could cause the flow to separate, effectively trapping it in this particular region. On the pressure side of the blade, there is also a weak trace of what looks like shock induced into the flow by the tie-boss. This assumption is to be taken with a grain of salt as it is not sure that there would be supersonic flow in the vicinity of the tie-boss at all and there was no video recorded of the pressure side of the blade.

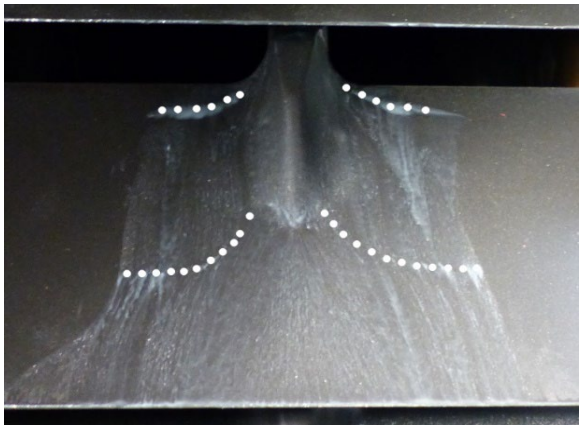

Figure 38 – Surface flow visualisation on the pressure side of the tailored tie-boss interblade channel.

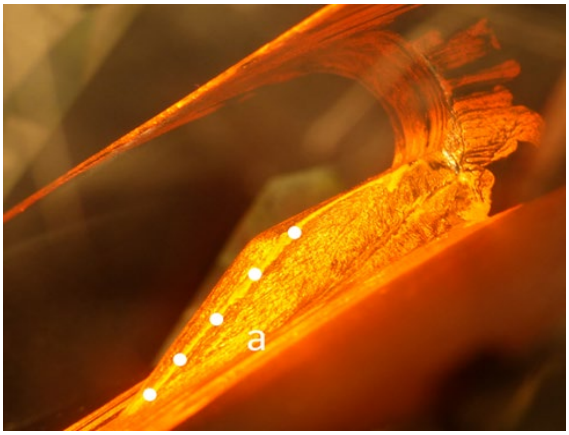

Figure 39 – Surface flow visualisation on the side of the tailored tie-boss.

The surface visualisation in the interblade channel of the tailored tie-boss is shown in Figure 38 and Figure 39. In the first mentioned image, there is a set of traces on the suction side of the blade. The upper trace does not correspond to any aerodynamic phenomenon. The trace is formed as the mixture stets after shutting the tunnel off. This mixture behaviour has been observed on the video of the experiment. The quality of the video is, however, insufficient for capturing of an image. The regions further downstream do not seem to be affected in any significant manner. The mixture used for this visualisation was the magnesium diluted in kerosene, it was less viscous and less visible. Lower viscosity of the mixture presumably decreased influence of the coat on the flow field but increased mixture flow after the tunnel shut off. The lower trace is again attributed to the impingement point of the inner branch of the exit shock wave. It is again curved, presumably for the same reason as in the case of oval tie-boss. The side view of the tie-boss shows another trace which is thought to have been caused by a vortex because of the streamlines turning away from this trace, which is expected result of the rotational motion of the fluid.

7.4. Conclusions of experimental investigation

Experimental investigation showed that the effects of the tie-boss presence in the flow field are significant. All the parameters of the flow are influenced. Most notably, there is quite large change in the exit flow angle for both types of the tie-boss. There is also significant loss of kinetic energy, as is expected due to the fact that tie-boss presents an obstruction of the flow. The tailored tie-boss with flat trailing edge causes much larger loss, presumably as the result of massive flow separation that occurs on back facing flat surfaces in the flow field and is sure to have occurred on the tie-boss too. The oval tie-boss causes larger flow turning, interestingly, outside the area of the tie-boss itself. The investigation showed that understanding the flow field in the interblade channel equipped with the tie-boss is crucial for possible optimisation of the flow field.

8. Numerical simulation

8.1. Numerical simulation setup

In order to investigate the flow field thoroughly, both tie-boss geometries have been numerically investigated. Numerical solvers used were Ansys Fluent and Ansys CFX. Both the solvers are able to run the simulation on a mesh with non-homogenous interfaces.

The computational domain was 160 mm wide, as is the test section in aerodynamic laboratory in Nový Knín. Periodic boundary conditions have been assumed on top and bottom of the domain. Sides of the domain were assumed as adiabatic no slip walls, as were the blades and tie-boss bodies themselves. The inlet total temperature was set to $T_{tot} = 298$ K. The inlet velocity pressure profile was set with accordance to the measured values of total pressure in the wind tunnel. In the region $z \in (0; 18.75)$ mm the total pressure was given by equation 9.1.1, which was derived from a distribution measured in [28]. In the middle of the zone the total pressure was set to $p_{tot} = 100\,000$ [Pa]. In the region $z \in (141.25; 160)$ mm, the total pressure was provided by negated equation 9.1.1. Although sensitivity testing showed that the inlet profile does not have any significant influence on the flow parameters outside the nearest 10 mm from the side walls. The inlet turbulence intensity was set to 1 %, as this was the closest value to 1.7% that numerical solver allowed. The direction of the flow was set to be parallel to the axis of the turbine, inlet velocity vector corresponded to inlet angle $\alpha_1 = 30.9°$. The outlet average static pressure $p_{s,ave} = 3 \cdot 10^4$ Pa has been set, with the blend factor of $q_{blend} = 0.05$. The outlet pressure corresponds with outlet Mach number $M_2 = 1.44$. No non-reflective outlet boundary conditions were employed.

$$p_{01} = \left(\frac{z}{0.01875}\right)^{\frac{1}{2.8}} + 92000\ [\text{Pa}], \qquad z \in \langle 0; 18.75 \rangle \tag{9.1.1}$$

Mesh for both the cases was made with non-homogenous interfaces. Both meshes have been made utilising Ansys ICEM. Vicinity of the tie-boss body had always been modelled with unstructured tetrahedral mesh with boundary layer refinement. The first layer's height had been set to $y_1 = 0.006$ mm for expected value of $y^+ = 1$ for expected flow conditions. The interface was shaped specifically to allow perpendicular cells in the area of the boundary layer. The remaining area was meshed using structured mesh. The division of the computational domain was adapted concerning the total number of elements and quality of results. Prior testing has shown that although the CFX is unstructured solver, quality of results was higher on structured mesh, while at the same time being faster and less demanding computationally wise. The structured mesh was desirable wherever it could be modelled. The complicated shape of the tie-boss body prevented generating structured mesh in its vicinity, so the octree flooding with post flooding boundary layer refinement extraction has been utilized. The structured mesh modelling is being done via user-controlled blocks which determine number and

shape of the mesh. The shape of connection between the meshes in case of oval tie-boss is shown in Figure 49. Shape of the computational domain was different for each tie-boss type. The second tie-boss has the tailored trailing edge. Thus, significant flow field phenomena were expected, and the domain for both tie-bosses was chosen so the interblade channel would not be cut in half. Instead, the blade was cut in half and the interblade channel is modelled undivided without any periodic interface. There have been concerns regarding modelling of the blade wake in this approach.

8.2. Mesh sensitivity

Mesh sensitivity was evaluated in the simulation of reference case cascade. The choice of reference cascade was purely practical, modification of structured mesh could be better controlled, and the metric of mesh finesse could be better defined. For mesh sensitivity analysis, five meshes were created. Four had identical geometry while one was prolonged to determine the effect of a longer domain on the flow field in the vicinity of the blade.

Table 3 – Generated meshes.

Geometry	Nr. of cells [mil]	Cells along blade	Alias
Long	10.1	188	Finest long
Short	6.3	188	Finest short
Short	3.8	142	Fine
Short	1.4	107	Medium
Short	0.82	72	Coarse

The meshes were created in Ansys ICEM. All the meshes were created as structured and then converted into unstructured meshes. Periodic boundary conditions on top and bottom of the domain were conformal with 1:1 face ratio. To prevent a shock wave reflection from the outlet boundary layer, a coarsened area has been introduced, see Figure 40. This solution, however inelegant, proved to be the most reliable way of dealing with reflected shock waves. Any kind of software non-reflective boundary conditions in both Ansys CFX and Fluent always lead to change in aerodynamic conditions at the boundary and thus to different flow fi eld parameters.

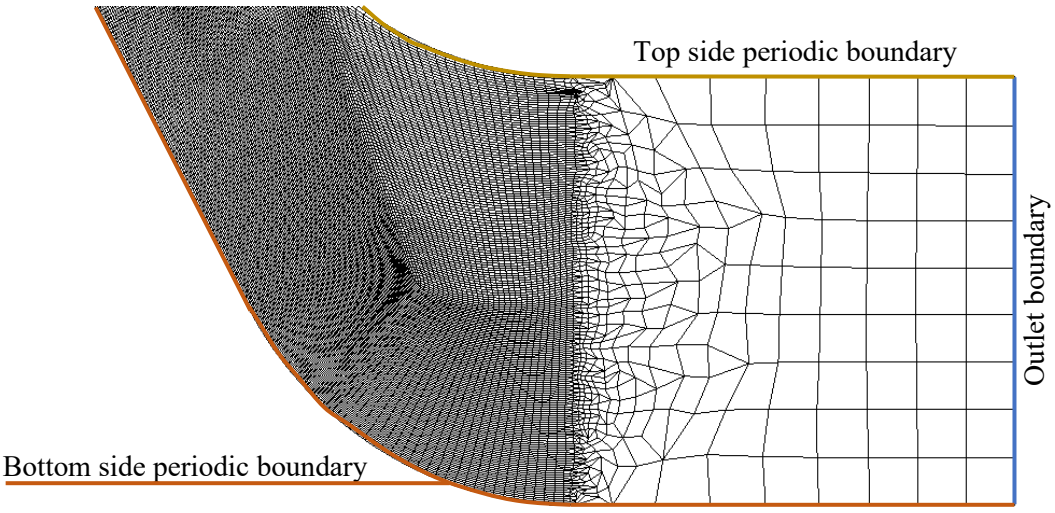

Figure 40 – Side view of the coarsened outlet area of the mesh with marked periodic boundaries and outlet. Upstream parts of the mesh were cut out of this picture.

Firstly, the simulations were done using Ansys CFX. Therefore, first part of mesh sensitivity analysis was performed in the CFX. Prior to the presented simulations, many more were performed in an effort to evaluate the influence of different meshing style on the results of the simulations. CFX does not allow implementation of non-reflective outlet boundary condition unless the boundary is set supersonic which does not allow for setting of backpressure, thus rendering it useless. Setting the outlet boundary condition as subsonic does not limit the velocity of the flow.

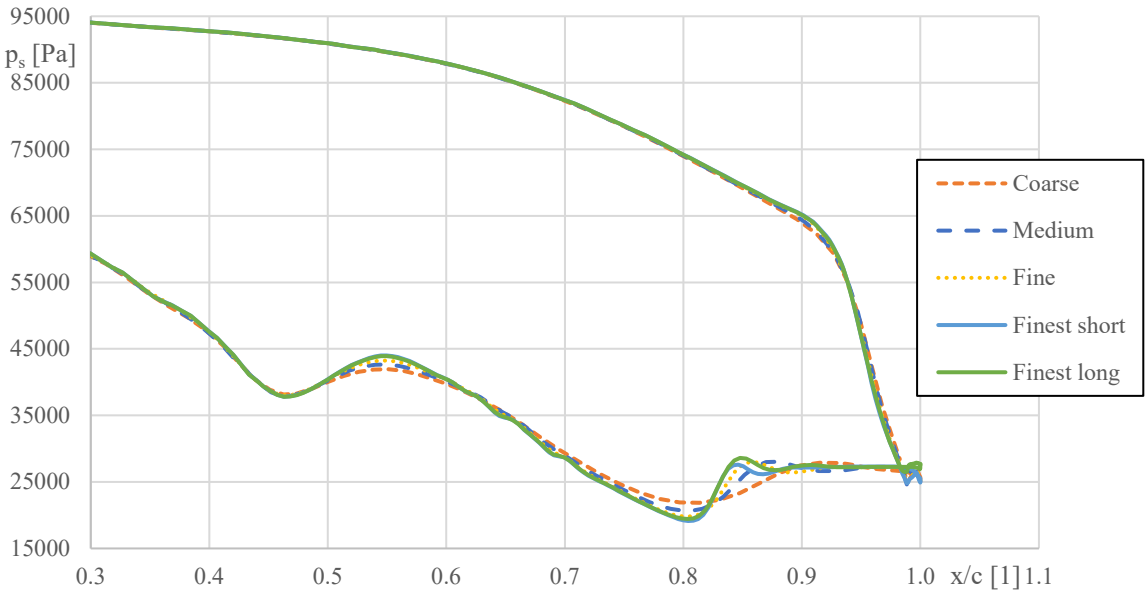

Figure 41 – Pressure distribution along the trailing area of the blade from simulations in Ansys Fluent.

In the Figure 41 there is pressure distribution on the surface of the blade in the middle of the channel. Only the interesting regions containing all the interactions and the trailing edge are shown for the better readability of the results. It is apparent that the Finest long and Finest short meshes are a very close match, while each subsequent coarser mesh did smooth the individual flow phenomena, omitting some altogether. This effect is particularly drawn in the area of interaction of inner branch of the exit shock wave of the adjacent blade with suction side of the examined blade.

However, during the detailed flow field examination, a strange behaviour of total pressure was observed. In certain regions, total pressure would exceed the inlet total pressure, thus forming regions of negative losses, see Figure 42. Along with total pressure, total temperature would often be higher than inlet total temperature. These regions were present in all examined meshes albeit with somewhat different size. Location of the zones is always similar. The zones are present near shock waves and before the shock wave reflection was eliminated, there were increased total pressure zones at the outer edge of the wake of the blade. In coarse mesh, the zones are also present in aeras of fast expansion in the interblade channel.

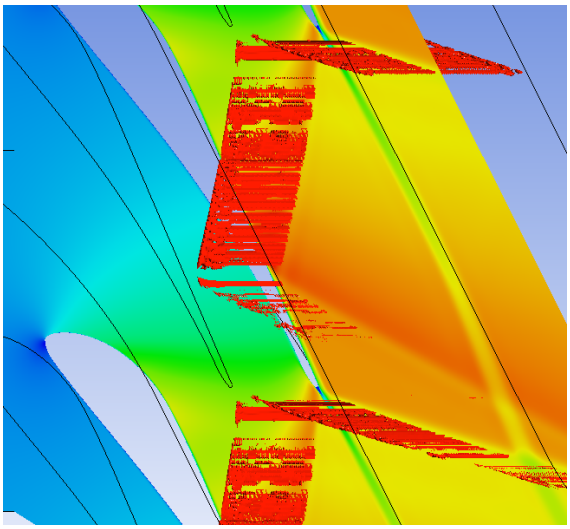

Figure 42 – Finest long mesh, isosurface of p_{tot}=100300 Pa.

First suspect in the investigation of the origin of the effect was viscosity. Simulation with different turbulent viscosity models were performed. Among the tried were the shear stress transport, BSL EARSM and k-ω models. There was also an attempt to run the simulation as laminar with no turbulent viscosity model employed. However, investigation of turbulent viscosity in the flow field pointed the suspicion away as there were no extreme or negative values of viscosity present in the flow field. Molecular viscosity was also suspected resulting in running a simulation with inviscid ideal gas and also with molecular viscosity calculated by the Sutherland's formula. None of the mentioned had any positive influence on the zones of increased total pressure. All the simulations were well converged,

judging not only from the residuals but also from the in-solver imbalances. As viscosity was ruled out as the source of negative loss, attention was shifted to the advection scheme of the solver. However, user has a very limited influence over the advection scheme. The only modification available is omission of the viscous work term $\nabla \cdot (\mathbf{U} \cdot \tau)$ from the equation 9.2.1. This option marginally worsened the increased total pressure zones.

$$\frac{\partial(\rho h_{tot})}{\partial t} - \frac{\partial p}{\partial t} + \nabla \cdot (\rho \, \mathbf{U} \, h_{tot}) = \nabla \cdot (\lambda \nabla T) + \nabla \cdot (\mathbf{U} \cdot \tau) + \mathbf{U} \cdot \mathbf{S}_M + \mathbf{S}_E \qquad 9.2.1$$

Consequently, an investigation of the theoretical values of total pressure was conducted. The outer branch of the exit shock wave was chosen for investigation. The total pressure increase was present, although investigation showed that there is a dip in the value of total pressure just behind the increase. Because analytical decomposition of solver behaviour was outside the realm of possibilities, the theoretical investigation was the only option left. The relations used for the investigation were obtained in [12].

$$p_{02} = \frac{p_{01} p_2}{p_1} \left[\frac{1 + q^2 (M_2^2 - 1)}{1 + q^2 (M_1^2 - 1)} \right]^{(1+q^2)/2q} \qquad 9.2.2$$

The substituted parameter q is defined in 9.2.3.

$$q = \left(\frac{\kappa - 1}{\kappa + 1} \right)^{0.5} \qquad 9.2.3$$

During the process of investigation, it was found out that the equation 9.2.2 is very dependent on the accuracy of input parameters. After exact parameters extraction, the theoretical value of total pressure downstream was obtained and compared to the value of total pressure extracted from the numerical solution. The difference of the two values was less than 1 Pa. Therefore, despite the existence of the increased total pressure zones, the numerical solver was deemed dependable.

The Fluent solver was set consistently among the tested cases. The implicit formulation of the advection scheme was selected with the AUSM flux vector computation method. The warped-face correction option was turned on. The spatial discretisation was set to second order upwind for all quantities. There was also a small area of increased total pressure, but this has been in the vicinity of the leading edge of the blade and magnitude of the excess pressure was lower by two orders. Thus, solutions from the Fluent were deemed reliable.

The evaluation of mesh quality started as evaluation of kinetic energy loss coefficient in expectation of obtaining clear distinction as the coefficient would settle on a value corresponding to the experiment as the mesh got fine enough. The results are in Table 4. The kinetic energy loss coefficient was evaluated using the 2-D data reduction method and the value represents middle of the channel on the traversing plane equivalent to the experimental investigation.

Table 4 – Relative kinetic energy loss coefficient in the middle of the channel.

Mesh	$\zeta_{Fluent,\ relative}$	$\zeta_{CFX,\ relative}$
Finest long	0.990	0.990
Finest short	0.993	0.987
Fine	0.987	1.083
Medium	0.990	1.063
Coarse	1.010	1.067

It is clear that the difference between the evaluated meshes are marginal for the Fluent solver and quite substantial for the CFX. The finest meshes, however, converged to the same value. In case of the Fluent, however, this metric could not be used. Therefore, a less precise metric had to be employed. The flow phenomena present in the finest simulations cannot be missing in the coarser ones should they represent the flow field with enough fidelity. In Figure 43 and Figure 44 there are flow fields from the simulations on finest and fine mesh. Both share same colour mapping, therefore only Figure 44. Mutual comparison of the finest long mesh and finest short mesh, which differ almost exclusively by the length of area downstream of the blade cascade showed that the prolongation did not have any noticeable effect on the flow field. Therefore, the long mesh has not been considered for the comparison. The Finest and the Fine mesh are visually very similar. Both capture transonic recompression, shock waves are sharp, and interactions are clearly visible. Albeit the quality of the simulation of the Finest mesh is superior.

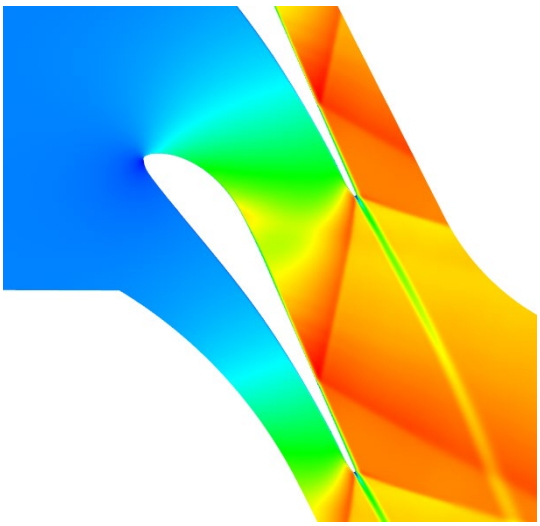

Figure 43 – Mach number distribution in the middle of the channel for Finest short mesh.

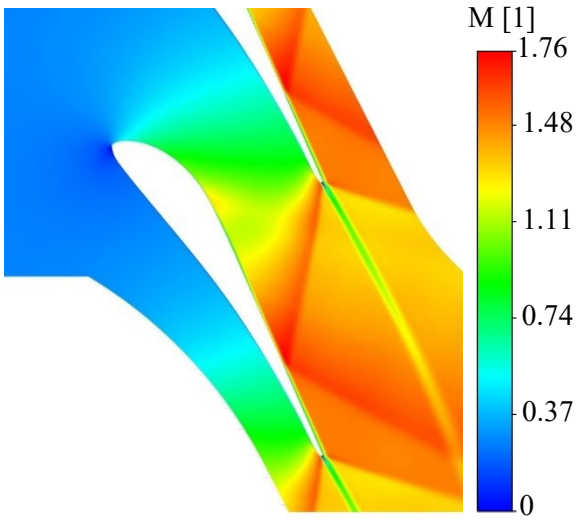

Figure 44 – Mach number distribution in the middle of the channel for Fine mesh.

In the Figure 45 and Figure 46 there are flow fields of Medium and Coarse mesh respectively. While both medium and coarse mesh captures transonic recompression, the shock waves are blurred. The reflection of the inner branch of the shock wave can still be seen in Medium mesh case, it is completely blurred in the case of the coarse mesh. In both these cases, the interaction of shock wave and boundary layer is hardly visible and the Mach number behind the reflected shock is visibly higher than in the case of finer meshes. Both the coarser meshes were deemed inadequate.

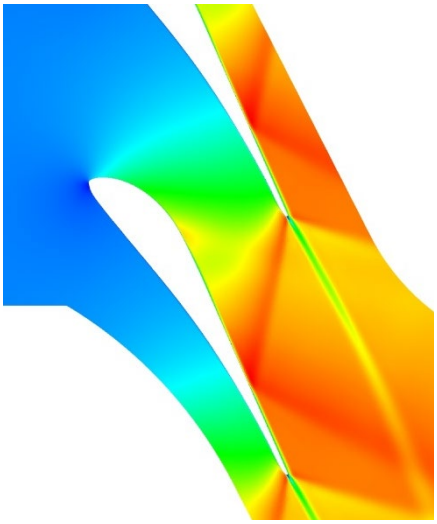

Figure 45 – Mach number distribution in the middle of the channel for Medium mesh.

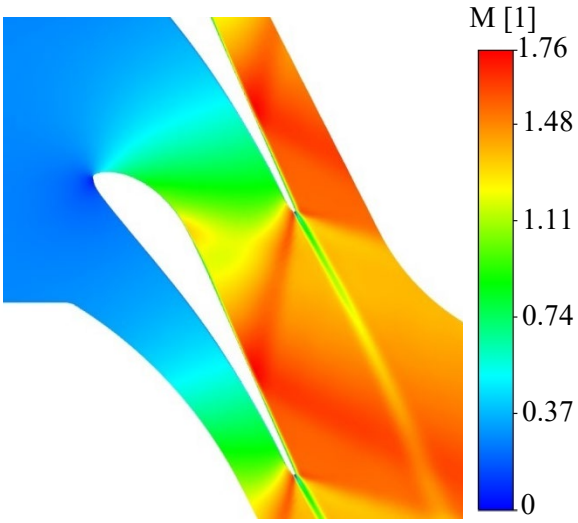

Figure 46 – Mach number distribution in the middle of the channel for Coarse mesh.

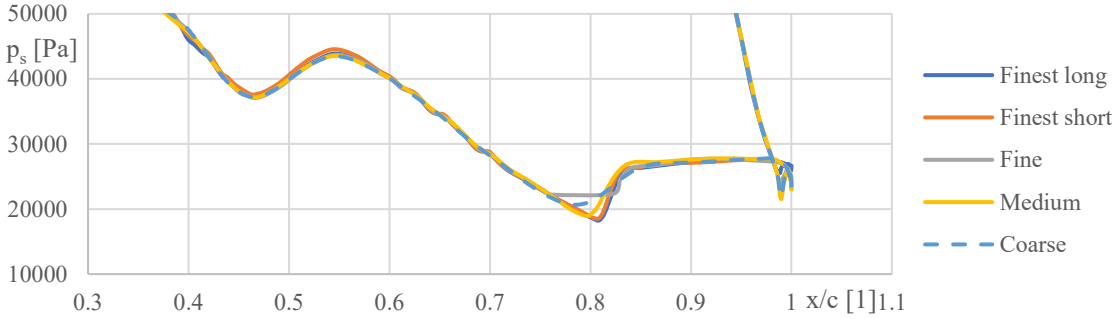

Figure 47 – Static pressure distribution along the blade for different meshes in the middle of the height of the blade from simulation in Ansys CFX.

The comparison of the static pressure distribution on the surface of the blade in the Figure 47 confirms findings of the visual investigation of the flow field quality. The Finest meshes show very precise points of shock wave interactions with the boundary layer on the surface of the blade. The simulation of Fine mesh has blurred part of that interaction. Therefore, the Finest mesh was chosen as suitable for simulations with the tie-boss. It is common practice to provide simulation with finer mesh than the mesh that was chosen. However, this simulation was not provided for practical reasons. The computational time on the Finest mesh was in the order of days and the size of the simulation made it impractical even on available computational servers.

8.3. Computational mesh

The computational mesh has been created in Ansys ICEM. Because of the complicated geometry of tie-boss, which could not have been simplified in order for the simulation to be able to assess the influence of the notch and various geometrical features on the flow field, the mesh generation could not be done with the blocking technique alone and unstructured mesh generation algorithms have been utilized as well.

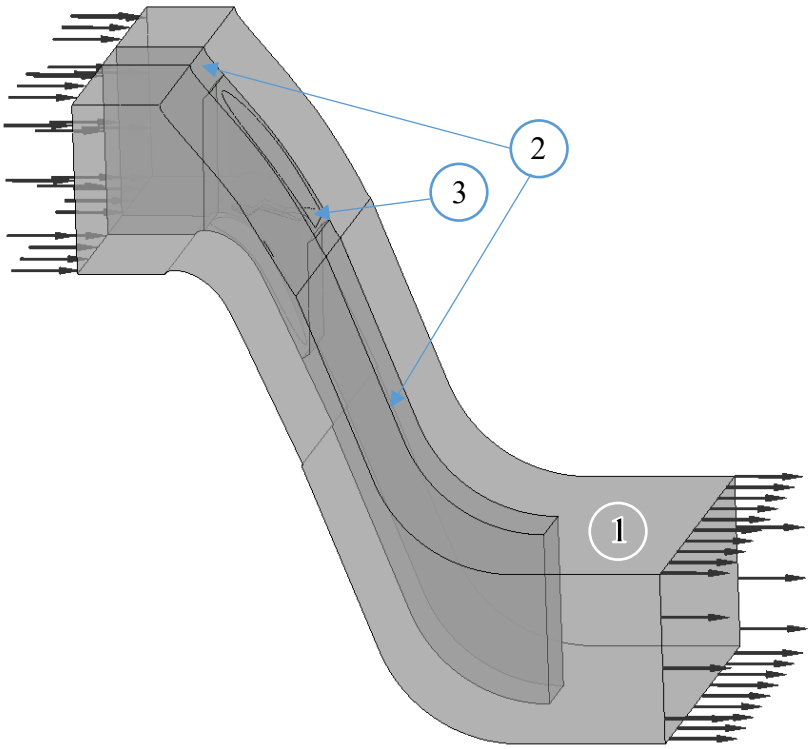

Figure 48 – Zoning of the computational domain.

The computational domain has been split into three areas labelled 1, 2 and 3. The outer structured mesh, the inner structured mesh and the unstructured mesh in the proximity of the tie-boss itself. The outer structured mesh region, designated by the number 1 in Figure 48, contains the outlet coarse region to prevent the exit shock wave boundary reflection. The inner structured mesh region, designated by number 2, is tailored to accommodate the unstructured mesh around the tie-boss itself. The regions 1 and 2 are meshed using the blocking technique where the user has full control of the generated mesh. The blocks are arranged throughout the zone and precise number of hexahedral elements is created on each edge of each block. This way, conformal mesh on the periodic boundary condition is created. This method, however laborious, yields the best results in terms of mesh quality. Although Ansys Fluent is unstructured solver, it does also benefit from a mesh with hexahedral prisms. The inner unstructured region, designated as 3, contains unstructured mesh which is flooded around the tie-boss. The flooding algorithm used is called octree, which expands elements around the meshed region and then divides then until the boundaries are well filled. This method does not allow

very precise mesh control and can only be controlled via set of parameters, it is however less laborious and will fill the very complicated geometry. Cut through the middle of the domain is shown in Figure 49. It is also worth noting that the unstructured mesh generation has around 5 times worse elements to volume ratio. The boundary layer in the unstructured mesh is created after the mesh generation, using the so-called post inflation algorithm.

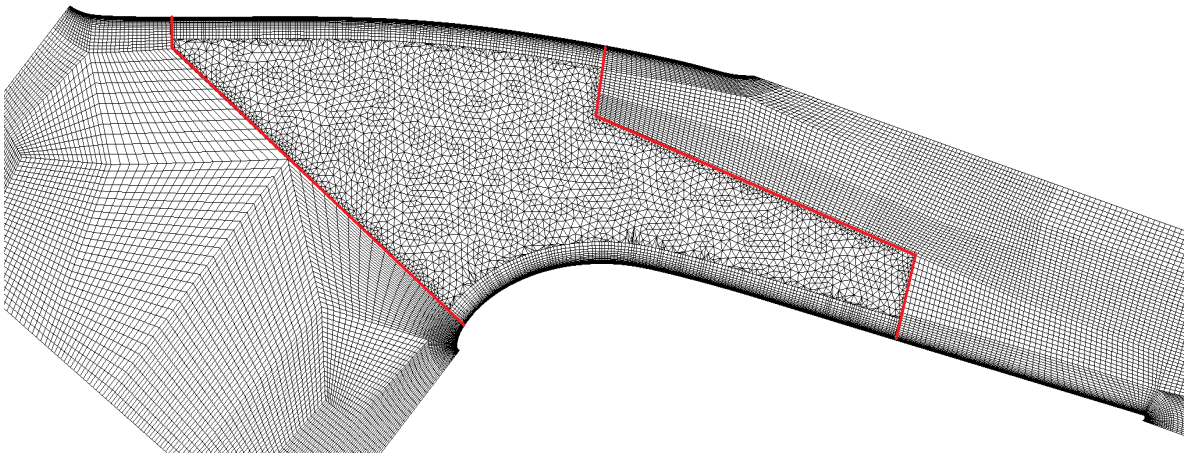

Figure 49 – Tailored tie-boss non-homogenous mesh interface.

The oval tie-boss computational mesh has a shared design with exception of the downstream step in the interface. The outer meshing regions are identical, and the inner meshing regions are very similar.

9. Results of numerical simulation

The y^+ was in the region of 1 to 1.5 in most key areas, below 3 in all the other areas of the blade and tie-boss. Although Ansys CFX is equipped with automatic near wall treatment that is able to deal with arbitrary y^+, approach with $y^+ < 2$ would lead to switch to low Reynolds number formulation model to resolve the viscous sublayer providing greater solution accuracy.

For the purposes of examination of the flow field, section planes have been inserted into the domain. The section planes placement has been done with the goal of having the ability to spot vorticial structures. Therefore, planes have been placed perpendicularly to the local flow. Although the mesh sensitivity analysis proved that both the solvers provide accurate results in the finest mesh, ultimately the CFX was chosen for its familiarity to the author and because of ease of implementation of the non-homogenous mesh interfaces.

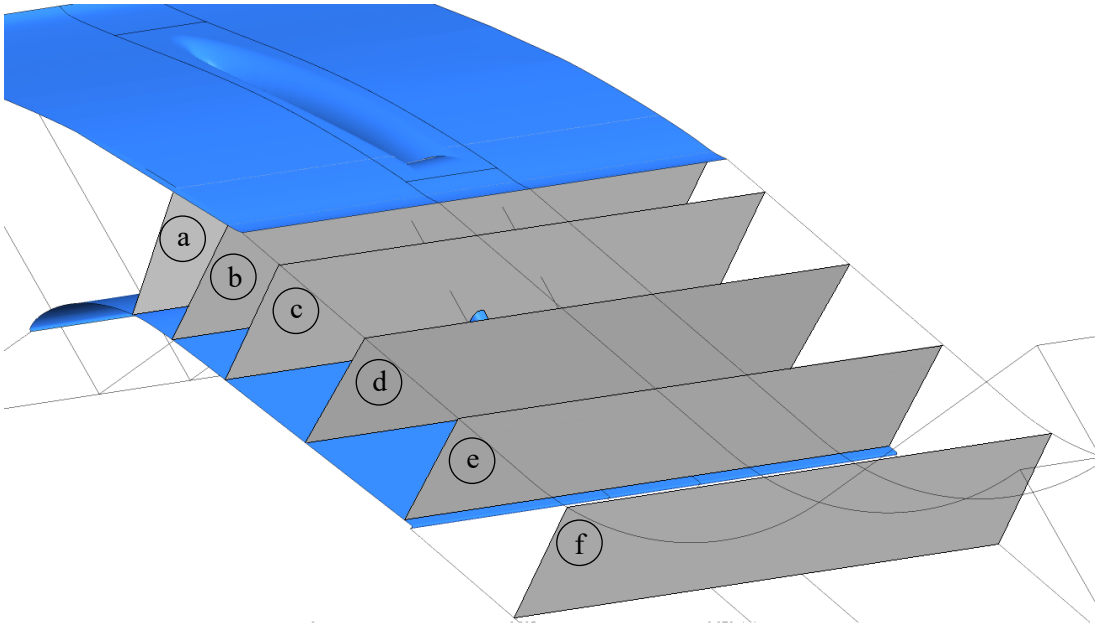

Figure 50 – Locations of cut planes used for flow field evaluation: a – x/c = 0.217; b – x/c = 0.323; c – x/c = 0.471; d – x/c = 0.703; e – x/c = 0.983; f – x/c = 1.308.

9.1. Sonic conditions – tailored tie-boss

The tie-boss body presents a considerable obstruction of the interblade channel and therefore a profound influence on the shape of the sonic surface is expected. The influence is clearly both from the tie-boss body and from the vortices that are generated by the tie-boss presence.

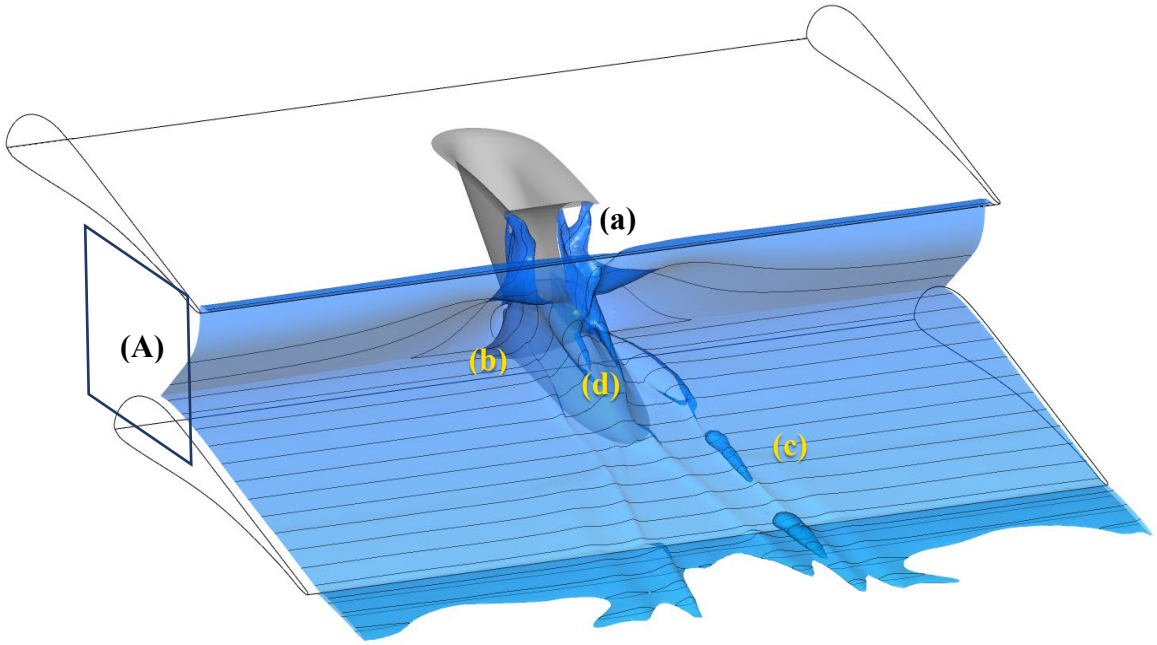

Figure 51 – Overview of surface plane in interblade channel of the tailored tie-boss with marked viewpoint (A) of the Figure 52.

In Figure 51 there is a sonic surface visualization, where M = 1. It is clearly visible, that the surface does not have constant shape in the direction of the height of the blade. There is a considerable upstream buckling in the area (b). The detail of the earlier transition to supersonic velocities is in Figure 52. The sonic surface has shifted upstream by $\Delta x/c = 0.098$. The lines on the sonic surface in Figure 52 are isolines of the coordinate z, along the span of the blade.

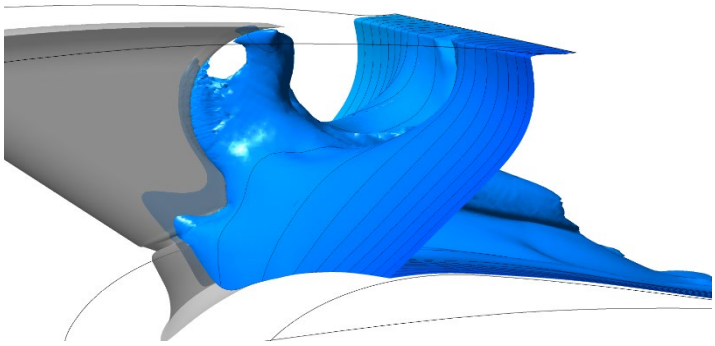

Figure 52 – Detail of the sonic surface position from side-view (A); see Figure 51.

There are visible supersonic fins just outside the wake of the tailored part of tie-boss, marked by (a) in Figure 51. Maximal Mach number inside the fins was found out to be M = 1.05. Therefore, only weak shock fans or very weak shocks can be expected at their ends. Nevertheless, the fins end before the final transition of the flow to supersonic velocities and small shocks are to be expected. The area around the fins had very high pressure and density gradients, therefore no reliable shock visualisation could be made. In Figure 53, there are density gradient contours with sonic line marked. It is clearly visible that the contours are disturbed or jagged near the end of the supersonic area, but it is impossible to tell whether this is due to a set of weak shocks or individual mesh control volumes. Elaborate analysis of the fins is regrettably outside the resolution of this numerical simulation.

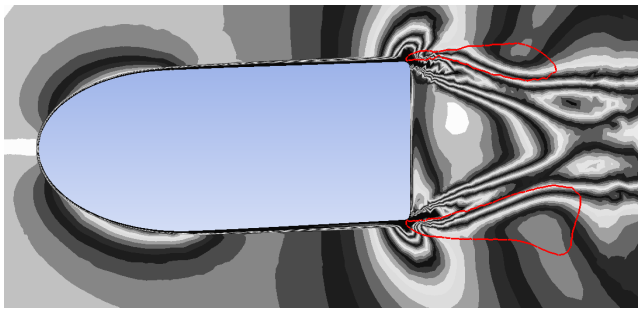

Figure 53 – Density gradient contours with sonic line (red) showed in a plane cutting through upper part of the tailored tie-boss.

The marks (c) and (d) in Figure 51 are clear traces of vortices. There are areas of very low momentum close to the surface of the blade and tie-boss, which will be discussed later. Vortices do transport this low momentum fluid further away from the surface, delaying transition to supersonic velocities. There are several vortices in the interblade channel, which will be talked about in the upcoming paragraphs. Most profound vortices at mark (d) originate at the beginning of the oval part of the trailing edge. The vortex core at (c) clearly decelerates to subsonic speeds twice, as it passes through the inner branch of exit shock wave of the adjacent blade and its reflected counterpart. This behaviour is attributed to its massive size and also the fact that it passes a region of very low momentum.

9.2. Sonic conditions – oval tie-boss

The oval tie-boss sonic surface is shown in Figure 54. It is clear that it is much less disturbed than in the case of the tailored tie-boss. Almost all of the transition to supersonic flow velocity happens before the flow passes the trailing edge of the tie-boss body. As in the previous case sonic surface has shifted upstream. The shift is much less profound at $\Delta x/c = 0.037$.

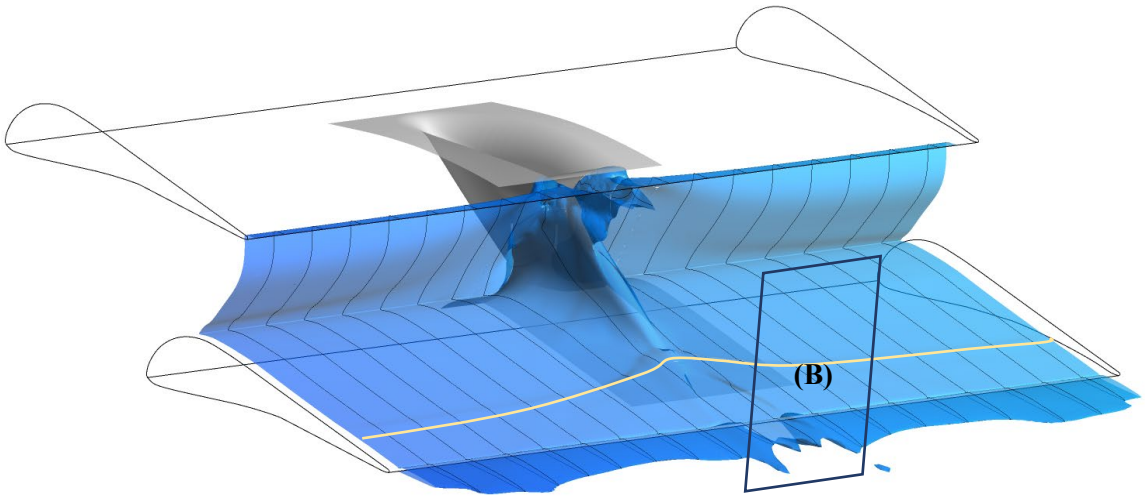

Figure 54 – Sonic surface in interblade channel with oval tie-boss with marked viewpoint (B) of Figure 55.

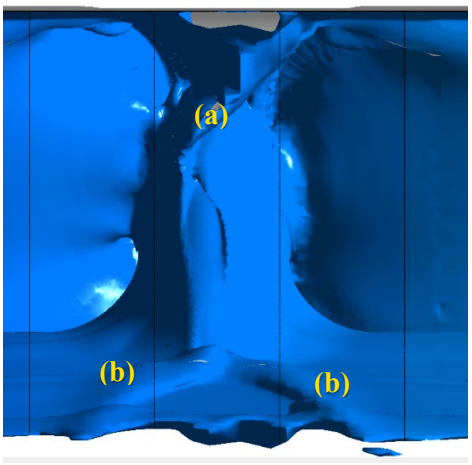

Figure 55 – Detail of subsonic pocket behind oval tie-boss trailing edge (B); see Figure 54.

There is a subsonic pocket at the top of the tie-boss body, which stretches to around 60% of the height of the interblade channel. Its size is not very significant, and its shape is influenced by the presence of large vortical core. In Figure 55 there is a very clear diagonal shape (a) of the sonic surface. This shape is formed as a result of transport of the fluid by vortices. There are also clearly visible boundary layer swells (b) on the suction side of the bottom blade as there are strong interactions between the boundary layer and vortices that are adjacent to the trailing edge of the tie boss. However, no negative values of skin friction coefficient were found as well as no backflow is occurring in the boundary layer. Absence of these phenomena suggest that the flow is not separated in the boundary layer of the blade. There is also a small subsonic region behind the trailing edge of the bottom blade. This flow deceleration is in the middle of vortex core and is attributed to passage of the vortex trough reflected inner branch of exit shock wave of the bottom blade which is deformed by the tie-boss presence.

9.3. Shock wave configuration – oval tie-boss

Transonic flow conditions in the mid-section interblade channel will induce shock waves in the flow. Shock wave interactions with the blade surface are also expected to occur, resulting in the shock wave reflection. Shock waves are also expected to be influenced by the tie-boss wake or possibly by the vortices that tie-boss induces into the flow field. The shock wave configuration was examined by author in [R2]

Shock wave visualisation is quite troublesome, as the properties of the flow that are in the shock wave are also in the boundary layer, in the vicinity of the wake and sometimes in the vortical structures. The traces of shock waves identified in the flow field are shown in the Figure 56. The shock waves were visualised as values of density gradients in respective coordinate axis directions which were later clipped by the span-wise coordinate to eliminate gradients in the vicinity of the side walls of the tunnel. The greyscale colouring of the isosurfaces has been chosen to roughly correspond to pitch-wise coordinate to better depict shape of the surfaces and it does not bear any physical qualities.

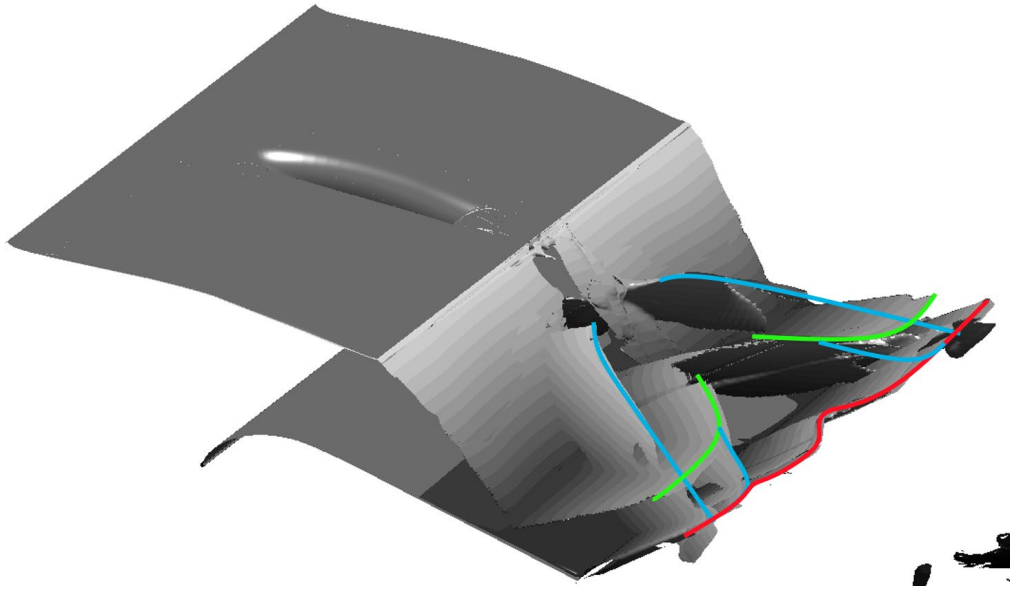

Figure 56 – Shock wave traces in the oval tie-boss interblade channel.

In Figure 56 the traces of the shock waves have been visualized. The traces are at intersection of shock waves with the top periodic boundary condition. The red trace belongs to the outer branch of the exit shock wave of the bottom blade. It is apparent that the trace is not straight, it has curvature in the middle and the shock wave actually appears to have moved upstream. This configuration has occurred because of the lower Mach number in the wake of the tie-boss and therefore different angle β of the shock wave. This distortion is present in the shock wave generated on the trailing edge of the blade and is repeated in reflected shock. There are also two other smaller curvatures caused by the turning of the flow by the passing of another shock waves, depicted by the blue traces.

The green trace belongs to the reflected inner branch of the exit shock wave of the upper blade. The inner branch of the shock wave impinges suction side of the adjacent blade and causes interaction with the boundary layer. This interaction causes growth of the boundary layer which can be seen in the small curvature of sonic surface near the surface of the blade, marked by yellow line, in Figure 54. The turned flow is then deflected by the surface of the blade and reflected shock wave is created. Because of ongoing expansion, the upstream Mach number for the reflected shock is greater than the upstream Mach number of the exit shock itself. Therefore, the reflected shock wave angle $\beta_2 = 36.8°$ is slightly smaller than the original shock wave angle $\beta_1 = 37.8°$. These angles were evaluated in the free stream region of the interblade channel where there is no direct influence of the tie-boss wake or vortices. There is also smaller curvature further away from the middle of the channel, which is again caused by the interaction with the shock wave depicted by the blue trace.

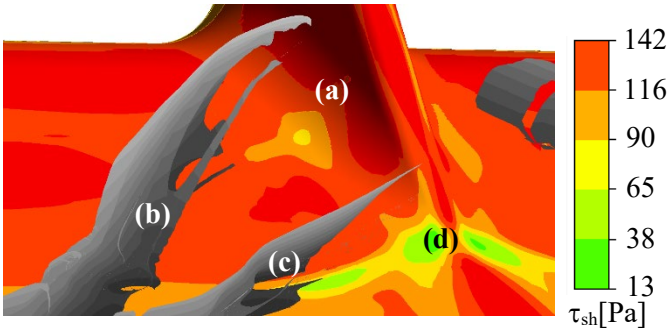

Figure 57 – Detail of trailing edge of oval tie-boss with shock waves and wall shear stress visualization.

Shock waves depicted by the blue trace originate on the root of the tie-boss body. Detail of the point of origin of the shock near the trailing edge of the tie-boss is shown in Figure 57. The contour on the surface of the blade depicts wall shear stress in the approximate direction of the flow. There are no negative values of shear, therefore there is no flow separation in this part of the flow field. Marked (a) is a drop of wall shear value indicating slow of the flow just downstream of the origin of the shock wave. Due to ongoing expansion in the interblade channel, the wall shear increases again as the flow accelerates. Marked by the letter (b) there is the subject shock wave which has blue trace in Figure 56. It is also worth mentioning that there is no inherent shock wave visualisation physical property in the solver. As mentioned before, density gradient iso-planes are utilised. The iso-plane always has two sides as the gradient passes the set value twice, once ascending the threshold and once descending it. The actual shock will be positioned in between those two gradient iso-planes. The mark (c) shows reflected inner branch of the exit shock wave, marked by green trace in Figure 56. The mark (d) is in a place of much more pronounced drop of wall shear. This is the place of the interaction between the inner branch of the exit shock wave and the blade. Unfortunately, the area near the trailing edge of the tie-boss contains very significant flow phenomena, therefore density and velocity gradients are high, and method of shock wave visualisation is blurred. It can be safely assumed that above the trace, the

interaction really occurs even though the shock wave itself could not be easily visualized. Therefore, a 2D visualization method was chosen, see Figure 58.

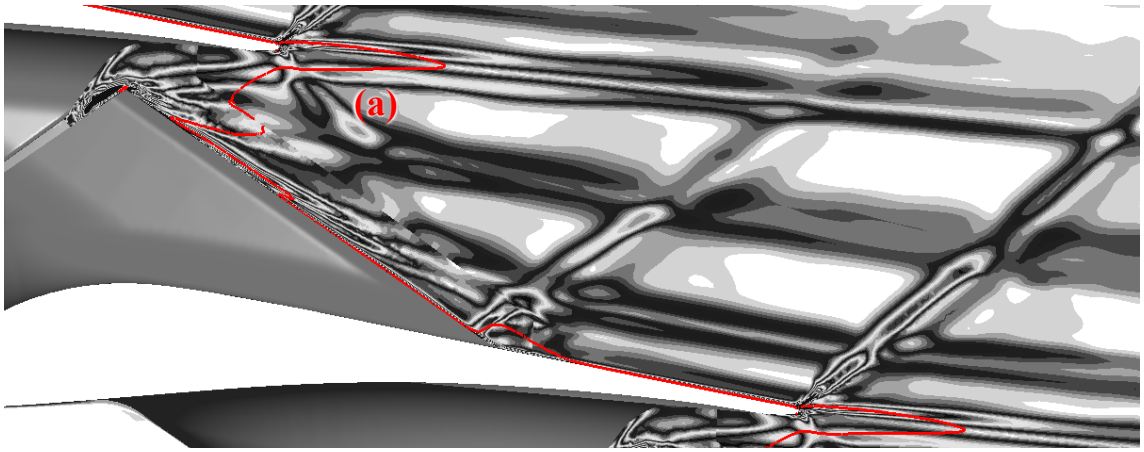

Figure 58 – Visualization of density gradient in a plane parallel to the flow with red sonic line.

The visualisation of density gradient allows some insight into the flow field. Namely it is clear that there is subsonic flow below the trailing edge of the blade in the tie-boss wake. Therefore, although there is compression – expansion disturbance (a) in the flow where shock wave would be expected, it is hard to confirm that there is one. No flow turning could be reliably observed as a consequence of flow passing through this disturbance, although this is given by the limited resolution of the calculation method.

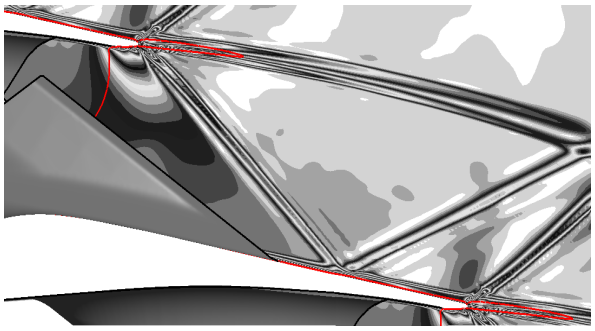

Figure 59 – Free stream shockwave configuration with sonic line and tie-boss shown in a plane behind the tie-boss.

There is also the shock wave which appears to emerge from the trailing edge of the tie-boss. In this particular cut it also appears that it is normal to surface, hence the subsonic area downstream. It must be remembered though that the flow past the tie-boss is complex and size of this subsonic region is very limited. The direction of the flow then changes and the shock changes from normal to oblique. As show in Figure 57 (d), the trace of wall shear stress decrease is continuous from the free stream region onto the trailing edge of the tie-boss. Therefore, it is assumed that the exit shock wave disturbance propagates trough the subsonic area near the trailing edge is a continuation of the free steam shock. In Figure 59 there is same density gradient distribution in the free stream region of the interblade channel. It is apparent that the shock wave is clearly pronounced, and impingement point with suction side of the blade is downstream compared to the shock wave in the tie-boss wake. It is also quite clear that angle of the wake relative to the blade chord changed. The difference of the angle measured in a distance x/C = 1.25 was 1,17°. This change has been clearly influenced by the vortices present in the wake of the tie-boss and also by different shock wave angle in the wake.

9.4. Shock wave configuration – tailored tie-boss

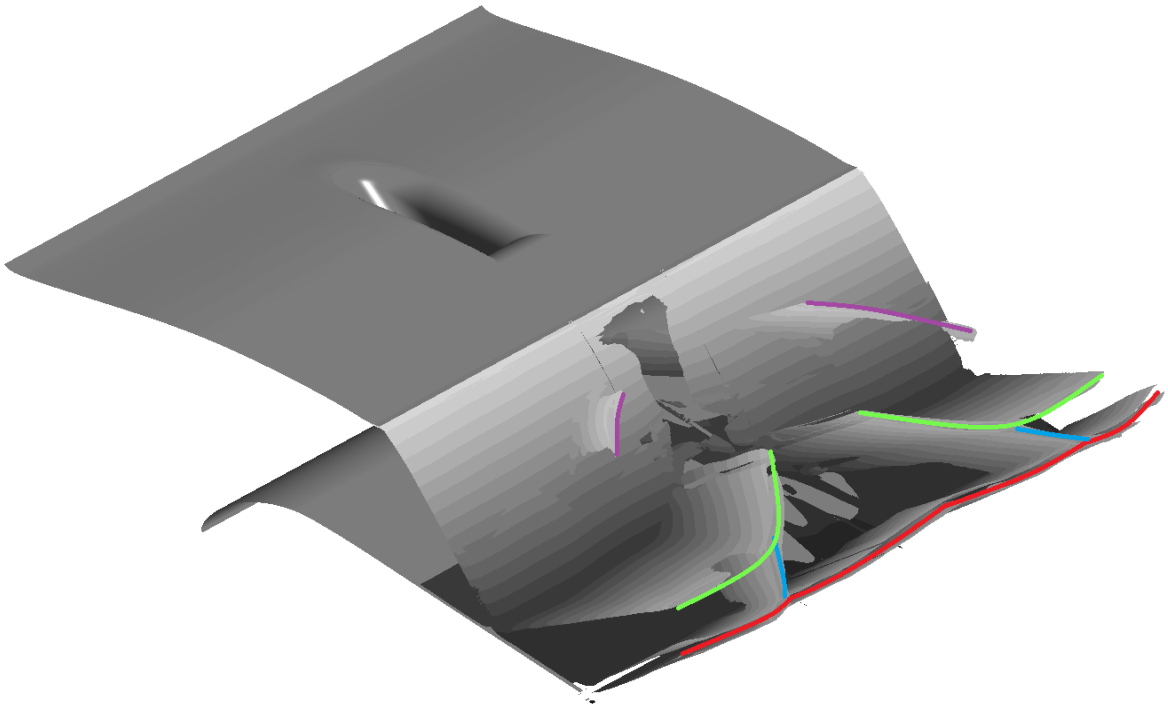

Figure 60 – Shock wave configuration in the tailored tie-boss flow field with shock wave traces.

A visualisation similar to the oval tie-boss one is shown in Figure 60. Red trace depicts the intersection of lower blade exit shock wave with the top periodic boundary condition. The trace is clearly straighter than the trace of the exit shock wave behind the oval tie-boss. Limited disturbance can still be observed in the area of the tie-boss wake, but it is very minor. The angle of the outer branch of the exit shock wave was between $\beta_{min} = 47.4°$ and $\beta_{max} = 53.3°$. There are also visible curvatures as the intersection of the exit shock wave and shock waves originating at the intersection of the trailing edge of the tie-boss and the suction surface of the blade, which are marked by blue line.

The configuration of shock waves in the flow field is quite similar to the configuration in case of the oval tie-boss. There is a large upstream deformation of reflected inner branch of exit shock wave, which is marked by green line. The impingement location can be seen in the Figure 51 as a slight growth of the distance between the blade surface and the sonic surface, albeit it is more obscured by the presence of subsonic the vortical cores.

The violet trace indicated shock wave emerging from the root area of the tie-boss, similarly to the shock wave b in Figure 57. The shock is however much weaker than in the case of oval tie-boss. Not only is the isosurface formed by more loose condition, but the surface is also much smaller.

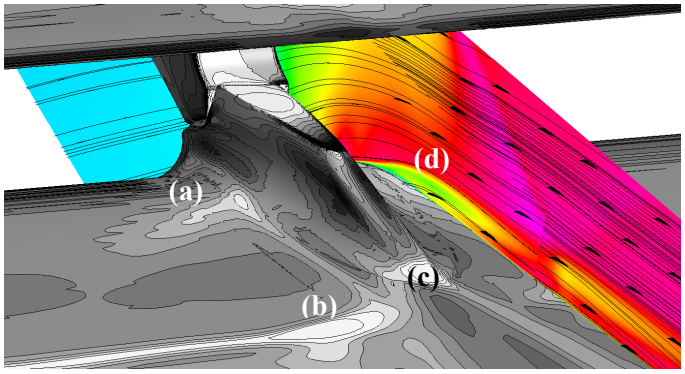

Figure 61 – Shear stress visualisation on tailored tie-boss and blade surface with velocity visualisation and streamline.

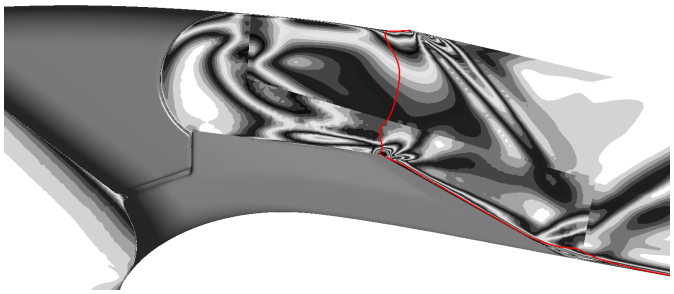

Figure 62 – Planar visualization of density gradient in tie-boss midplane with sonic red line.

In Figure 61 there is a shear stress visualization and a velocity visualization with surface streamlines. Surface streamlines are formed as streamlines of tangential components of velocity in subject plane or surface. Different colouring scheme was chosen in an attempt to visually differentiate shear stress from velocity and since no quantitative conclusions are drawn, no scale was necessary. Point (a) marks significant shear stress and velocity reduction location. The wall shear stress in the direction of flow was never negative, so an assumption is made that flow separation did not occur despite the unfavourable pressure gradient. Point (d) marks intersection of similar shear stress drop on starboard[1] side of the tie-boss with inserted axis-wise plane. The plane colour indicates velocity and there are inserted streamlines to indicate direction of the flow. In the region of reduced shear stress the flow seems to diverge from the surface of the blade. This occurs in the supersonic part of the flow field and therefore a shock wave is created. In the corner between the tie-boss and surface of the blade there is also very strong vortical flow which transports low momentum fluid further away from the surface of the blade. The point (b) marks clear trace of the inner branch of exit shock wave impingement. It is curved, as is the resulting shock wave. The positive pressure gradient of the shock wave created a rapid boundary layer growth and flow deceleration resulting in the reduced shear stress on the surface of the blade. Similar effect occurs at the point (c) where the tie-boss trailing edge shock emerges. In Figure 62 there is clear subsonic area just downstream of the shock wave near the intersection of the tie-boss body with the blade. This deceleration is expected and visible in the visualization of shear stress. There is also a compression – expansion – compression flow configuration at the upper end of the lower part of tie-boss trailing edge. This phenomenon is very local as the flow around the tie-boss is highly three dimensional. It is unclear whether this compression can be considered a shock wave. It is also clear that inner branch of the exit shock wave does not impede the adjacent blade in the area of the tie-boss shock emerging. However, the surface

[1] Designation of port side and starboard side has been adopted, as tie-boss is, in the same fashion to a ship, always oriented the same way into the flow but viewing angles of pictures and diagrams can differ and therefore a unique way of identifying sides of tie-boss was needed.

trace of the shock wave seems to indicate that the compression wave is continuous along the height of the blade. This indicates that the oblique shock was not planar and has more complicated shape.

9.5. Vortical structures – oval tie-boss

As the tie-boss body obstructs the past flowing fluid, disruptions occur in the boundary layer as well. Products of disruptions of the boundary layer are vortices. Vortical structures are going to be studied thoroughly, because possible control of their occurrence or form could lead to improvements in the blade characteristics. As expected, there are many significant vortical structures in the flow fields of both tie-boss types. Similar analysis on earlier simulations have been published by Radnic et al. [R3].

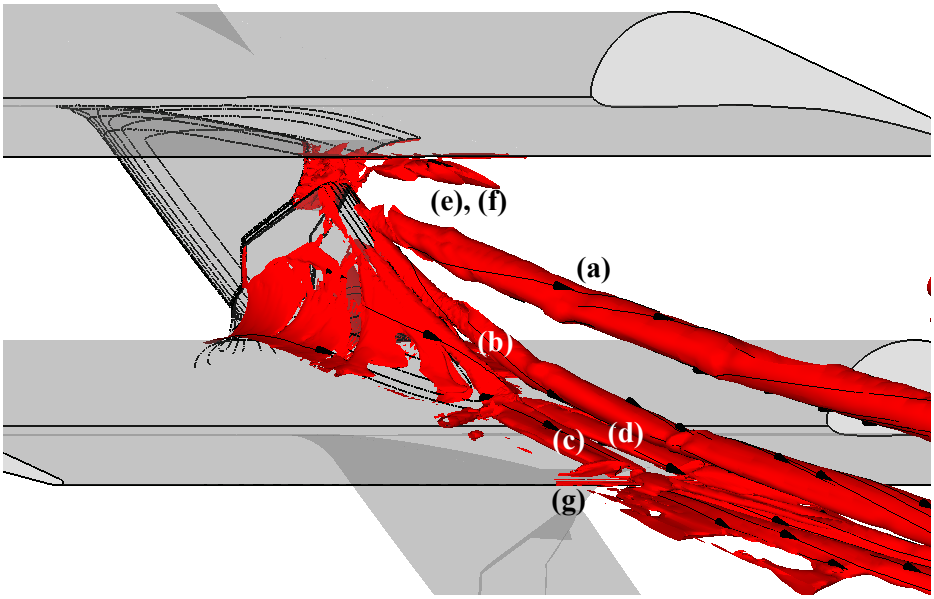

Figure 63 – λ_2 criterion isosurface with surface streamlines in the oval tie-boss interblade channel.

In Figure 63 there is visualisation of vortical cores in the interblade channel equipped with oval type tie-boss. The isosurface is equivalent to approximate value of lambda criterion $\lambda_2 \cong -55\,000\,000\ s^{-2}$. There was also λ_2 criterion sensitivity test, where the isosurfaces were created using much higher value of λ_2. Test proved that selected value did not omit any significant vortical structure. The vortical structures are quite chaotic, so the overview will be complemented by sections. In Figure 64 there is a middle part of the section a. Positions of

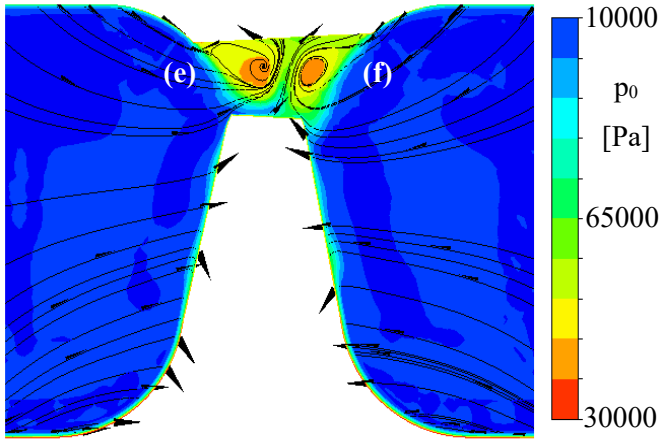

Figure 64 – Contours of total pressure and surface streamlines in the section a (see Figure 50) of the oval tie-boss.

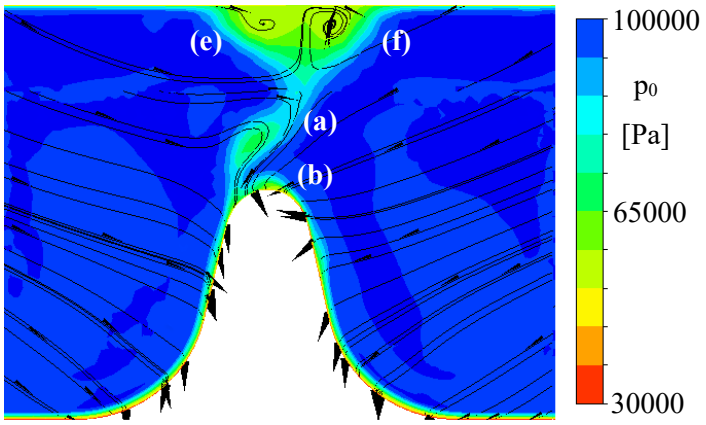

Figure 65 – Contours of total pressure and surface streamlines in the section b (see Figure 50) of the oval tie-boss.

individual sections are shown in the Figure 50. It is worth to notice that the cuts are made to be perpendicular to the flow, but the flow is not homogenous throughout the flow field. Therefore, there are streamlines which do not form closed rings around vortical cores, because the axial component of velocity is not perpendicular to the flow. This phenomenon mainly occurs in the vicinity of tie-boss trailing edge, as seen in Figure 65. In the cut a there are two very pronounced counterrotating vortices (e) and (f). These two vortices originate in the separation of the boundary layer on the trailing edge of the upper part of tie-boss. Even though this version of the tie-boss has monolithic oval trailing edge, the topmost part of its trailing edge does not reach the pressure side of the adjacent blade. Instead, the top counterpart, which itself has tailored trailing edge similar to the other type of tie-boss, creates separation bubble above the trailing edge of tie-boss itself. It is also clear that total pressure is very low in the centre of the vortices, therefore there is high loss of kinetic energy. This area of high kinetic energy loss then merges with the wake of the blade and dissolves downstream of the blade. The lower total pressure seems to be influenced by the transport of matter by the vortices. The counterrotating motion will move the slower fluid from the centre of the tie-boss wake into the boundary layer of upper blade.

In Figure 65 there is a section further downstream from Figure 64. Here, the trailing edge of the tie-boss begins to influence the flow-field. As mentioned above, the flow near the trailing edge is not perpendicular to the cut plane, so the tangential velocities in the cut plane are deforming the shape of the vortices. Vortices (e) and (f) have traversed upwards into the region of the trailing edge of the upper blade. Vortices (a) and (b) are not yet well visible, their influence, however, is. The bulging of the streamlines is a clear indicator of a presence of vortex that is not perpendicular to the cut plane, and hence vortex (a) can be identified. Vortex (b) is counterrotating bulge in the very vicinity of the tie-boss trailing edge. In this particular cut the shape of the region of lower total pressure is also interesting. It forms a diagonal pattern from the left side of the trailing edge into the right side of the wake behind the tie-boss. This diagonality is presumably an effect of the counterrotating vortices, which transport high momentum fluid into the wake. This pattern can be also seen in Figure 55.

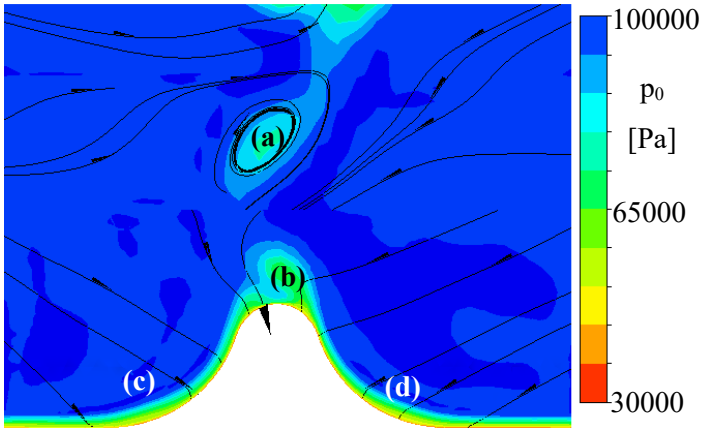

Figure 66 – Contours of total pressure and surface streamlines in the section c (see Figure 50) of the oval tie-boss.

In Figure 66 there is a cut further downstream from Figure 65. The trailing edge of the tie-boss is clearly visible. The vortices (e) and (f) have moved upwards into the area of adjacent interblade channel trough the pediodic boundary condition. Vortex (a) has separated from the trailing edge of the tie-boss and it's direction corresponds to the direction of the free flow better and therefore, its trace is clearly visible in this cut. Vortex (b) stays attached to the trailing edge. Streamlines belonging to the vortical core are curved and do not form closed circles. The vortical cores still contain areas of lower total pressure. The outer bounds of vortices have moved higher momentum fluid from free stream areas and the diagonal pattern seen in the Figure 65 has dissapeared around the vortex (a). Vortex (b) still moves fluid from the vicinity of the surface of the tie-boss into the free stream, as shown by the total pressure distribution. There is also significant growth of boundary layer in the corners of the tie-boss and slight curvature of the streamlines. The isosurfaces of λ_2 criterion show clear vortex cores formation just downstream of this particular cut. Assumption can me made that the curvature of streamlines marks formation of the vortices (c) and (d).

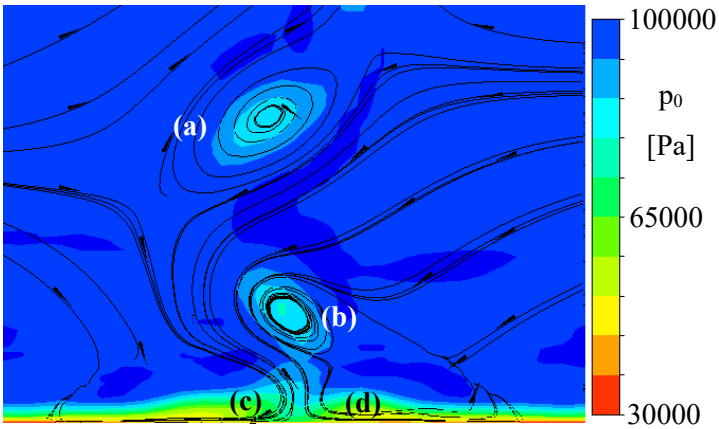

Figure 67 – Contours of total pressure and surface streamlines in the section d (see Figure 50) of the oval tie-boss.

Figure 67 shows the streamlines and total pressure distribution in the cut d. Here, the trailing edge of the tie-boss is no longer present as it's reintegrated with the blade. The vorticial core (b) is now parallel to the flow and streamlines have formed closed curves. Streamwise position of vortex (a) has not changed significantly. Vortex (b) has traversed downwards and vortices (c) and (d) have moved into the tie-boss wake. The influx of fluid into the wake area made (c) and (d) vorticial cores non perpendicular to the cut plane d and therefore their streamlines are open. It is also apparent that total pressure is paradoxically higher in the region of tie-boss wake than in the free stream around it. This behaviour is again attributed to the transport of fluid by the vortices.

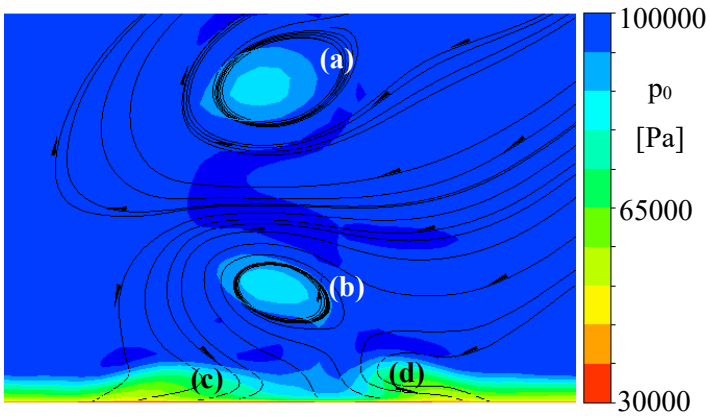

Figure 68 – Contours of total pressure and surface streamlines in the section e (see Figure 50) of the oval tie-boss.

In Figure 68 vortices (c) and (d) are traversing away from the wake of the tie-boss presumabley as the effect of shock wave induced flow turning. The cutplane e is in the vicinity of the trailing edge of the bottom blade. As in the previous cut, a region of lower total pressure is inside the wake of the tie-boss. In the vicinity of the blade surface, the two areas of lower total pressure are attributed to the transport of fluid from the boudary layer into the flow. These areas also correspond with the positions of cores (c) and (d).

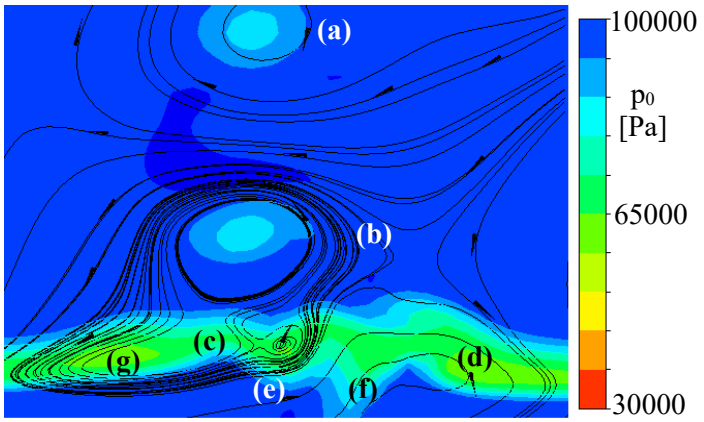

Figure 69 – Contours of total pressure and surface streamlines in the section f (see Figure 50) of the oval tie-boss.

In Figure 69 there is the last cut that was investigated in the flow field of the oval tie-boss. This cut is behind the blade cascade. The vortices (e) and (f) which have traversed upwards behind the cut in Figure 65 are now in the flowfiled again, therefore, the streamlines are very complex and trivial assesment of the vortex cores could not be risked. Hence, a distribution of λ_2 coefficient has been added. The λ_2 coefficient shows rotation and local pressure minima and therefore reliably asseses vortex cores. It is worth noting that only the negative values of λ_2 indicate vortex core, in this distribution marked by red colour. The ligther spots do not mark vortex cores. Also, the streamline configuration would suggest that vortices (b), (c), (e) and (g) have common origins, which is not the case. Lastly, number of streamlines does not conform to any physical quantity. Seedpoints of streamlines are generated on rectangular

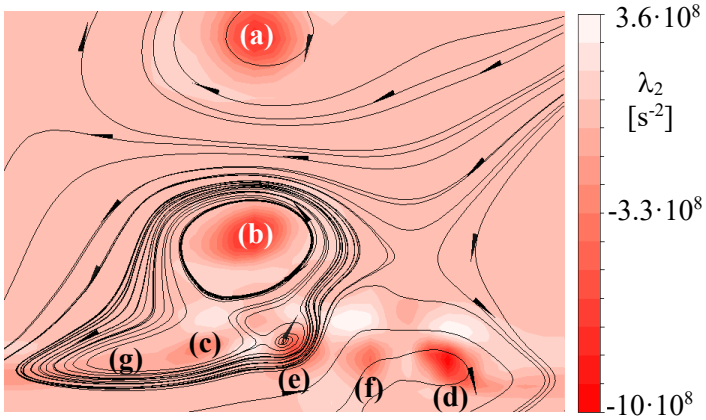

Figure 70 – Contours of λ2 criterion in the section f (see Figure 50) of the oval tie-boss.

grid and streamlines are drawn in both directions from the seed point, therefore number of streamlines in any vortex core is given by chance and does not suggest vortex strength as might seem intuitive. Caution was executed when examining the vortex configuration. Vortices (a) and (b) turned upwards in the cut plane. They are, however, straigth. Flow turning by the outer branch of exit shock wave seems to not have profound impact on the vortex core. Vortices (e) and (f) have traversed inbetween the vortices (c) and (d). The vortex pair (c) and (d) are counterrotating, vortice pair (e) and (f) are also counterrotating. However the now neighboring vortices (c) and (e) are corotating and (d) and (f) are too. As a result of this the vortices move away from each other further downsteram, as illustrated in Figure 71. This behaviour suggests that greater flow turning exhibited by the oval tie-boss might be a result of vortex interaction.

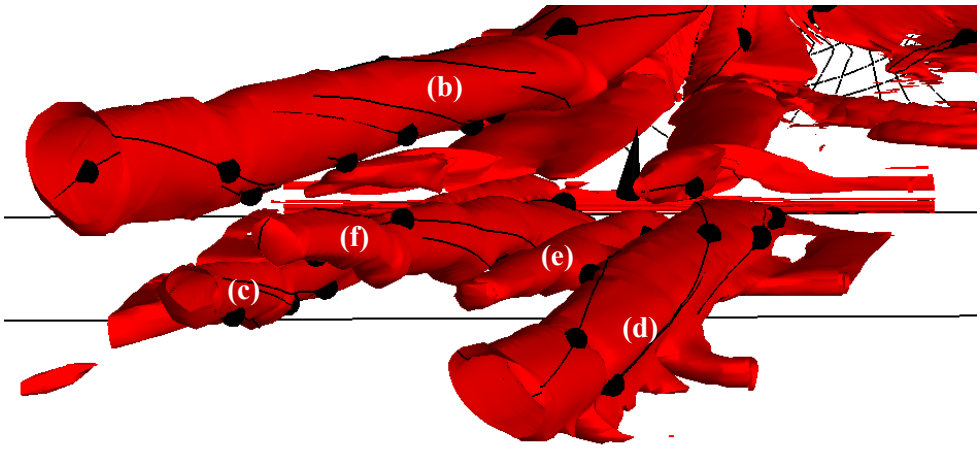

Figure 71 – Rear view of the λ_2 criterion isosurfaces.

The Figure 71 clearly shows that vortex (f) moves upwards. Vortex (e) moves also upwards and diminishes over time. Vortex (c) also moves upwards, which makes all three vortices move into the vicinity of vortex (b). This interaction is believed to have caused slight movement of the vortex (b) in the direction of blade height, in this diagram to the right. Vortex (d) on the other hand moves downwards and now is quite far away from the tie-boss wake. Influence of the vortex on the flow field was not originally attributed to the tie-boss itself. This quite complex vortex interaction cannot be studied in order to determine causality, because it is not possible to control and for example turn off one of the vortices. All the data seem to suggest is that the vortex interaction is responsible for large changes in the properties of the flow field. And therefore, understanding and control of the vortex origination and form could allow construction of part span

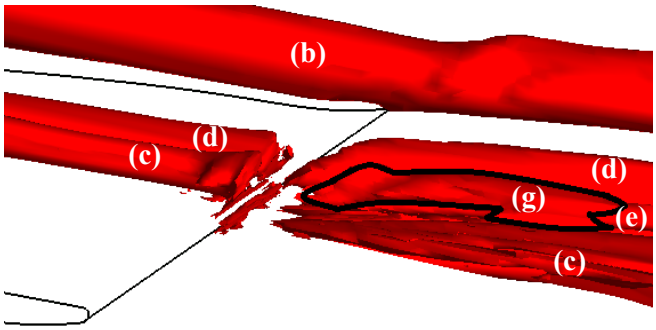

Figure 72 – Visualisation of vortex (g) in the λ_2 criterion isosurfaces.

connectors with lesser influence on the flow field. In the Figure 68 there is also vortex (g) which quickly dissipates, and which only forms downstream of the trailing edge of the blade. As apparent in Figure 72 there is a discontinuity in the λ_2 criterion. This is probably influence of the flow passing through exit shock wave of blade. This sudden compression might interfere with the local pressure

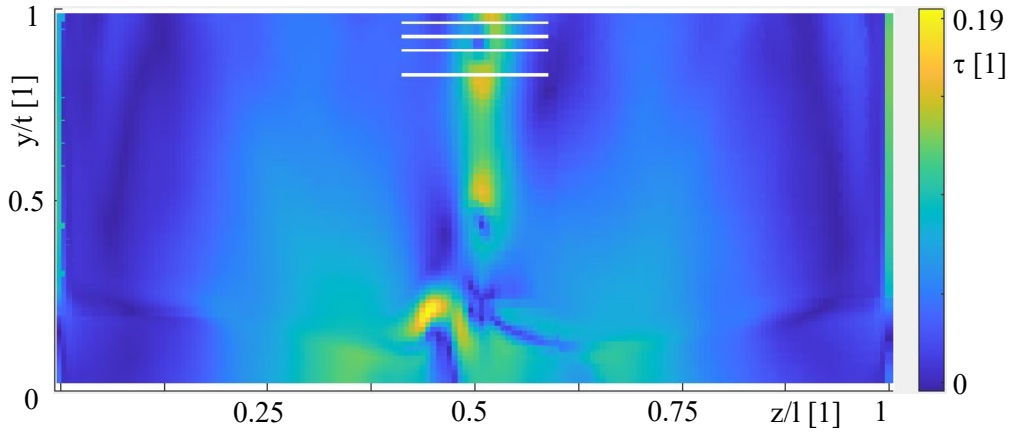

Figure 73 – Distribution of τ in the cut plane f of the oval tie-boss.

minima criterion of λ_2. Furter investigation in this matter would be needed to draw any definitive conclusions. The vortex (g) emerges just downstream of this discontinuity and therefore its origin is unclear. Most probable explanation of its existence is that it is a split from vortex (c), which was very flat after passing through the exit shock wave of the tie-boss close to its formation. Vortex (g) shares the sense of rotation with vortex (c) and vortex (c) has much more circular shape in the cut f than while it was near the blades surface. Vortex (g) dissipates very quickly as it is near two strong vortices with the same sense of rotation, and it is moves upwards and along the height of the blade.

Vortex strength distribution as defined in chapter 7.2 for the oval tie-boss interblade channel is shown in Figure 73. As stated, the vortex strength is not the best criterion for qualifying vortices. It, however, allows for a quantitative comparison with other authors. It has been now determined that no vortex breakdown occurs in the investigated interblade channel. Kalkhoran et al. [24] have found that critical value of vortex strength for possible vortex breakdown on oblique shock wave is $\tau = 0.18$ at $M = 3.5$. Coincidently this is the maximal value of vortex strength in the cut plane f, but at much lower Mach number $M_{max} = 1.7$. Investigation in other cut planes or purpose made cuts was attempted, but reliable value of tangential speed could not be obtained. Critical value of vortex strength implies that vortex control in interblade channel is desirable as a means of vortex breakdown prevention. Although the value of τ is approximately half of what would be needed for vortex breakdown to occur, vortex strength could increase in future designs. Consequences of vortex breakdown occurrence on flow field parameters are unknown, but it is certain there would be increased loss of kinetic energy and local chance of flow turning.

9.6. Vorticial structures – tailored tie-boss

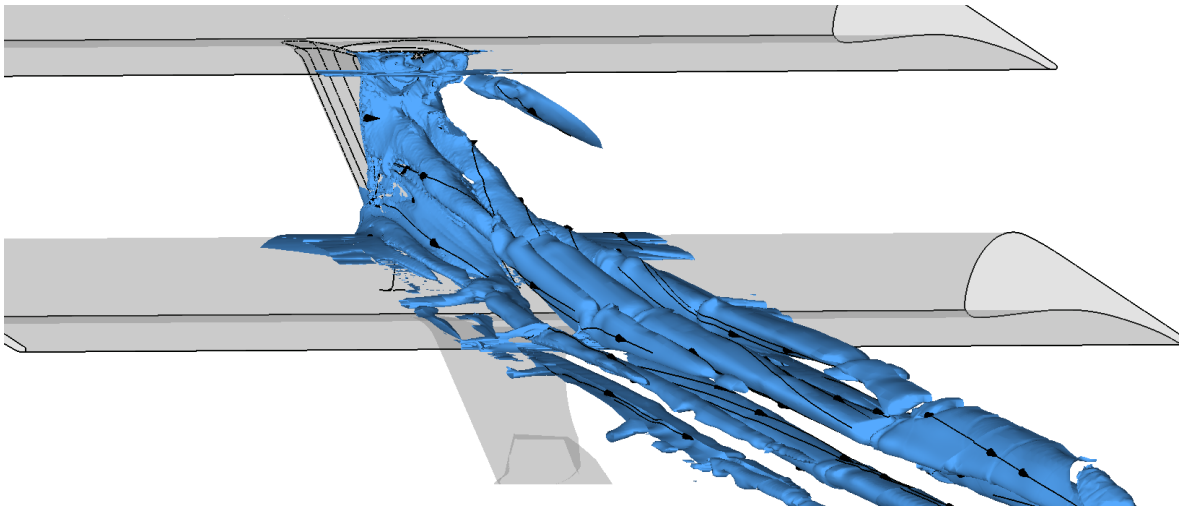

Figure 74 – λ_2 criterion isosurfaces with surface streamlines in the interblade channel with tailored tie-boss.

The vortex configuration in the interblade channel of the tie-boss with tailored trailing edge is shown in Figure 74. Chosen value of criterion was approximately $\lambda_2 = -30\ 000\ 000\ s^{-2}$. This value is lower than in the case of oval tie-boss. A dependency test was conducted and determined that higher threshold value of criterion would fail to capture significant vorticial structures. Downside of the lower value being many artifacts present in the flow field that do not point to existence of vortices. The vortex configuration is very complex and most of the vortices convene into wake of the lower part of the tie-boss making individual assessment even more difficult than in the case of the oval tie-boss. Cuts perpendicular to the flow for better vortex identification and description have been made in identical positions as in the case of the oval tie-boss.

In Figure 75 there is the first investigated cut at the position a. This cut is downstream of the tailored trailing edge of the upper part of the tie-boss and therefore many vorticial structures are already well developed. There are three vortices, (a), (b) and (c), which develop in the separation behind the tailored trailing edge, with vortex (a) in the upper part of the separation and vortices (b) and (c) in the lower part, adjacent to the surface of the lower part of the tie-boss. Vortices (d) and (e) seem to originate at the leading edge and the notch of the tie-boss, as will be shown later. There is large drop in total pressure in the tie-boss wake of the tie-boss signifying considerable loss of kinetic energy, probably due to the large separation of the flow. There is also a separation on the starboard side of the tie-boss. This separation was also visible during the surface flow visualisation in section 8.3. Once again, streamlines used for the flow visualisation in cuts are generated based on a grid of points and therefore any concentration of streamlines does not indicate any physical quantity.

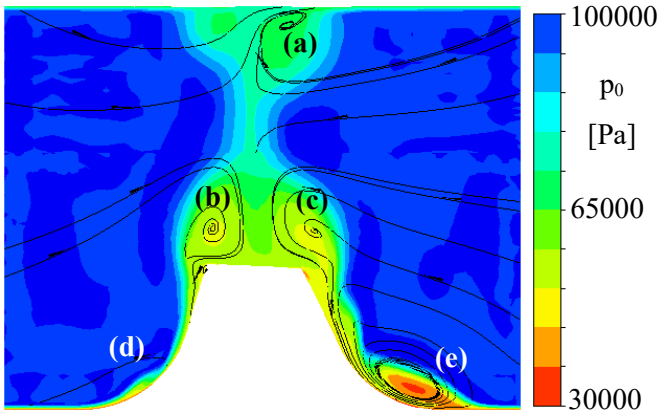

Figure 75 – Contours of total pressure and surface streamlines in the section a (see Figure 50) of the tailored tie-boss.

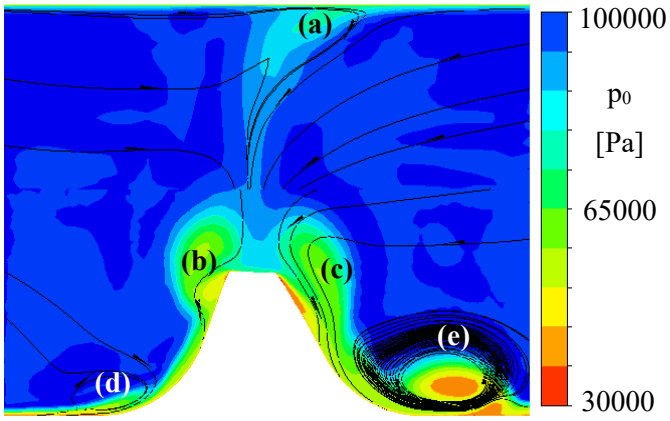

Figure 76 – Contours of total pressure and surface streamlines in the section b (see Figure 50) of the tailored tie-boss.

In Figure 76 there is distribution of total pressure in a cut further downstream. The total pressure loss in the tie-boss wake is still considerable. The same effect which quickly dissipated kinetic energy loss in the case of oval tie-boss now keeps the low momentum fluid attached to the tie-boss. Vortices adjacent to the flat top of the bottom part of the tie-boss transport the low momentum fluid down the sides of the tie-boss. Therefore, the low momentum fluid does not get dissipated into the free flow but instead sticks to the surface of the blade and tie-boss. Vortices (b) and (c) stick to the flat top of the bottom part of the tie-boss. Vortices (d) and (e) grow in size as the investigation cut moves further downstream. Vortex (a) stays adjacent to the top blade surface. Large drop of the total pressure in the vortex core (e) is a result of the flow separation.

Figure 77 shows cut even further downstream, at the position c. The trailing edge of the tie-boss has almost reintegrated with the surface of the blade by this point. The two major vortices (b) and (c) have detached from the surface of the tie-boss, but they are still moving downwards, towards the surface of the bottom blade. As before, the streamlines do not form closed loops because the vortices are not perfectly perpendicular to this cut. Vortex (e) has shifted away from the starboard side of the tie-boss along the height of the blade, but still stays attached to the surface of the blade. Vortex (d) also

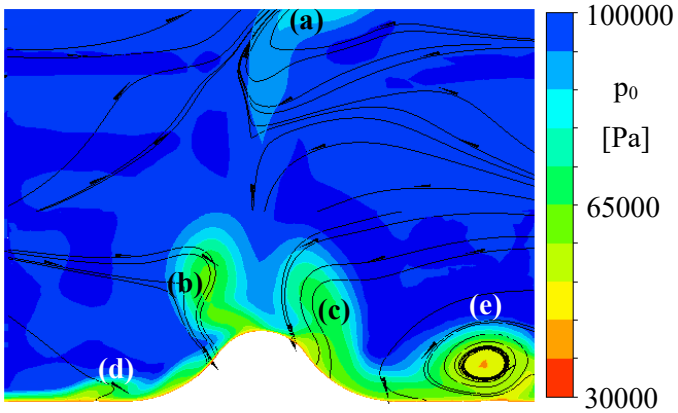

Figure 77 – Contours of total pressure and surface streamlines in the section c (see Figure 50) of the tailored tie-boss.

moves a bit away from the tie-boss and seems to have started diminishing. Total pressure distribution indicates clear drop in the area of the tie-boss wake and also very significant drop in the core of vortex (e).

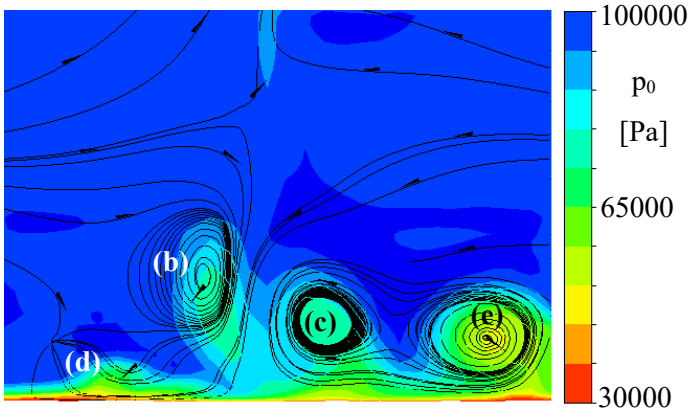

Figure 78 – Contours of total pressure and surface streamlines in the section d (see Figure 50) of the tailored tie-boss.

The cut d, see Figure 78, is the first one not to have any part of the tie-boss in it, but it still is in the region of the interblade channel, albeit now touches only the bottom blade. Vortices (b) and (c) have moved further downwards in this cut. Position of the vortex (e) has become stable across the cuts. It is clear that core of vortex (e) retains the highest drop of total pressure. All the vortices retain quite significant total pressure drop, as is expected because the vortex core should not exchange material with the surrounding flow. Vortex (d) has marginally moved inwards, closer to the wake of the tie-boss. Size of the vortex core shrinks further. The distribution of total pressure loss also marks a trend different to the oval tie-boss. The loss of total pressure is significant in an area much wider than the wake of the oval type tie-boss, where significant total pressure loss was limited to the wake and near vicinity of the surface of the tie-boss.

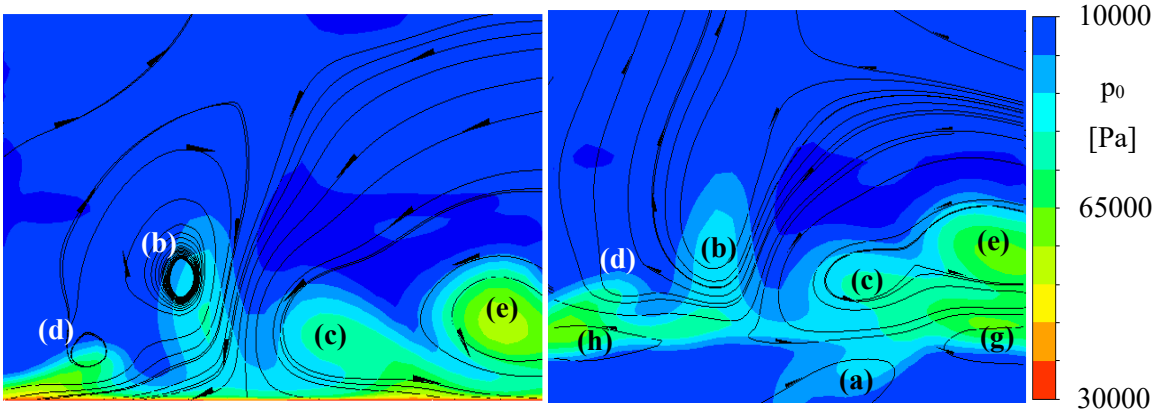

Figure 79 – Contours of total pressure and surface streamlines in the sections e (left) and f (right) of the tailored tie-boss.

In Figure 79 there are the two final cuts. The left cut, at position e, is still on top of the blade, while the cut f is behind the interblade channel. Because the configuration becomes ever more complicated, complementary distribution of λ_2 criterion has been created. The total pressure loss is still coincidental with vortex cores. The vortex core (e) harbours greatest decrease and the vortices (c) and (d) are also significant. Vortex (d) is furtherer away from the tie-boss, presumably as a result

of flow turning on the reflected inner branch of exit shock wave of the adjacent blade. Behind the trailing edge of the blade, the total pressure loss in not limited to the wake of the blade. The wake might seem to be too high in the right cut, but this is a result of the cut being taller itself, the absolute positions are therefore not to be compared.

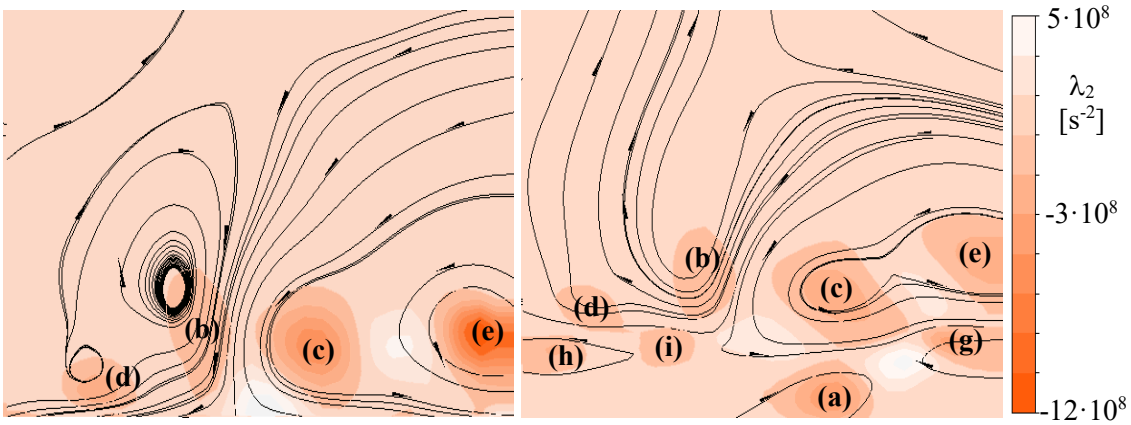

Figure 80 – Contours of λ_2 criterion and surface streamlines in the sections e (left) and f (right) of the tailored tie-boss.

In Figure 80 there is the distribution of λ_2 criterion in the same cuts as in Figure 79. There is a noticeable difference between the vortical cores indicated by the λ_2 criterion and what would seem to be vortical cores according to the streamlines. This disarray, especially in case of the vortex (b) in left cut, is attributed to the randomness of the streamline placement and different magnitude of rotational forces, which might be greater in the vicinity of other vortices. From the cut section f, there are 8 identifiable vortical cores, 7 of which are investigated further because the origin of vortex (i) could not be investigated due to the complexity of flow field int the wake of the blade. Vortices (b), (c), (d) and (e) are in virtually identical positions in both cuts. Vortex (a), which was generated in the next interblade channel has traversed into the wake of the blade. The vortex (g) seems to have originated in the wake of the blade and possibly as a result of the presence of corotating vortices (c) and (e), to which there is counterrotating vortex (a). This configuration is believed to have led to creation of shear stress in not too stable blade wake. Very similar mechanism is believed to have led to creation of vortex (h), but the responsible vortices would be (a) and (d). The origin of vortices (d) and (e) had to be investigated more thoroughly. λ_2 criterion in the region of leading edge of the tie-boss did not form any significant structures apart from a small bulge in the notch in the leading edge.

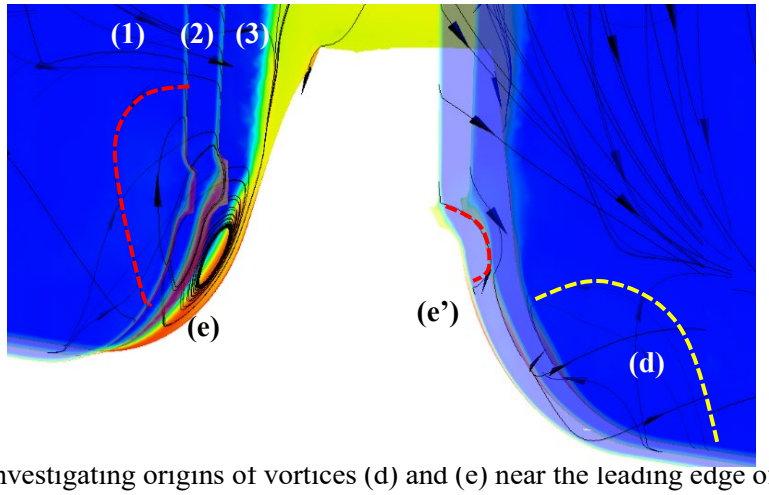

Figure 81 – Cuts investigating origins of vortices (d) and (e) near the leading edge of the tie-boss. The overview of the cascade is in Figure 80.

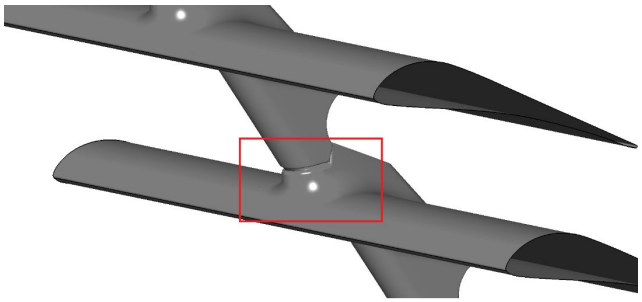

Figure 82 – Overview of the cascade with marked view of Figure 80.

Therefore, a different approach was chosen. A set cut planes was created in the region of leading edge of the tie-boss. Colour of the cut planes is distribution of total pressure, and the scale is identical to the previous cuts. It is not significant for this analysis, therefore there is no legend. The Figure 81 is a composition of three separate cut planes. The two cut planes in front have been made transparent, while the third one is opaque. The planes are numbered (1), (2) and (3) respectively, the plane (1) us the most upstream, while (3) is the most downstream. There is a closed loop of streamlines in the Figure 81 marked by the red dashed curve located in the cut (1). This loop is present on both starboard side and port side of the tie-boss. This is the vortex that originated in the notch and leads around the leading edge. It is assumed that this vortex formed by the same mechanism as horseshoe vortex, but its position was determined by the presence of the notch. It is clear that this vortex on the starboard side of the tie-boss moves towards surface of the bottom blade in the cut plane (2). In cut plane (3) there is very pronounced vortical core which later propagates to the massive flow separation. On the starboard side, the significant drop in total pressure can be seen as early upstream as in the cut plane (3). On port side, however, it does not seem that the vortex named (e'), the counterpart of the vortex (e), would directly transform into the vortex (d). Vortex (d) has been marked by the yellow dashed curve in the cut plane (3), while vortex (e') remains further away from the surface of the bottom blade and seems to dissipate. Vortex (d), which is much smaller than the vortex (e), seems to be ordinary corner vortex. An observation can be made that the vortices (e') and (d) are counterrotating, therefore a possibility that shear stress induced into the flow by vortex (e') has an

influence on formation of vortex (d) cannot be ruled out. It is presumed that the fillet which has much larger diameter than the thickness of the boundary layer prevented formation of a significant corner vortex. Evolution of vortex (e) suggests that the notch on leading edge of the tie-boss plays large role in the size and position of some vortices in the flow field. Therefore, size and positioning optimisation of the notch could lead to improvements in overall cascade flow parameters. The notch almost disappears on the port side of the tie-boss and with it the vortex (e'), which further corroborates on the need of optimisation of this particular geometrical element. The notch in the case of the oval tie-boss is shaped marginally differently and no significant vortex seems to originate from it. There is a question of accuracy of the modelling of the notches and meshes inside them, but sensitivity investigation is outside the realm of practical possibilities in the scope of this work.

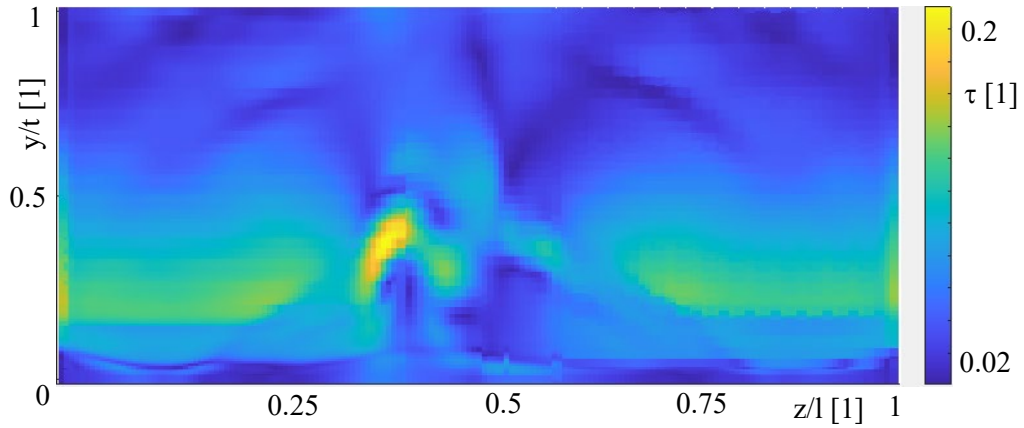

Figure 83 – Distribution of vortex strength in the cut plane f of the tailored tie-boss.

In Figure 83 there is a distribution of vortex strength τ in the tailored tie-boss interblade channel. Value of vortex strength is highest in the vicinity of the vortex (b). Vortices (d), (c) and (e) also generate quite high values of τ, but dependability of the method is once again called in question, because seemingly high values of vortex strength can be seen in the free stream area with turning of the flow on the outer branch of exit shock wave. The maximal value of vortex strength was $\tau = 0.22$. Hence, no vortex breakdown was expected, because critical vortex strength would be approximately $\tau_{crit} = 0.4$. Considering limited accuracy of obtaining the input parameters for calculation of τ this value could be higher and vortex control is still considered desirable[2].

[2] Author's remark: a vortex breakdown simulation sensitivity would be in order, where known vortex breakdown scenario is modelled to determine whether the numeric solver is able to capture such phenomenon. There is no known theoretical limitation on the side of the solver regarding modelling of vortex breakdown, yet this testing will be done in future.

10.Reduced parameters

The method of data reduction has been introduced in the chapter 7.5. The main quantities that are of interest to evaluate the performance of the blade cascade are kinetic energy loss coefficient as defined by equation 6.2 and cascade exit pitch angle β, which is defined in chapter 4.1. The data obtained from the experimental investigation have been also shown in the distributions alongside the results of numeric simulation. Reduced parameters are always evaluated in a plane that is positioned identically to traversing plane in the experiments.

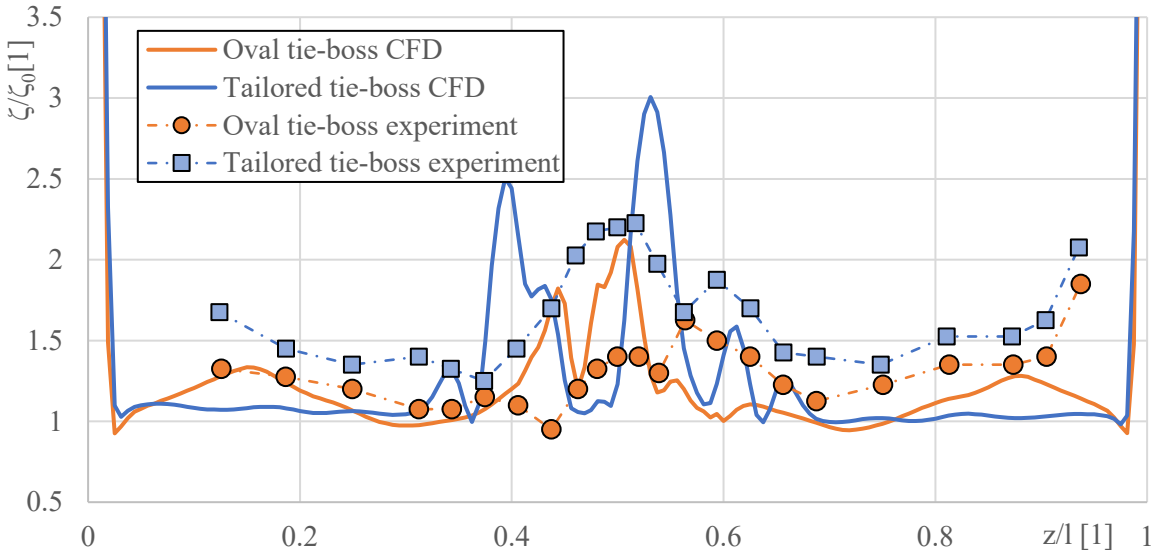

Figure 84 – Span-wise distribution of relative kinetic energy loss coefficient.

In Figure 84 there is the distribution of relative ζ/ζ_0. Note that different values of ζ_0 have been chosen. For the experimental data the ζ_0 is equal to the measured value on the reference cascade while the ζ_0 chosen for numerical data comes from the numerical simulations. The agreement with experiment is quite good but as mentioned earlier the tested cascade and tie-boss did not have the contact notch modelled. This increases possible differences between the experiment and the numerical simulation. The distribution clearly shows that the losses of kinetic energy are much higher in case of the tailored tie-boss than for the oval one. The losses are overall higher in most areas along the blade with the small exception of the area directly in the wake of the tie-boss. This is to be expected given the total pressure distribution shown in the investigated cuts. The vortices (b), (c) and (e) of the tailored tie-boss have transported fluid with higher loss of kinetic energy further away from the tie-boss. Although it has been found out that the vortex e has its shape dictated by the presence of the notch which was not present in the test cascade, the ζ is also higher in the wider area. Although, there has not been a clear drop in the loss coefficient in the wake of the tie-boss. Unfortunately, it is not possible to assess the vorticial structures in the tested cascade given the available measured data and methods available for their acquisition. The distribution of ζ/ζ_0 on the oval tie-boss has very different trends. There is no massive separation behind the trailing edge of the oval tie-boss. There is

a limited one on the top of the trailing edge, but its influence is lesser than the tailored trailing edge separation. The major vortices of the oval tie-boss also do not move away from the wake of the tie-boss and do not transport significant amount of low momentum fluid away from the wake, which leaves the loss coefficient confound to the area of the wake. Lastly there was a possibility of evaluation of 3D data reduction method which would yield a singular value of kinetic energy loss coefficient. This approach was not pursued because it would create a result which would have no physical meaning, but it would seem like one. The evaluation is dependent on the width of the channel with constant width of the tie-boss. Therefore, it would be dependent on that ratio and not comparable to any other evaluation than prismatic blade in a 160 mm wide channel.

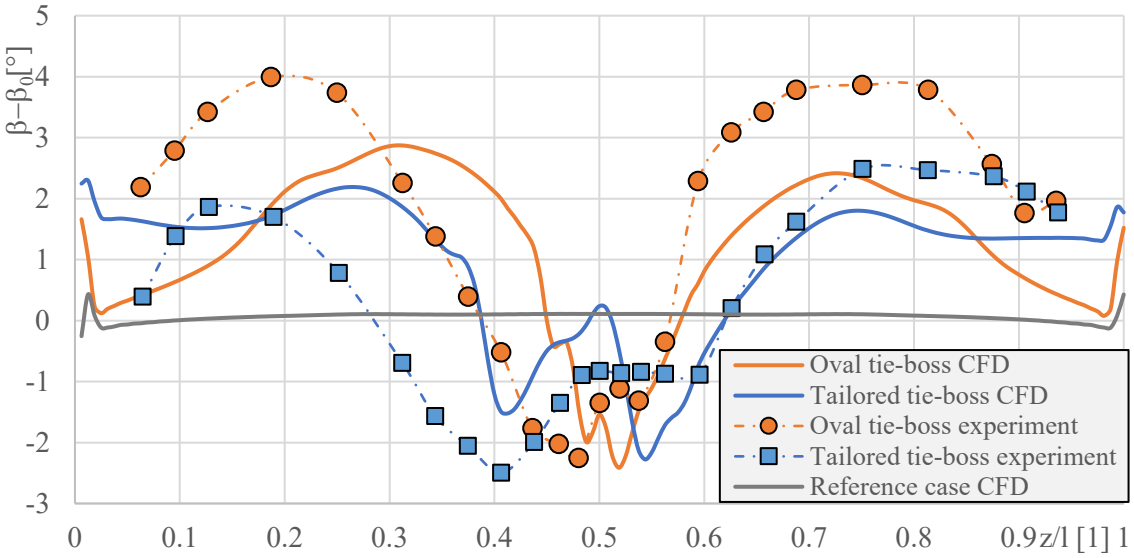

Figure 85 – Span-wise distribution of exit flow angle.

In Figure 85 there is the blade-wise distribution of relative exit flow angle β/β_0. Again, the values of β_0 have been chosen individually for corresponding data set. It is apparent that the numerical simulation results resemble the trends of the experimental data, however the absolute value of β seems to be marginally shifted. The influence of the tailored tie-boss is again wider than the influence of the oval tie-boss. There is increased value of the exit angle in the region outside the oval tie-boss wake. It is debatable whether this is the influence of the vortex. The data reduction method obtains parameters through strict balancing of mass flow and momentum. The vortices do transport matter in a circular manner so their net influence, dependent on the direction of investigated cut, could be positive or negative given on position relative to vortex core. Moreover, vortices are usually accompanied by a counter rotating vortex which should, in theory, enhance this effect. The data reduction method has been applied in vertical cuts, so vortices, which were above one another should have net zero effect on flow turning. On the other hand, in the case of tailored tie-boss, the vortices are fanning out along the height of the blade and this effect should be more profound. There are local extremes in the tie-boss wake for the oval type and just outside the wake for the tailored tie-boss. This

coincides with the location of major vortices in the respective cases. It is not possible to determine whether the flow turning can be attributed to the vortices, but the data seems to suggest it. This is yet another reason why measures of control of the vortices should be considered.

For better understanding of the development of the exit flow angle, the data reduction method has been applied to the cuts used for investigation of vortices. Then, the obtained flow angle has been normalized by value that was in the free flow in the immediate vicinity of the side wall for each individual cut plane of the tailored tie-boss. This means that the distributions are comparable on an absolute scale. The distribution of the tailored tie-boss interblade channel is in Figure 86 and of the oval tie-boss is in Figure 87.

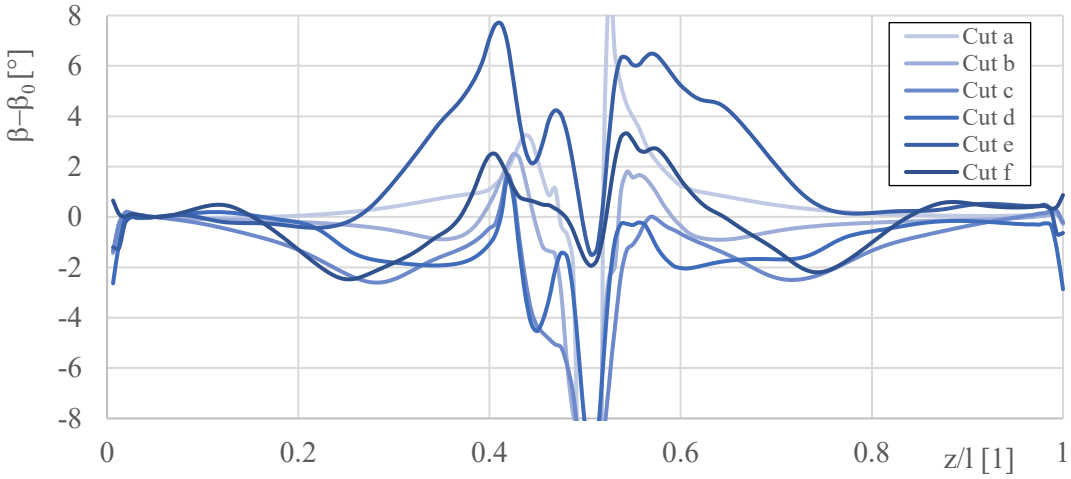

Figure 86 – Distribution of relative reduced flow angle in cuts defined in Figure 50 in the tailored tie-boss interblade channel.

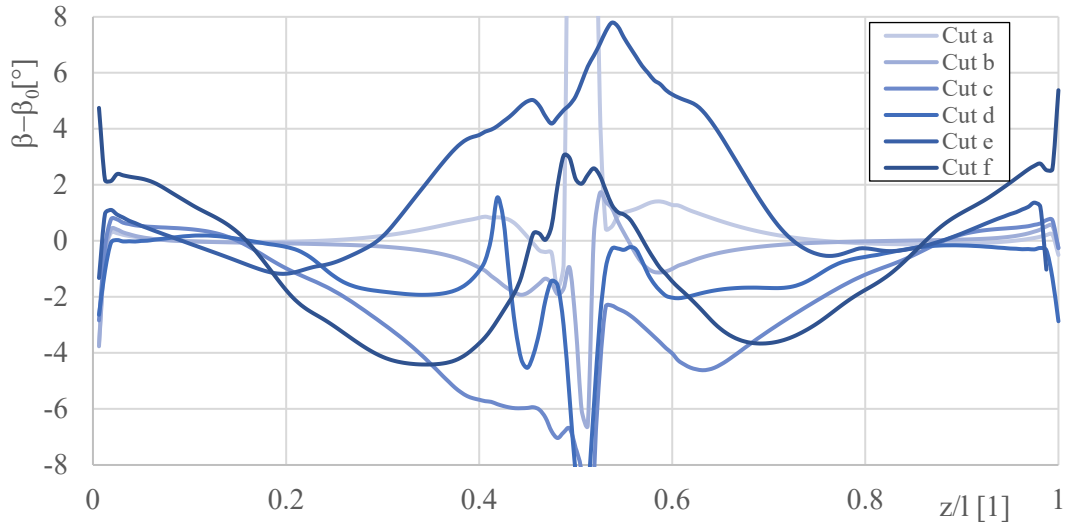

Figure 87 – Distribution of relative reduced flow angle in cuts defined in Figure 50 in the oval tie-boss interblade channel.

The distributions show that the flow angle changes gradually during the flow past the tie-boss. This proves that the change cannot be attributed to the passage through a deformed shock wave, which was one of the working theories. The change in the angle seems to be caused by the expansion in the partly obstructed interblade channel. The tie-boss deflects fluid into the free stream part of the channel. An argument can be made that the tie-boss influences the properties of past flowing fluid in a manner similar to that of a profile in a free stream. Distribution of Mach number in an examination plane which passes the middle of interblade channel is shown in Figure 88.

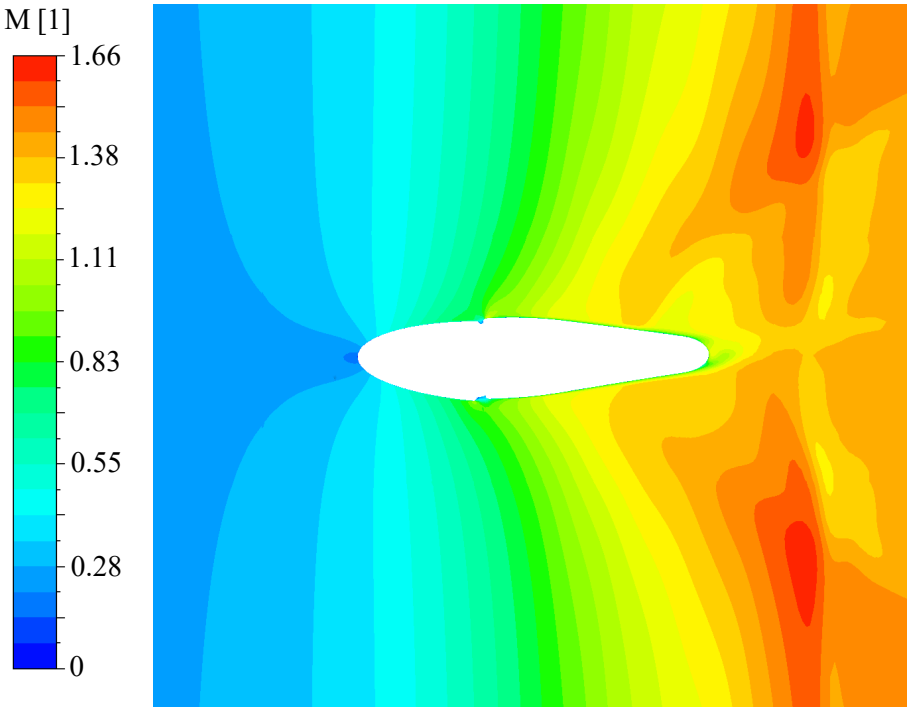

Figure 88 – Mach number distribution in a cut plane inside the interblade channel of the oval tie-boss.

The Mach number distribution shows that the flow past the tie-boss body does not resemble a flow past a single profile. The distribution of velocity is mainly dictated by the presence of the interblade channel. Curiously, the tie-boss profile forces faster expansion of the flow and the corresponding increase of the Mach number, but the deceleration of the flow which would have been seen on the single profile is not present.

11.Conclusions

Presence of the part span connector is inevitable in modern steam turbine; therefore, an effort is to be made to control its influence on the flow field. The geometry of investigated connectors was dictated mainly by the structural purpose they serve.

In an attempt to gain insight into complex three-dimensional flow in the transonic blade cascade equipped with part span connector tie-boss, a thorough theoretical background was laid. The main focus of the theoretical background was flow of supersonic fluid past deflective walls, inside channels of varying geometry and past profiles. In these examples, behaviour of the fluid has been described, including formation of shock waves or expansion fans. Interaction of shock waves with other shock waves and wakes was described. Flow past trailing edges of various thicknesses was studied with emphasis on formation and shape of exit shock waves.

In depth flow field analysis has been performed using numerical simulations. A computational mesh consisting of 6.8 mil elements and non-homogenous interfaces has been constructed. Mesh sensitivity analysis has been done on a reference case for two commercial solvers, Ansys CFX and Ansys Fluent. The results have been coherent on both the solvers, Ansys CFX was ultimately chosen for better non-homogenous interface handling. Results of the numerical simulations showed good agreement with results of preceding experiments Trends of exit flow angle and kinetic energy loss coefficient are identical.

The analysis showed that several major and few minor vortices have formed in the interblade channels of both oval and tailored tie-boss. The analysis using cut planes suggest that vortices play a significant role in transport of the fluid between the wakes, boundary layers and free flow around the profiles, thus having a profound effect on the span-wise kinetic energy loss coefficient. It was also shown that vortex cores will traverse through the flow field correspondingly to geometry and direction of the flow and they seem to be affected by the transportive effects of other vortices.

Interactions of shock waves and vortices have been observed. Vortex cores seem to have been deflected accordingly by the passing shock waves, the cores themselves were deformed. While no vortex breakdown has been observed, the evaluation of vortex strength showed that vortices present in the flow could possibly break down in the right conditions. The vortex strength τ_{max} was approximately 0.22 for tailored tie-boss and 0.2 for oval tie-boss. For respective Mach numbers the critical value of vortex strength would be approximately 0.33. This is yet another reason why control of the induced vortices is sensible, as vortex breakdown would dramatically disturb the flow.

The presence of the tie-boss has also been shown to influence the angle of exit shock wave downstream and induction of new shock waves to the flow. The inner branch of exit shock wave and its reflected counterpart have been influenced the most, but outer branch of the exit shock wave is

visibly deformed too. New shock waves, seemingly originating at the downstream maximal thickness position of the tie-boss at the intersection with suction side of the profile. Second set of new shock waves seems to originate at the intersection of the tie-boss trailing edge and suction side of the blade.

The tie-boss was found to have caused a sharp increase in kinetic energy loss coefficient. Locally, the value of coefficient was up to 300% of the reference blade for tailored tie-boss and up to 215% for the oval tie-boss. These values are however local maxima, overall influence is much lower. The tailored tie-boss trailing edge has caused massive flow separations and thus massive wake which is believed to be the driving force of the kinetic energy losses. The straight and curved trailing edge of the oval tie-boss limits the disruptions of the flow and causes lower losses.

The tie-boss was also found to have caused changes in exit angle not only in the wake of its body but also in the region of free flow by as much as 2.85° for the oval tie-boss and 2.18° for tailored tie-boss. This change has been found to be gradual rather than abrupt, caused for example by a deformed shock wave. The cascade exit angle affects the blade performance. It is debatable whether the streamwise position of the tie-bosses could alleviate the effect, as moving them upstream would provide more space for expansion in the interblade channel as well as lower velocities in the region of its presence. This approach was tested by other authors, yet the testing was rather broad and unspecific for last stage of steam turbine of large power output. It is authors belief that testing of different possible positions of PSC could improve the stages performance. However, the PSC must fulfil its structural role and possibility of position change must be evaluated regarding their function first.

Lastly, there is a question regarding the stability of the numerical solution. A time-resolved simulation would greatly increase the possibility of understanding development of all the flow field phenomena. Sadly, a sheer demandingness of such task was entirely out of scope of this thesis. It is also believed that implementation of the recommended changes would greatly reduce the major flow phenomena which would need to be simulated by a time-resolved model.

11.1. Evaluation of aims of the work completion

I. A set of methods allowing detection, description and categorization of complex flow field has been devised.

   a. The developed experimental setup has been described and the model for the measurement has been designed and manufactured. Pneumatic measurements in combination with surface flow visualisations provide insight into the complex flow field phenomena.

b. Expected flow field phenomena have been examined in the theoretical analysis which forms basis for the flow field examination. Special care was given to interaction of shock waves and vortices which form in the transonic flow filed of the mid-section interblade channel. Complex, three-dimensional flow field contains interactions of shock waves that propagate diagonally through the flow and interactions with wakes and vortices.

II. A computational mesh was build using the Ansys ICEM software. The mesh consists of three non-homogenous zones with one tetrahedral able to wrap around the complicated geometry of the tie-bosses while hexahedral regions were used to fill prismatic part of the computational domain. The hexahedral regions of the mesh have been generated using the blocking technique, which enabled total control of the mesh layout. The shifted periodic approach was chosen for 1:1 periodic boundary. The tetra and pentahedral region have been meshed using the octree flooding technique with post flooding boundary refinement. The regions were separated with non-homogenous mesh interfaces. Mesh sensitivity analysis was performed in both proposed solvers has been performed. The meshing approach ensured the ability to manipulate the refinement of the mesh while maintaining the general layout. The mesh sensitivity analysis showed that the finest considered mesh is to be used to capture all the possible flow phenomena accurately. The numerical simulation has been conducted using Ansys CFX software, although Ansys Fluent has been considered and tested too. Validity of numerical data in critical regions has been tested.

III. Re-examination of experimental results brought forward sporadic misconceptions of past publications. Insight has been gained into the nature of shock – boundary interactions. Surface stream visualisation has been complemented by examining the videos captured during the measurements, uncovering post measurement accumulation of visualisation mixture.

IV. Very detailed analysis of the results has been done.

a. Three dimensional visualisations of shock wave configuration and vorticial configuration have been provided for both types of the tie-boss. Mutual interactions of the flow field phenomena have been studied and complex description of the flow through the interblade channel has been obtained.

b. Reduced flow field parameters have been obtained and influence of the tie-boss presence on the flow field was studied. Distribution of kinetic energy loss coefficient and exit flow angle have been obtained and their implications discussed.

c. The very fine computational mesh used allowed in depth analysis of certain flow field phenomena and allowed drawing conclusions regarding their origins. Massive vorticial structures have been linked to notches in the geometry of the connector. Location of origination of certain shock waves had been uncovered. Interaction on wake and vortices and shock waves have been found and described.

11.2. Future work

Designing of the new steam turbines is not expected to cease in the near future and the part span connectors will be part of the new designs. Therefore, it is authors firm belief that the basis for future research laid by this thesis should be expanded.

The thesis showed that there is a room for optimisation of the shape of the part span connectors and has identified critical geometries which are responsible for some of the influence on the flow field. In the first wave, simulations on the existing shapes of tie-boss with some alterations should be performed. A simulation on tie-boss with closed notch should prove the influence on formation of vortices, simulation on tie-boss with narrower and smoothed out trailing edge should prove its influence on the shock wave configuration. Then, either through alternation of flow conditions or position of the tie-boss, a variant with the tie-boss body in the subsonic region of the flow should be investigated.

Further numerical testing of part span connectors designed with respect to the findings of the subsequent simulations would be in order. New possible shapes of the part span connectors should be devised in cooperation with structural engineers. Special attention is to be paid to the trailing edge of the connector, as it is a less dramatic change. The thinner trailing edge and expected smaller wake should lead to overall lower losses, lower changes in exit flow angle and therefore overall smaller impact on the blade performance. Another model should consider optimised shape of connector notch. While it is common understanding that rounded shapes defuse stress peaks and therefore are not entirely avoidable, an optimised shape moving the notch to a location of lower influence could be derived. Lastly, a change of position of the connector should be considered. Should the trailing edge of the connector end before supersonic transition of the flow, its influence on the shock wave configuration is expected to decrease.

Should any of the newly devised shapes show promising performance, an experimental testing is in order. Manufacturing technology has undergone a significant development since the building of the last model, and so did the ability to measure ever smaller or more intermittent phenomena. Therefore, a more accurate testing more narrowly aimed at the expected phenomena should provide new results that would form design on future last stage mounter part span connectors.

12. List of abbreviations and indices

Table 5 – List of used quantities.

Designation	Quantity	Unit
A	Area	m^2
c	Chord length	m
h	Specific enthalpy	$J\ kg^{-1}$
p	Pressure	Pa
s	Specific entropy	$J\ kg^{-1}K^{-1}$
T	Temperature	K
l	Width of the test section	m
M	Mach number	1
M^*	Dimensionless velocity	1
Q	Q-criterion	s^{-2}
t	Pitch	m
x	Chord-wise coordinate	m
y	Pitch-wise coordinate	m
y^+	Dimensionless wall distance	1
w	Velocity	$m\ s^{-1}$
z	Span-wise coordinate	m
α	Nominal angle	°
α_{pt}	Angle of inclination of adjustable perforated tailboard relative to the plane of trailing edges	°
β	Flow angle	°
γ	Stagger angle	°
Γ	Circulation	m^2s^{-1}
δ	Deviation of the flow	°
κ	Isentropic expansion factor	1
ι	Angle of incidence	°
∇	Nabla operator	According to derived quantity
λ_2	Lambda 2 criterion	s^{-2}
τ	Vortex strength	1
τ_{sh}	Shear stress	Pa
θ	Deflection angle	°
ζ	Kinetic energy loss coefficient	1
ω	Vorticity	s^{-1}

Table 6 – Table of used indices

subscript	description
01	Total, upstream
1	Upstream, inlet
02	Total, downstream
2	Downstream, exit
b	Barometric
2S, 3S, 4S, 5S, 6S	Static, measured by tappings on the side wall of the test section in front of the cascade
015, 25, 35, 45, 55	Measured by individual taps on the conical probe
is	Isentropic

$_{s}$	Static
$_{tot}$	Total
$_{x, y, z}$	Coordinate wise.
Superscript	
^{SC}	Settling chamber

13.References

13.1. Author's references

[R1] Aerodynamic Effects of Tie-Boss in Extremely Long Turbine Blades. Radnic, Tomáš, et al. November 2018, ASME. J. Eng. Gas Turbines Power. ISSN 0742-4795.

[R2] T. Radnic, M. Luxa and D. Šimurda, "Shock Wave Configuration in a Transonic Flow Through a Mid-Section of Last Stage Turbine Blade Cascade Equipped With a Part Span Connector, " Acta Polytechnica CTU Proceedings, submission in progress.

[R3] Numerical Investigation of 3-D Flow Phenomena in Interblade Channel with Tie-boss. Radnic, Tomáš, et al. 2021. Proceedings of 14th European Conference on Turbomachinery Fluid dynamics & Thermodynamics. ISSN: 2410-4833.

13.2. Other references

[1] Global Emissions. [Online] Center for Climate and Energy Solutions. [Cited: 18 july 2022.] https://www.c2es.org/content/international-emissions/.

[2] 3-D inviscid self-excited vibrations of a blade. Rządkowski, R. and Gnesin, V. 2007, Journal of Fluids and Structures 23, pp. 858-873. ISSN: 1095-8622.

[3] Static and Dynamic Analysis of 1 220mm Steel Last Stage Blade. Míšek, Tomáš and Kubín, Zdeněk. s.l. : University of West Bohemia, 2009, Applied and ComputationalMechanics 3, pp. 133-140. ISSN: 2336-1182.

[4] Complex Three-Dimensional Turbulent Flows. Bradshaw, P. s.l. : University of Newcastle, 1983. Eighth Australian Fluid Mechanics Conference. pp. K5.1-K5.6. ISBN: 9780725904630.

[5] Aerodynamic Performance Assessment of Part-Span Connector of Last Stage Bucket of Low Pressure Steam Turbine. Mistry, Hiteshkumar, et al. 2011. ASME 2011 Power Conference collocated with JSME ICOPE. ISBN: 978-0-7918-4459-5.

[6] A Numerical Investigation of the Impact of Part-Span Connectors on the Flow Field in a Linear Cascade. Brüggemann, C., et al. Charlotte, NC, USA : s.n., 2017. Proceedings of ASME Turbo Expo 2017. ISBN: 978-0-7918-5078-7.

[7] Numerical Investigations on the Aerodynamic Performance of Last Stage Bucket With Part-Span Connector. Li, B. and Li, J. Montreal, Quebec, Canada : s.n., 2014. Proceedings of the ASME 2014 International Mechanical Engineering Congress and Exposition. Volume 7: Fluids Engineering Systems and Technologies. ISBN: 978-0-7918-4954-5.

[8] Numerical Investigation of the Impact of Part-Span Connectors on Aero-Thermodynamics in a Low Pressure Industrial Steam Turbine. Häfele, Markus, et al. Düsseldorf, Germany : s.n., 2014. Proceedings of ASME Turbo Expo 2014: Turbine Technical Conference and Exposition. ISBN: 978-0-7918-4558-5.

[9] Numerical and Experimental Study on Aerodynamic Optimization of Part-Span Connectors in the Last Stage of a Low-Pressure Industrial Steam Turbine. Häfele, Markus, et al. s.l. : Sage, 2015, pp. 456-476. ISSN: 0957-6509.

[10] Experimental Study on the Aerodynamic Characteristics of Blades at the Last Stage of a Steam Turbine at Off-Design Conditions. Yungfeng, Liu, et al. 2022, International Journal of Aerospace Engineering. ISSN:1687-5966.
[11] High-speed Aerodynamic Investigation of the Midsection of a 48" Rotor Blade for the Last Stage of Steam Turbine. Luxa, Martin, et al. Lappeenranta, Finland : s.n., 2013. Proceedings of 10th European Conference on Turbomachinery Fluid dynamics & Thermodynamics. ISSN: 2410-4833.
[12] A Selection of Graphs for Use in Calculations of Compressible Airflow. Rosenhead, Louis and et al. Oxford : Cambridge University Press, November 1954, Journal of the Royal Aeronautical Society, p. pp. 789. ISSN: 0001-9240.
[13] Uruba, Václav, Jonáš, Pavel and Antoš, Pavel. Measurements of Turbulence in Transonic Wind Tunel of Institue of Thermomechanics (in Czech). Praha : s.n., 2012.
[14] Aerodynamic Tests of a Transonic Turbine Blade Cascade Model Consisting of Low Number of Blades. Šimurda, David, et al. Pilsen : s.n., 2012. Turbomachines (In Czech). pp. 1-10.
[15] Kožíšek, Martin, Luxa, Martin and Šimurda, David. Calibration of Five-Hole Conical Probe for Traversing Device II, Research Report Z 1507/14 (in Czech). Praha : s.n., 2014.
[16] Bryer, Denis William. and Pankhurst, R. C. Pressure-Probe Methods for Determining Wind Speed and Flow Direction. London : Her Majesty's Stationery Office, 1971. ISBN: 011480012X.
[17] Dvořák, Rudolf. Internal Aerodynamics (in Czech). 1975.
[18] Babinsky, Holger and Harvey, John K. Shock Wave-Boundary-Layer Interactions. s.l. : Cambridge University Press, 2011. ISBN: 9781107646537.
[19] Anderson, John D. Fundamentals of Aerodynamics. s.l. : University of Maryland, 2001. ISBN: 1259129918.
[20] Šafařík, Pavel. Regarding the problems of steam turbines (In Czech). Prague : ČTVS, 1976.
[21] Luxa, Martin. Effects of the Design Solutions of the Blade Wheel with very Long Blades of the Last Stage of the Low Pressure Cylinder of the Steam Turbine of Large Output on Transonic Flow Field (in Czech). Praha : s.n., 2017.
[22] Cattafesta, Louis N. and Settles, Gary S. Experiments on Shock/Vortex Interactions. 30th Aerospace Sciences Meeting and Exhibit. 1992.
[23] On Identification of a Vortex. Jeong, Jinhee and Hussain, Fazle. s.l. : Cambridge University Press, 1995, Journal of Fluid mechanics, pp. 69-94. ISSN: 1469-7645.
[24] Aspects of Shock Wave-Induced Vortex Breakdown. Kalkhoran, Iraj M. and Smart, Michael K. 2000, Progress in Aerospace Sciences, pp. 63-95. ISSN: 0376-0421.
[25] Amecke, Jochen and Safarik, Pavel. Data Reduction of Wake Flow Measurements with Injection of an Other Gas. Göttingen : DLR, 1995.
[26] Šimurda, David. Transonic and Supersonic Flow in Turbine Profile Cascades (in Czech). Praha : s.n., 2011.
[27] Luxa, Martin and Šimurda, David. Optical Measurements on Transonic Cascade, Research report no. Z 1476/11. Prague : s.n., 2010.
[28] Hofer, Tomáš, et al. Measurement of Selected Flow Field Parameters in Front of TR-L-3 Cascade (in Czech). Prague : s.n., 2011.

14. Appendix 1

14.1. Method of data reduction for measurements with five-hole conical probe

The mass flux equation is then stated as follows.

$$\rho M_x^* = \frac{1}{A r T_0}\left(\frac{2}{\kappa+1}\right)^{\frac{1}{\kappa-1}} \iint_A p_0 \left(\frac{\kappa+1}{2}\right)^{\frac{1}{\kappa-1}} M_x^* \left(1-\frac{\kappa-1}{\kappa+1} M_x^{*2}\right)^{\frac{1}{\kappa-1}} dA \qquad 15.1.1$$

Because the mass flux balance equation is very complicated, substitutions must be made. The highlighted elements of the equation form density ρ. The equation 15.1.1 can then be simplified and marked as K_1.

$$\rho M_x^* = \frac{1}{A} \iint_A \rho \left(\frac{\kappa+1}{2}\right)^{\frac{1}{\kappa-1}} M_x^* \, dA = K_1 \qquad 15.1.2$$

Momentum flux in the direction x is stated as follows.

$$\rho M_X^{*2} + \frac{p}{c_*^2} = \frac{1}{A r T_0}\left(\frac{2}{\kappa+1}\right)^{\frac{1}{\kappa-1}} \iint_A p_0 M_x^* q_x dA + \frac{1}{c_*^2 A} \iint_A p_0 dA \qquad 15.1.3$$

The equation 15.1.3 needs to be separated as well.

$$K_2 = \frac{1}{A r T_0}\left(\frac{2}{\kappa+1}\right)^{\frac{1}{\kappa-1}} \iint_A p_0 M_x^* q_x dA \qquad 15.1.4$$

$$K_5 = \frac{1}{A} \iint_A p dA \qquad 15.1.5$$

With the substitution by the equations 15.1.4 and 15.1.5, the momentum flux equation can be stated as follows.

$$\rho M_X^{*2} = K_2 - \frac{1}{c_*^2}(p - K_5) \qquad 15.1.6$$

Momentum flux in the direction y

$$\rho M_x^* M_y^* = \frac{1}{A r T_0}\left(\frac{2}{\kappa+1}\right)^{\frac{1}{\kappa-1}} \iint_A p_0 M_y^* q_x dA = K_3 \qquad 15.1.7$$

Momentum flux in the direction z

$$\rho M_x^* M_z^* = \frac{1}{ArT_0}\left(\frac{2}{\kappa+1}\right)^{\frac{1}{\kappa-1}} \iint_A p_0 M_z^* q_x dA = K_4 \qquad 15.1.8$$

Energy equation

$$\frac{T}{T_0} = 1 - \frac{\kappa-1}{\kappa+1} M^{*2} \qquad 15.1.9$$

State equation

$$p = \rho r T \qquad 15.1.10$$

For the purposes of solution of above equations, critical speed and critical pressure ratio need to be defined. Critical speed can be stated as follows,

$$c^* = \sqrt{\frac{2\cdot\kappa}{\kappa+1} p_0 \frac{1}{\rho_0}} \qquad 15.1.11$$

and critical pressure ratio as follows.

$$\varepsilon^* = \frac{p_*}{p_0} = \left(\frac{2}{\kappa+1}\right)^{\frac{\kappa}{\kappa-1}} \qquad 15.1.12$$

Also, the equation for changes of the pressure ratio and temperature ratio in isentropic flow [17] needs to be applied.

$$\pi_{(M^*)} = \frac{p}{p_0} = \left(1 - \frac{\kappa-1}{\kappa+1} M^{*2}\right)^{\frac{\kappa}{\kappa-1}} \qquad 15.1.13$$

$$\tau_{(M^*)} = \frac{T}{T_0} = 1 - \frac{\kappa-1}{\kappa+1} M^{*2} \qquad 15.1.14$$

The equation 15.1.13 can be also substituted using the equation 15.1.5.

$$\pi = \frac{1}{c^{*2}}(p - K_5) \qquad 15.1.15$$

Then, individual components of the momentum equations can be stated as follows.

$$M_x^* = \frac{K_1}{\rho} \qquad 15.1.16$$

$$M_y^* = \frac{K_3}{K_1} \tag{15.1.17}$$

$$M_z^* = \frac{K_4}{K_1} \tag{15.1.18}$$

Also, for the purposes of future substitutions, equation 15.1.15 needs to be rewritten as follows.

$$p = \pi c_*^2 + K_5; \rho = \frac{K_1}{K_5 - \pi} \tag{15.1.19}$$

The equation 15.1.11 needs to be rewritten as follows.

$$c^{*2} = \frac{2\kappa}{\kappa + 1} r T_0 \tag{15.1.20}$$

From the equation 15.1.14, the following can be obtained.

$$\frac{T}{T_0} = 1 - \frac{\kappa - 1}{\kappa + 1}\left(M^{*2}_x + M^{*2}_y + M^{*2}_z\right) \tag{15.1.21}$$

The equation 15.1.21 can be substituted with equations 15.1.15 - 15.1.20 and the equation of state obtaining the following equation.

$$\frac{\rho\, p_0}{\rho_0\, p} = 1 - \frac{\kappa - 1}{\kappa + 1}\left[\frac{(K_2 - \pi)^2}{K_1^2} + \frac{K_3^2}{K_1^2} + \frac{K_4^2}{K_1^2}\right] \tag{15.1.22}$$

The left side of the equation 15.1.22 can be adjusted obtaining the following.

$$\frac{(\pi c^{*2} + K_5)(K_2 - \pi)}{r T_0 K_1^2} = 1 - \frac{\kappa - 1}{\kappa + 1}\left[\frac{(K_2 - \pi)^2}{K_1^2} + \frac{K_3^2}{K_1^2} + \frac{K_4^2}{K_1^2}\right] \tag{15.1.23}$$

The equation 15.1.23 can be expanded by K_1^2 obtaining the following.

$$\frac{(\pi c^{*2} + K_5)(K_2 - \pi)}{r T_0} = K_1^2 - \frac{\kappa - 1}{\kappa + 1}\pi^2 + 2\frac{\kappa - 1}{\kappa + 1}K_2\pi - \frac{\kappa - 1}{\kappa + 1}(K_2^2 + K_3^2 + K_4^2) \tag{15.1.24}$$

Left side of the equation 15.1.24 can be adjusted to obtain the following.

$$\frac{(\pi \cdot c^{*2} + K_5)(K_2 - \pi)}{r T_0} = \frac{c^{*2}\pi K_5 + K_2 K_5 - \pi^2 \cdot c^{*2} - \pi K_5}{r T_0} \tag{15.1.25}$$

After separation of all the components belonging to π^2, π the following patrs of the equation 15.1.25 can be obtained.

$$\pi^2\left(\frac{\kappa + 1}{\kappa - 1} - \frac{2\kappa}{\kappa + 1}\right) = -1\pi^2 \tag{15.1.26}$$

$$\pi\left(\frac{2\kappa}{\kappa+1}K_2-\frac{2(\kappa-1)}{\kappa+1}K_2-\frac{K_5}{r\cdot T_0}\right)>\varphi=\left(\frac{2K_2}{\kappa+1}-\frac{K_5}{r\cdot T_0}\right) \quad 15.1.27$$

$$\omega=K_1^2+\frac{\kappa-1}{\kappa+1}(K_2^2+K_3^2+K_4^2)+\frac{K_2\cdot K_5}{r\cdot T_0} \quad 15.1.28$$

Which leads to quadratic equation stated below.

$$-\pi^2+\varphi\pi-\omega=0 \quad 15.1.29$$

Alternatively, the equation 15.1.29 can be solved applying the determinant to the substitutions introduced in 15.1.27 and 15.1.28.

$$\pi_{1,2}=\frac{\varphi}{2}\pm\frac{\sqrt{\varphi^2-4\omega}}{-2} \quad 15.1.30$$

The solution allows directly obtaining static pressure using the equation 15.1.19. The dimensionless speed can be stated using substitution for density $\rho=K_1^2\cdot(K_2-\pi)^{-1}$ as follows.

$$M_{1,2}^*=\sqrt{\frac{(K_2-\pi)^2+K_3^2+K_4^2}{K_1^2}} \quad 15.1.31$$